National Technical University of Athens
School of Applied Mathematical
and Physical Sciences

National Centre
for Scientific Research
Demokritos

Interdepartmental M.Sc. "Physics and Technological Applications"

Master's thesis

A Multi-Wavelength Analysis of the Planetary Nebula NGC 3132 using MUSE, JWST, HST and SST data

Konstantinos Bouvis

Supervisor:
Stavros Akras
Associate researcher

Co-Supervisor:
George Koutsoumbas
Professor

Athens, July 2023

This master's thesis has been carried out in collaboration with the Institute for Astronomy, Astrophysics, Space Applications, and Remote Sensing of the National Observatory of Athens.

https://www.astro.noa.gr
https://www.noa.gr

Abstract

Planetary nebulae (PNe) are the remnants of low to intermediate-mass stars ($1 - 8M_{\odot}$) that have shed their outer layers at the end of their Asymptotic Giant Branch (AGB) phase. In this work, we present a multi-wavelength analysis of the planetary nebula NGC 3132, also known as the Southern Ring Nebula, using data from the MUSE integral field spectrograph, the James Webb Space Telescope (JWST), Hubble Space Telescope (HST) and the Spitzer Space Telescope (SST). Our goals are to examine the physical conditions and chemical composition of the gas and explore their possible variations alongside the nebula. Moreover, we intend to compare our results with an available 3D ionization model of the nebula in order to constrain some of its parameters. Finally, we aim to analyze radially the JWST and Spitzer infrared data to investigate a possible correlation between dust extinction and molecular Hydrogen. For this thesis, we extracted emission line maps from MUSE's datacube and we analyzed those data using SATELLITE python code. For JWST and Spitzer infrared data and HST optical data, we developed our own python code for radial distribution of each available filter, so we can understand the stratification of the nebula. We confirmed that NGC 3132 consists of an ionized central bubble surrounded by a molecular halo with spiral patterns. We created 2D maps for all the physicochemical parameters of the nebula, as well as some line diagnostic diagrams. In addition, we discovered a relation of c(Hβ) with the presence of a substantial amount of dust. This dust component may prevent the H_2 gas from being dissociated. This analysis helped us to provide constrains and lead to a significant improvement of the 3D photoionization model. NGC 3132 is a unique object because of its complex structure and morphology that reveals the history of mass loss and binary interactions of its progenitor star system. Exploring complex systems like this gives us useful information about stellar evolution and especially uncovers details around the formation and evolution of Planetary Nebulae.

Περίληψη

Τα Πλανητικά Νεφελώματα είναι τα υπολείμματα αστέρων χαμηλής και μεσαίας μάζας ($1 - 8M_{\odot}$) που απομακρύνθηκαν στο τέλος της φάσης του Ασυμπτωτικού Κλάδου των Γιγάντων. Σε αυτή την εργασία, παρουσιάζουμε μία ανάλυση του Πλανητικού Νεφελώματος NGC 3132, γνωστό και ως Βόρειο Δακτυλιοειδές Νεφέλωμα, χρησιμοποιώντας δεδομένα από το φασματογράφο του MUSE και από τα διαστημικά τηλεσκόπια James Webb, Hubble και Spitzer. Οι στόχοι μας είναι να εξετάσουμε τις φυσικές και χημικές ιδιότητες του αερίου και να ερευνήσουμε τις πιθανές χωρικές διακυμάνσεις τους. Επιπλέον, σκοπεύουμε να συγκρίνουμε τα αποτελέσματα μας με ένα έτοιμο τρισδιάστατο μοντέλο φωτοιονισμού του νεφελώματος ώστε να περιορίσουμε κάποιες από τις παραμέτρους του. Επίσης, στοχεύουμε να αναλύσουμε ακτινικά τα δεδομένα στο υπέρυθρο μέρος του φάσματος των διαστημικών τηλεσκοπίων James Webb και Spitzer με σκοπό να ερευνήσουμε μία πιθανή συσχέτιση μεταξύ της διαστρικής απορρόφησης και της ύπαρξης μοριακού Υδρογόνου. Για αυτή τη διπλωματική, απομονώσαμε τις γραμμές εκπομπής από τον κύβο δεδομένων του MUSE και αναλύσαμε τα δεδομένα αυτά μέσω του κώδικα SATELLITE στη Python. Για τα δεδομένα του James Webb, του Hubble και του Spitzer αναπτύξαμε τον δικό μας κώδικα στη Python για τη ακτινική κατανομή κάθε διαθέσιμου φίλτρου ώστε να κατανοήσουμε τα διάφορα στρώματα του νεφελώματος. Τελικά, επιβεβαιώσαμε ότι το NGC 3132 αποτελείται από μία κεντρική ιονισμένη φυσαλίδα που περιβάλλεται από μία άλω με υψηλή περιεκτικότητα σε μόρια. Δημιουργήσαμε δισδιάστατες κατανομές για όλες τις φυσικο-χημικές παραμέτρους του νεφελώματος όπως και διάφορα διαγνωστικά διαγράμματα του. Ταυτόχρονα, ανακαλύψαμε μία σύνδεση μεταξύ του c(Hβ) και της ύπαρξης σημαντικού ποσού διαστρικής σκόνης. Αυτή η συνιστώσα της σκόνης μπορεί να εμποδίζει την διάσπαση του H_2 σε άτομα. Η ανάλυση αυτή, μας βοήθησε να θέσουμε περιορισμούς στο τρισδιάστατο μοντέλο και οδήγησε σε σημαντικές βελτιώσεις του. Το NGC 3132 είναι ένα ιδιαίτερα σημαντικό αντικείμενο λόγω της σύνθετης δομής και της μορφολογίας του και αποκαλύπτει την ιστορία της απώλειας μάζας και των αλληλεπιδράσεων ενός διπλού αστρικού συστήματος. Εξερευνώντας σύνθετα συστήματα σαν και αυτό αποκτούμε σημαντικές πληροφορίες σχετικά με την αστρική εξέλιξη και αποκαλύπτονται λεπτομέρειες σχετικά με την σχηματισμό και την εξέλιξη των Πλανητικών Νεφελωμάτων.

To Stavros Akras and George Koutsoumbas for their important help and advises throughout this thesis.

To my friend and colleague Lydia Konstantinou for her cooperation and contribution to this study.

And lastly, to my family and friends for their valuable support.

– Bouvis Konstantinos

Contents

List of figures

Chapter 1

Stellar Evolution

1. Protostar

Stars like our Sun are formed in large interstellar clouds inside the spiral arms of galaxies. These clouds consist of molecular gas (mostly H_2) and dust. They collapse under their own gravity, initially they start to contract and later on they fragment into gravitationally bound cores, which will finally form the **Protostar**. It is known that newly formed stars aren't isolated, instead they are grouped in pretty large groups known as clusters (e.g., a few hundred stars) (Hannu Karttunen, 2017, chapter 16.4).

An interstellar cloud starts contracting only if its mass is large enough, so its gravity can dominate over its pressure. In 1920, James Jean calculated the maximum mass limit for hydrostatic equilibrium. Above this critical mass, the cloud starts to contract.

$$M_J = 3 \times 10^4 \sqrt{\frac{T^3}{n}} \cdot M_\odot \tag{1.1}$$

Where n is the particle density and T refers to absolute temperature.

The contraction of a cloud releases gravitational potential energy. Then, this energy transforms into thermal energy of the gas and into radiation. The contraction takes place in dynamical time scale since the particles of the gas fall freely towards the core.

At first, the radiation is transmitted freely through the gas due to its low density and opacity. In this way, energy escapes through radiation and the temperature of the gas can't increase. Density and temperature are increasing mostly in regions around the center of the gas. As density increases, so does opacity, more and more energy is trapped inside the gas and transformed into thermal energy. So the temperature starts to increase as well as the density, which prevents the gravitational collapse of the system. In this stage, the gas is known as **Protostar** and it consists mostly of molecular Hydrogen (H_2).

When the temperature reaches $1,800\,K$, H_2 starts to dissociate into atoms. This decomposition consumes energy, so the increasing rate of temperature and density is slowing down, while the contraction is accelerating. The same procedure is repeated when H becomes ionised at $10^4\,K$ and later when He becomes ionised. The gas is fully ionised at $10^5\,K$. The contraction of the Protostar stops only when the gas is fully ionised in the form of plasma. Then, the star reaches at hydrodynamic equilibrium state.

The next part of the evolution occurs very slowly on Thermal time scale. At this point, the radius of the Protostar has reduced from $\sim 100\,AU$ to $\sim 0.25\,AU$. The temperature of a star which reaches hydrodynamic equilibrium for the first time is relatively low and the gas has high opacity. At this stage, at the core, energy is transferred through convection. Convection as a procedure is very effective, thus the surface of the Protostar is relatively bright.

1.1. Evolution on the HR diagram

A Protostar (Figure 1.2) is located in the bottom left corner of the Hertzsprung Russell diagram because it's faint and cold. As it is contracting, its surface becomes bright, so it moves up right on the diagram. When the contraction ends, the star is located somewhere on the Hayashi Track; the exact location depends on its mass. Later, the star is moving alongside the Hayashi Track, which corresponds to moving down on the HR diagram (its radius and luminosity decreasing).

As the temperature of the star is increasing, opacity at the center is decreasing and energy is transferred through radiation. The mass of the radiative area is increasing until it covers the whole star. Then,

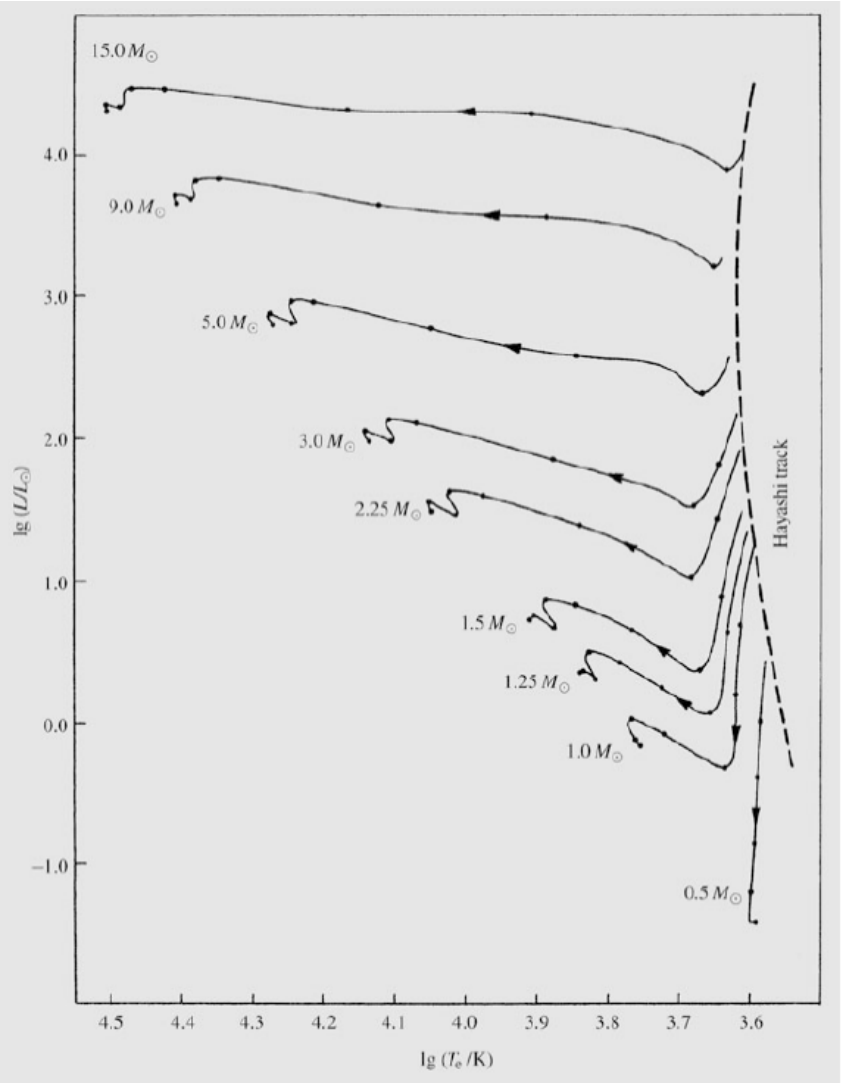

Figure 1.1: After a rapid dynamical collapse, the stars settle on the Hayashi track and evolves towards the Main Sequence on the Thermal time scale.

the temperature at its core is so high that nuclear reactions are possible. Until now, all the available energy was the released gravitational potential energy, while from now on the nuclear energy is the main source. The luminosity and the surface temperature of the star is increasing and the star is moving up left on the HR diagram.

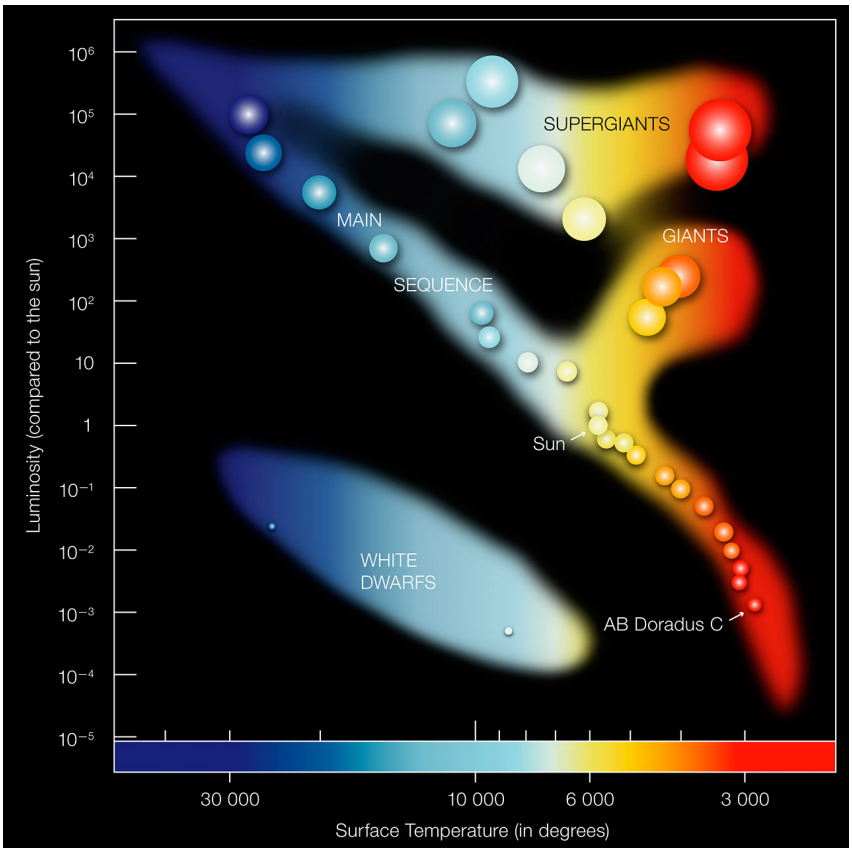

Figure 1.2: Hertzsprung–Russell (HR) diagram.

2. Main Sequence

During the fusion of H to He, the star starts to radiate and it's located at the **Zero Age Main Sequence** (ZAMS) phase. Later, when its mass becomes stable, the star is established on the **Main Sequence** (MS) phase. The MS corresponds to the main diagonal line on the Hertzsprung-Russell diagram (Figure 1.2). The beginning of the Main Sequence is associated with the fusion of H to He through proton-proton chain reaction, at temperatures as high as $4 \cdot 10^6\, K$.

At the Main Sequence phase, the only source of energy is the fusion of H to He, that's the reason why this phase is taking place on Nuclear Timescale, the larger one. In addition, the stars spend almost 90% of their lifetime in the MS phase. As a result, the vast majority of the observed stars are in the MS phase; thus the MS region on the HR diagram is multitudinous, especially at the low mass area. The low mass

stars consume their nuclear fuels slowly, that's why they remain at the MS much longer than the high mass stars. While the star is in the MS phase, it's in hydrodynamic equilibrium; i.e., the thermal pressure (pressure of randomly moving particles) counterbalances the force of gravity. In addition, the star is in thermal equilibrium as well. More extensively, the released energy from the nuclear fusion in the core is transmitted outwards to the surface of the star and emitted away through convection or radiation process.

The Main Sequence stars can't be more massive than $\sim 120\, M_{\odot}$, because then they wouldn't be able to contract through the Protostar phase. Meanwhile, MS stars can't be less massive than $0.08\, M_{\odot}$, because in this way they would never be hot enough for nuclear reactions to start and fuse H. However, this kind of stars, **Brown Dwarfs**, produce a little amount of energy through Deuterium (${}^{2}_{1}\mathrm{H}$) burning. The minimum mass of a Brown Dwarf is $0.015\, M_{\odot}$, stars less massive than this can't even form.

As stated before, low mass stars burn H to He through proton-proton chain reaction. According to this reaction, four H nuclei and four protons in total to form a He nucleus. The released energy from this reaction in proportional to $\propto T^4$.

$$
\begin{aligned}
{}^{1}_{1}\mathrm{H} + {}^{1}_{1}\mathrm{H} &\longrightarrow {}^{2}_{1}\mathrm{He} + e^{+} + \nu \\
{}^{1}_{1}\mathrm{H} + {}^{2}_{1}\mathrm{H} &\longrightarrow {}^{3}_{2}\mathrm{He} + \gamma \\
{}^{3}_{2}\mathrm{He} + {}^{3}_{2}\mathrm{He} &\longrightarrow {}^{4}_{2}\mathrm{He} + {}^{1}_{1}\mathrm{H} + {}^{1}_{1}\mathrm{H}
\end{aligned}
$$

The fusion rate is known as luminosity (i.e., released energy per unit of time) and its relation with the mass of the star is the following:

$$L \propto M^{3.5} \tag{1.2}$$

The time that the star will remain on the Main Sequence (burning H to He in the core) corresponds to:

$$t_{MS} = \frac{M}{L} = t_{\odot} \times \left(\frac{M}{M_{\odot}}\right)^{-2.5} \tag{1.3}$$

Where $t_{\odot} = 1.2 \times 10^{10}\, years$ is the time it takes the Sun to burn all its H fuel and $M_{\odot} = 1.98 \times 10^{30}\, kg$ is the mass of the Sun.

Therefore, through equations (1.2) and (1.3) it is clear that high mass stars are brighter and consume their H fuel more rapidly in their core compared to the low mass counterparts. This occurs due to the different nuclear reactions that take place in the core of the star. Heavy stars consume their fuels through the CNO cycle, while the low mass stars through the p-p chain reaction.

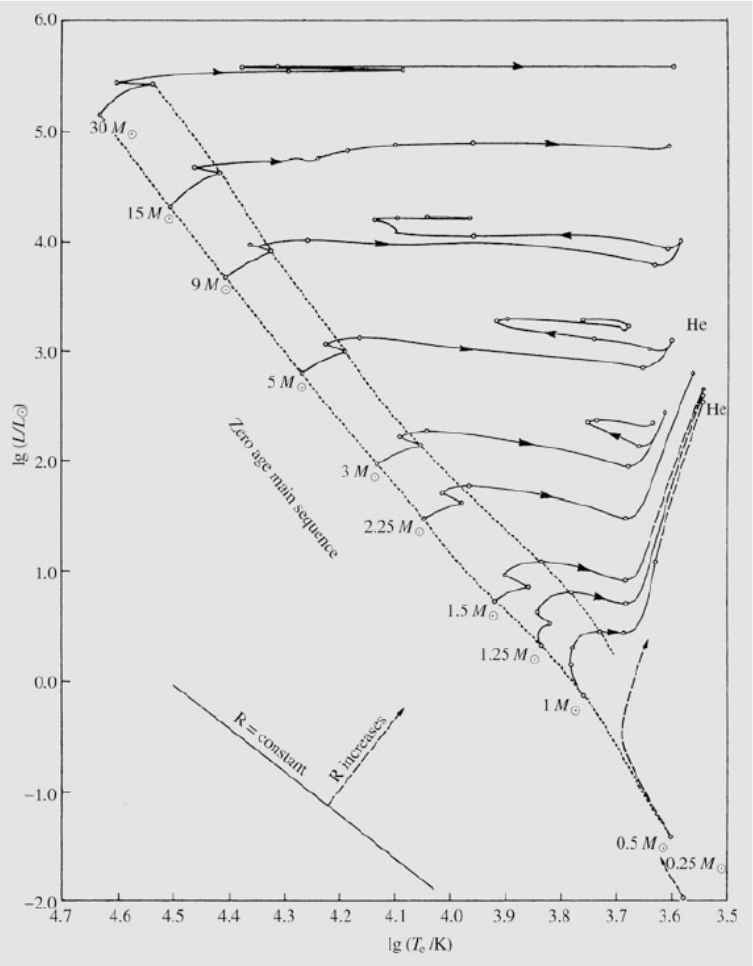

Figure 1.3: Stellar evolution paths in the HR diagram at the Main sequence phase and later. The Main Sequence is bounded by dashed curves. The point marked as He corresponds to Helium ignition and in low mass stars the Helium Flash. The straight line shows the location of stars with the same radius.

2.1. Upper Main Sequence

The stars that are located at the upper part of Main Sequence are so heavy that the temperature in their cores is capable to ignite the CNO

cycle. The produced energy flux from these fusion reactions is transmitted through convection (i.e., material movements). These reactions boost the mixing of material, thus the H abundance is reduced uniformly inside the convection area. Outside the core, energy is transmitted through radiation. The core mass is steadily decreasing while H runs out. In this way, the star is moving up right in the HR diagram while its luminosity increases and its surface temperature decreases. When H runs out, the core shrinks rapidly, the surface temperature increases and the star is moving up left on the HR diagram. Due to contraction of the core, the surrounding H shell temperature increases until it's high enough for H fusion into He to begin.

2.2. Lower Main Sequence

The stars that are located at the lower part of Main Sequence have lower central temperatures compared to heavy stars, and energy is produced through the p-p chain reaction. These reactions aren't as sensitive to temperature as the CNO cycle. Thus, the released energy is spread to a larger area, a convection core isn't created and energy is transmitted only through radiation (Figure 1.4). At the outer shells, opacity is high due to low temperature and energy is transferred through convection. So, the structure of low mass stars is the complete opposite to the one in high mass stars. Since the core material isn't mixed enough, H is consumed quickly at the center and its abundance is increasing radially. While H at the core runs out, the star moves slowly upwards on the HR diagram alongside the Main Sequence as it becomes more bright and hot. Later, the star moves to the right on the HR diagram as H is running out. In the end, the star consists a He core and a thick H-burning shell.

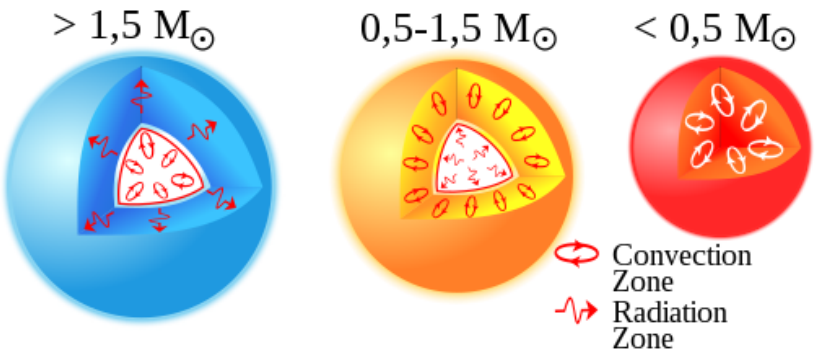

Figure 1.4: Energy transfer of different mass stars.

3. Giant Phase

When all of H turns into He, the Main Sequence phase ends and from now on stellar evolution depends on the initial mass of the progenitor. More specifically, stars more massive than $8\,M_{\odot}$ are called high mass stars, while stars less massive than this limit are called low mass stars.

The star is stable in a state which H is turning into He in a shell surrounding the He core. The transition is happening gradually for low mass stars, creating the **Subgiant Branch** on the HR diagram. On the contrary, high mass stars make a sudden "jump" at this point.

This thesis focuses more on low mass stars, that later in their lives become White Dwarfs and create Planetary Nebulae, which is the main subject.

The **Subgiant** phase starts when the star consists of a He core, which is surrounded by an H shell. The He core's mass is increasing while H is burning at the shell. At this point, energy is transmitted from the core to the surface through radiation (i.e., photons). The difference between the energy produced in the core and the energy that reaches the surface is responsible for heating and the dilation of intermediate layers (i.e., the star's radius increases). This dilation corresponds to a horizontally right movement of the star on the HR diagram. If the star's mass M_* stays unaffected like its luminosity L_*, then according to the formula below (1.4), its effective temperature T_{eff} is decreasing. Finally, the star becomes more red in color and is established in the **Red Subgiant** phase.

$$L = 4\pi R^2 \sigma T_{eff}^4 \quad [\frac{erg}{s}] \tag{1.4}$$

Where $\sigma = 5.67 \times 10^{-8}\ \frac{W}{m^2 K^4}$ is the Stefan-Boltzmann constant and effective temperature is the black body temperature, which emits the same energy flux as the star's surface does.

At the end of the Subgiant phase, the core's temperature isn't high enough in order to fuse He in the core nor to fuse H in the outside shell. Thus, there is no produced energy to counterbalance gravity and finally the core contracts. The temperature rises until the H shell starts burning. The photons which are produced in the shell can't escape, so they push out the outer layers of the star and as a result the star cools down and increases its size. The luminosity increases as well as its radius, even by

a factor of 5,000. The temperature is decreasing, making the star appear even redder. From this moment forward, the star is established in the **Red Giant Branch-RGB** phase and the energy is transmitted through convection and not radiation.

3.1. Helium Flash

While a low mass ($M < 2.3\,M_{\odot}$) (Hannu Karttunen, 2017, chapter 12.4) star is in **Reg Giant** phase, its He core becomes degenerate due to extremely high densities. A degenerate core consists He nucleus and free electrons (fermions), which obey the Pauli exclusion principle. If the star is more massive than $M > 0.26\,M_{\odot}$ (Hannu Karttunen, 2017, chapter 12.4), when its temperature reaches $10^8\,K$ the He fuses to C through triple-alpha process.

$$^4_2\mathrm{He} + {}^4_2\mathrm{He} \rightleftharpoons {}^8_4\mathrm{Be} + \gamma$$
$$^8_4\mathrm{Be} + {}^4_2\mathrm{He} \longrightarrow {}^{12}_6\mathrm{C} + \gamma$$

Oxygen can also be formed through the following reaction:

$$^4_2\mathrm{He} + {}^{12}_6\mathrm{C} \longrightarrow {}^{16}_8\mathrm{O} + \gamma$$

He burning to C occurs simultaneously at all the central region and leads to a rapid increase in the temperature.

At a degenerate gas, electrons have the same position due to extremely high density, so in order to satisfy Pauli's exclusion principle they differ in their momentum. This kinetic energy of the electrons provide the pressure in such a gas, which is known as electron degeneracy pressure. This kind of pressure is capable of counterbalancing gravity.

The degenerate gas doesn't expand when the temperature is increasing, until thermal pressure overcomes the degenerate one, opposite to an ideal gas ($PV = nRT$). In this way, the rise of temperature only accelerates nuclear reactions. So, the degenerate pressure increases with volume's reduction and simultaneously, density also increases, which boosts the electrons to move even faster in order not to be at the same position. So while the temperature at the core is high enough to burn He due to its contraction, the pressure isn't increasing, so the degenerate core doesn't dilate, neither cools down.

When the core's temperature becomes high enough, the core stops being degenerated and dilates violently. Nuclear fusion of He doesn't

have enough space to decompress, so a few seconds after He ignition, there is an explosion known as **Helium Flash**. The released energy from this explosion is absorbed by the outer H layers of the star (that's why it isn't visible) and doesn't provoke a total collapse of the star. This explosion may last for a few seconds, but it emits energy comparable to the whole Galaxy. More specifically, the luminosity of the star is decreasing after the Helium Flash since the core dilates and the shell contracts. Finally, the star ends up in a new state where He is burning to C at the non-degenerate core.

At intermediate mass stars $2.3\,M_\odot < M < 8\,M_\odot$ (Hannu Karttunen, 2017, chapter 12.4), the core's temperature is higher, the central density is lower and the core isn't degenerated. In this way, the ignition of He at the core doesn't have destructive consequences for the central region.

The heavier stars burn He before even they reach the Red Giant Branch. If the star doesn't expel its outer layers due to stellar winds, it will form a **Red Supergiant** or else it will become a Luminous Blue Variable and end up as a Wolf-Rayet star (Hannu Karttunen, 2017, chapter 12.4).

3.2. Horizontal Giant Branch

Right after the Helium Flash, at the end of Red Giant phase, in which He is burning to C and/or O, the star enters the **Horizontal Giant Branch**. Its exact location on the branch depends on the shell's mass. In this phase, the released energy is so powerful that the thermal pressure overcomes the degenerate pressure in the core and the gas becomes ideal once again. The core expands and the H burning in the surrounding shell decreases. At this point, there are two sources of energy, H burning to He at the shell and He burning to C at the core. However, these two sources of energy aren't enough to overcome gravity; thus the star contracts. Its luminosity remains stable and its temperature increases according to equation (1.4). This evolutionary phase is called **Horizontal Branch**.

4. Asymptotic Giant Branch

The evolutionary path of a He core-burning star depends on its mass. Its mass is a decisive factor which determines the maximum core

temperature and the degree of degeneration during the ignition of heavier elements.

When He fuel runs out in the core, He continues to burn in a shell surrounding the core and simultaneously H is burning in an even outer shell (Figure 1.5). The star is moving towards lower temperatures and higher luminosities on the HR diagram. This phase is called **Asymptotic Giant Branch** and it's similar to the previous phase of Red Giant but with slightly higher temperatures.

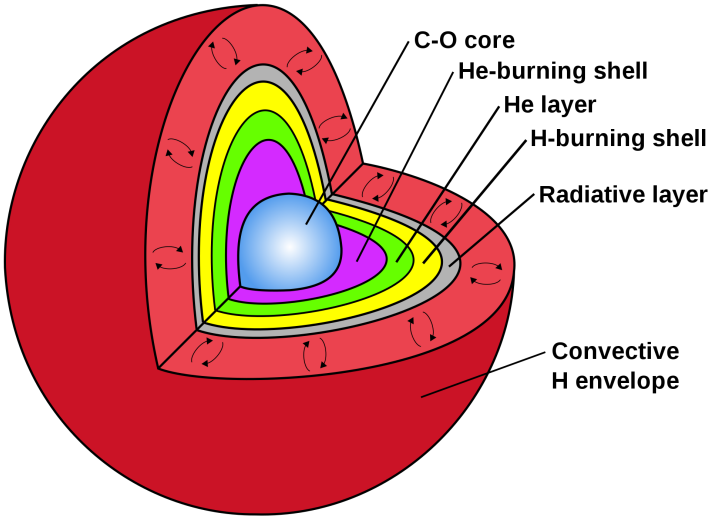

Figure 1.5: Structure of an AGB star.

The star consists of a C core, which is surrounded by an inner He shell and an outer H shell. Nuclear reactions at the core have stopped and they can't resist the force of gravity, so the core shrinks and it's heated once more. The pressure of degenerate electrons prevents the fully gravitational collapse of the star. The temperature's rise isn't enough to ignite C in the core, but it's capable of starting nuclear reactions at the inner He shell and at the outer H one. In this way, the luminosity of the star increases, but once again the produced photons can't escape and are trapped in the H shell, expanding it. The star increases its radius, it cools down and it becomes even redder. This is the beginning of the **Asymptotic Giant Branch** (AGB).

Due to high luminosity and radius, the outer shell of an AGB star is often unstable and it goes through high amplitude pulsating oscillations. In addition, AGB stars have strong stellar winds which remove approximately $\sim 10^{-5} - 10^{-4}\, M_{\odot}/yr$ (Keeton, 2014, chapter 16.3.1)

(Kwok, 2000, chapter 10.4), this means that in $\sim 10^5\, yr$ AGB stars lose a significant amount of their mass. The duration of the AGB phase depends on stellar winds at the surface and not from the nuclear reactions in the core (Kwok, 2000, chapter 10.4).

After the AGB phase, the **post-AGB** phase follows, where the star looses mass due to stellar winds. The star is burning He and H at the inner and outer shell, respectively. This kind of structure is unstable and it leads to matter emission at the ISM. The mechanisms responsible for reducing the star's mass are Helium Shell Flashes and periodical oscillations of the star's outer shell. As a result, the star loses its atmosphere, which consists mostly of He and H, and the remaining C-O core is surrounded by a thin layer of He and H. The exposed core is starting to gradually cool down and the hot, bright material previously ejected from the AGB star forms a Planetary Nebula.

At the next evolutionary phase, the core loses its thin shell of He and H, its luminosity decreases, and it cools downs revealing a White Dwarf.

4.1. Low and intermediate mass stars

Low and intermediate mass stars (Figure 1.6) after He runs out in their core, a C-O core of degenerate electrons is created, this is the beginning of the AGB phase. This phase can be split into two more sub-phases:

1. **Early-AGB** phase, in which the H shell disappears due to the expansion of other shells.
2. **Thermal Burning AGB (TP-AGB)** phase, which starts with the re-ignition of H in a thin shell. The H burning shell is the main source of energy in the most part of this phase. While He mass is increasing at this shell, it leads to higher process rate of triple-alpha reaction and finally to thermonuclear runaway. This is known as **He-shell Flash** or **Thermal Pulse** and lasts until He shell expands and cools down. Then, the star returns to a stable state, where it burns H in the outer shell.

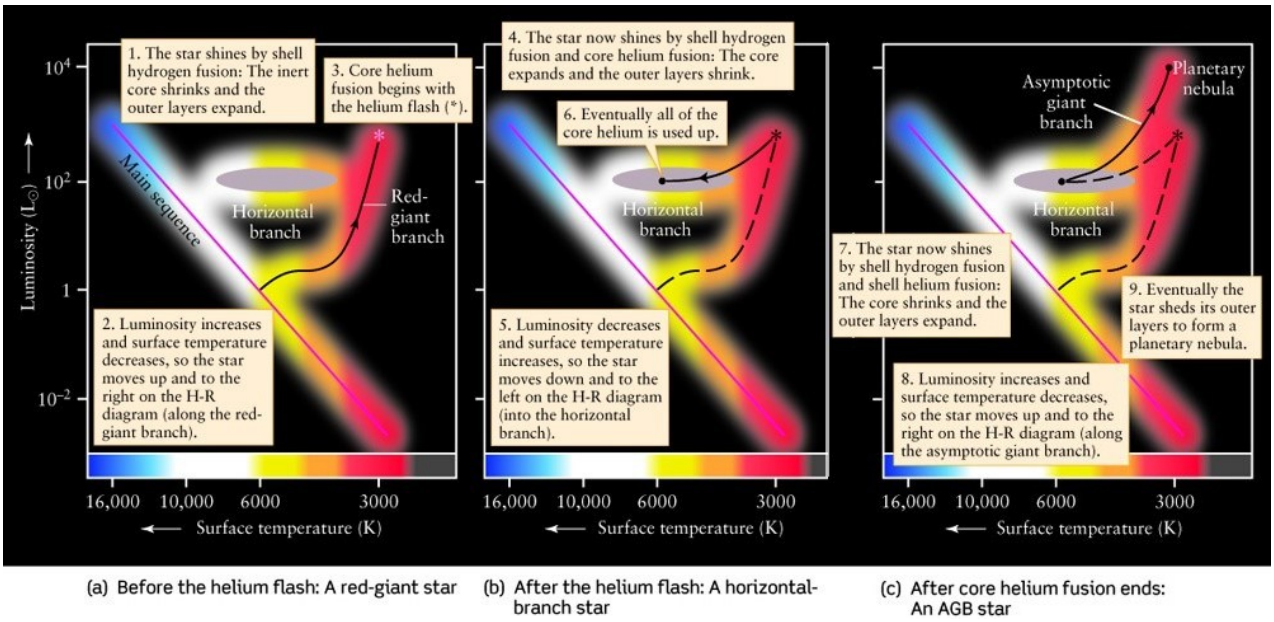

Figure 1.6: Evolution of low-mass stars.

4.2. High mass stars

At the end of He burning the evolutionary path changes because from now on most of the produced energy is escaping the core, in the form of neutrinos. In stars with mass $\sim 10\,M_\odot$ the C or the O ignites with an explosion **Carbon Flash** or **Oxygen Flash** similar to Helium Flash. This explosion is much more powerful and it creates a **Supernova** explosion of the whole star (Hannu Karttunen, 2017, chapter 12.4).

For even higher masses, the core remains not degenerate and the ignition of heavier elements occurs not catastrophically, since the core expands and heats up. Firstly, C is starting to burn, then O and lastly the Si. When each "fuel" runs out at the core, it continues to burn in a shell, thus; the star ends up with many different burning shells (Figure 1.7). In stars with mass $M > 15\,M_\odot$, this process continues until Fe is formed. The structure of these stars, which is a Fe core not producing energy and many shells producing energy, isn't stable and the core collapses.

A small part of the energy released from the collapse, decomposes Fe to He and later on to protons and neutrons. This process accelerates the collapse, like the decomposition of molecules to atoms that accelerated the Protostar collapse. The core collapse lasts only a few seconds, while the outer shells collapse more slowly. The temperature rises at the shells,

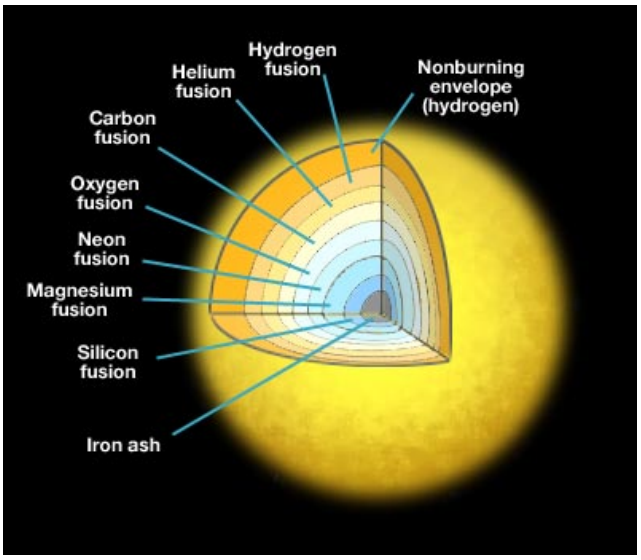

Figure 1.7: Structure of Massive stars after AGB phase.

which still have fuel for nuclear reactions. At these shells, nuclear fusion starts with an explosion, releasing huge amounts of energy through neutrinos. This explosion is known as supernova.

5. Final stages of evolution

For low mass stars, after the Post-AGB phase, the C and O ashes from He burning are deposited at the core, increasing its mass. The increasing force of gravity shrinks the core. In order the core to maintain its equilibrium state, it can't be heavier than $1.4\,M_{\odot}$, which is known as Chandrasekhar limit. Above the limit, the degenerate electron pressure can't counterbalance the inward force of gravity and the star collapses, leaving behind a **Neutron star** or a **Black hole**. In contrary, when the core's mass is lighter from the Chandrasekhar limit, then it will become a small dense object called **White Dwarf (WD)**.

For high mass stars $M > 8\,M_{\odot}$ the final stages of their evolution can be described as a core collapse process which slows down each time a new source of fuel is available. When all the fuels runs out, the outer layers explode with a **Supernova** explosion. At the dense core, protons and electrons merge creating neutrons, which due to huge density create a neutron degenerate core which resists the gravitational collapse creating

a Neutron Star. However, if the core's mass is high enough, there is no known mechanism to prevent the complete gravitational collapse to a Black Hole.

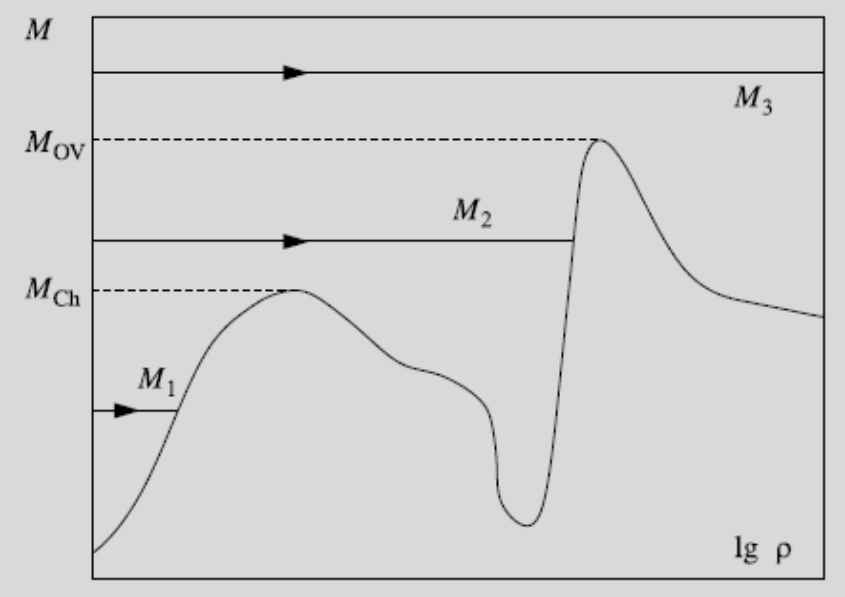

Figure 1.8: The evolutionary end points of stars with different masses, shown as a function of central density. The curve shows the behavior of the central density of completely degenerate ($T = 0\,K$) bodies. Chandrasekhar limit $\sim 1.2\,M_\odot - 1.4\,M_\odot$ and Oppenheimer–Volkoff mass $\sim 1.5\,M_\odot - 2\,M_\odot$ correspond to the maxima on this curve.

In Figure 1.8 it's visible that a star with a mass lower than the Chandrasekhar limit, when it runs out of nuclear fuels, it becomes a WD. It gradually cools down, contracts and finally it reaches $0K$ (Hannu Karttunen, 2017, chapter 12.5), which is the first equilibrium point and the phase of Black Dwarf. A star with mass between Chandrasekhar limit and Oppenheimer-Volkoff limit cools down until it reaches the second equilibrium point and becomes a Neutron Star. Finally, a star with mass higher than Oppenheimer-Volkoff limit it continues to shrink, creating a Black Hole.

5.1. Supernova Remnants

The stage where pressure in the core is high enough to merge protons and electrons to neutrons and neutrinos constitutes the beginning of a **Supernova** explosion. The neutrinos are escaping transferring huge amounts of energy and the electrons that merged were the ones that

helped the core to resist against gravity, through degenerate electron pressure. So, when these electrons are absorbed, the core quickly ($\sim 1.4\,sec$) collapses. When the core shrinks down to $\sim 10\,km$ its density is comparable to the atomic one. Then the gas develops neutron degenerate pressure (relativistic degenerate gas), which prevents the complete gravitational core collapse. Until this point, the collapse releases a huge amount of energy $\sim 10^{46}\,J$. Most of this energy is escaping through neutrinos from the reverse β-reaction and a small portion is transformed to kinetic energy, which is capable of creating shock waves, which disrupts the gas shell of the star. The final result, is a Supernova type II (core collapse). Finally, an even smaller portion of the energy is escaping through photons and as a result a Supernova explosion can produce similar luminosity $10^9\,L_\odot$ of a whole galaxy.

The collapse leads to brutal expansion of the outer layers, which remain as an expanding stellar shell. The continuous emission that is emitted away is created from synchrotron radiation (i.e., relativistic electrons moving in spiral orbits alongside magnetic lines).

Spectroscopically, **Supernova Remnants** (SNRs) are classified to Type I where they don't have any H in their spectra and to Type II where they have H emission lines in their spectra.

Depending on the mechanism that provoked the explosion, they are classified as Type Ia; thermonuclear explosions which originate from small mass progenitors (e.g., a binary system consisting of a WD which earns mass and crosses the Chandrasekhar limit). In addition, they are classified as Type II, Type Ib and Type Ic. These kinds of explosions originate from core collapse of high mass progenitors (e.g., after Fe is produced in a heavy star's core).

5.2. White Dwarfs

The C and O remnants at the core create a hot, dense star known as **White Dwarf** (WD). These stars have a spectral type of O or B and they emit mainly UV radiation, which ionises their surrounding nebula.

The WDs are located in the down left corner of the HR diagram and have a similar radius to Earth's $\sim 6,300\,km$ and mass similar to the Sun's $M_\odot \sim 10^{30}\,kg$.

Below are listed three main mechanisms which create WDs (Hannu Karttunen, 2017, chapter 12.3) (Kwok, 2000, chapter 15.11) :

1. Directly from the Horizontal Branch or from early AGB phase without a producing shell.

   More specifically, very low mass stars $0.08\,M_{\odot} < M < 0.26\,M_{\odot}$ during MS transfer energy only through convection, which means that all the H is available for nuclear fusion. After that, they are evolving slowly and when all of the H have been transformed to He, they shrink down to a WD (Hannu Karttunen, 2017, chapter 12.3) (Kwok, 2000, chapter 15.11).

2. Through TP-AGB phase, while they are evolving slowly and ionising the surrounding nebula.

3. Through TP-AGB and PNe phases.

   In the final stage of a PNe, the shell is expanding and it's merging with the interstellar gas, while the central star becomes a WD.

In an ordinary star, the gas at its center is considered ideal and fully ionised. The partial pressures of the ions, electrons, and the pressure due to radiation counterbalance gravity. When a star runs out of nuclear fuels, its core's density increases while its temperature stays relatively the same. The degenerate electron pressure is the one which counterbalances gravity, since the pressure of ions and radiation is now insignificant. The electron degenerate pressure depends on the density, which increases while the WD shrinks.

In contrary with a typical star, the radius of a WD is decreasing while its mass increases. In this way, when its mass reached $1.4\,M_{\odot}$ the radius of the WD becomes 0, of course, this means that the star collapses and finally it explodes. In this case, the kinetic energy that the electrons should have in order to provide enough pressure to counterbalance gravity corresponds to a velocity higher than the speed of light.

Finally, stars with C-O core and mass higher than $1.4\,M_{\odot}$ have to deposit the bigger part of their mass to the PNe, in order to survive the gravitational collapse.

WDs don't have an internal source of energy, so when they radiate away all of the remaining thermal energy, they change color from white

to red and finally to black. When they reach the background temperature of the Universe, they are known as **Black Dwarfs**. The time they need to cool down is comparable to the age of the Universe and studying the fainter White Dwarfs a lower limit in the age of the Universe can be set.

It's worth noting that because the core is degenerated while it's cooling down, the atoms are lined up to a huge, dense grid (like crystals). It is known that when C is compressed and crystallized in this way, it forms diamonds. So, it could be said that the WDs are "diamond" stars.

5.3. Neutron Stars

If a star's mass is high enough, its density could overcome the one of a WD. The equation of state of a classic degenerate electron gas is replaced by the corresponding relativistic one. Then, the reduction of the radius doesn't help to counterbalance gravity. So, if a star has a mass higher than the Chandrasekhar limit, the gravity overcomes the degenerate electron pressure. The star reaches higher densities, where protons and electrons merge together to form neutrons and the degenerate neutron pressure can resist the force of gravity. The final stable state in known as a **Neutron Star**.

5.4. Black Holes

High mass stars at the end of their life, after the Supernova explosion, create a remnant with mass higher from the Oppenheimer-Volkoff mass $1.5\,M_{\odot} - 2\,M_{\odot}$. In such dense objects, there is no known mechanism to counterbalance gravity and the object collapses to a **Black Hole**.

Due to extremely high concentration of matter in such a microscopic space, the force of gravity is so strong that even the light can't escape, that's why they are called black.

6. Planetary Nebula

The topic of thesis is the study of PN NGC 3132 and in this section we will present the characteristics of these sources.

The AGB phase ends with the elimination of H shell due to stellar winds, before the C ignition. While H shell mass reduces below a specific value, the star starts to heat up. This phase lasts until the central star becomes hot enough to ionise the surrounding nebula. Forbidden lines and recombination lines of metals make the nebula observable in optical wavelengths; and the **Planetary Nebula (PNe)** phase is starting. PNe are high ionisation regions and consist of elements which formed in the progenitor's atmosphere (like H, He, C, N) and heavier elements that were already present in the interstellar medium (like O, Ne, Ar, S).

Proto Planetary Nebula (PPN) can be defined as the evolutionary stage where the central star stopped the huge mass loss at the AGB phase, but it isn't evolved enough to emit the right amount of Ly-α photons to ionise the surrounding remnants of the AGB shell. The mass loss during

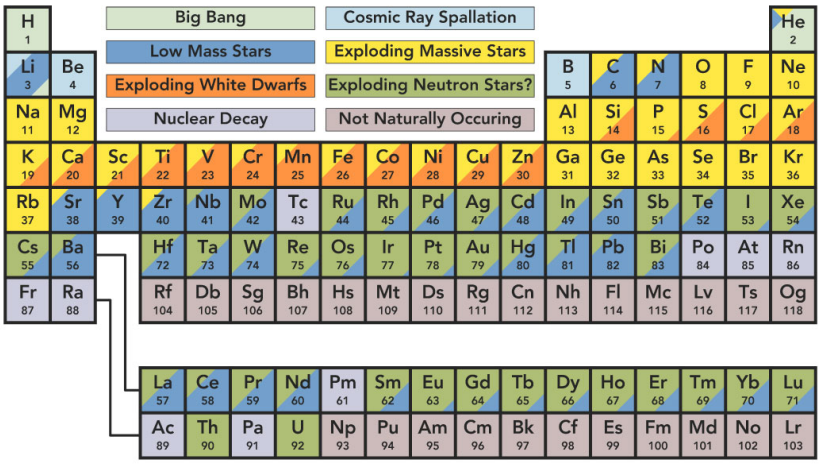

Figure 1.9: Origin of elements.

AGB phase is approximately $\sim 10^{-5}\, M_{\odot}/yr$. For a typical lifetime of a PNe $\sim 10^{4}\, yr$, the star looses around $\sim 0.1\, M_{\odot}$ which is comparable with the predicted PNe mass (Kwok, 2000, chapter 12.1). As a result, the shells of the progenitor AGB stars are related to PNe, but the exact mechanism is quite complicated. Despite the fact that the lifetime of PNe is a really small percentage of the lifetime of low mass stars between Red Giant phase and

White Dwarf phase, PNe play a significant role in the enrichment of the interstellar medium with necessary elements for the formation of new stars (Figure 1.9).

Table 1.1 gives the typical values for some physical parameters of a PN (Kwok, 2000, chapter 2 and 11.3) (Donald E. Osterbrock, 2006, chapter 1.6). Due to the expansion velocity of the nebula, after its lifetime the nebula becomes so big and sparse that it doesn't distinguish itself from the interstellar medium (ISM).

n_e	T_e	Lifetime	Size	Mass	Expansion Velocity
$100 - 10^4 cm^{-3}$	10,000 K	10^4 yrs	0.2 pc	0.1-1 $M_\odot$	25 km/s

Table 1.1: Typical values of some physical parameters for a Planetary Nebula.

Due to the mass loss in AGB phase, 95% of all the stars in the Galaxy will end up to White Dwarfs and 60% (Kwok, 2000, chapter 2 and 18.10) of them will go through the PNe phase. It is estimated that one PNe is created each year in our Galaxy and there are total of $\sim 14,000$ (Kwok, 2000, chapter 2 and 18.10). Figure 1.10 display a few of the most well studied and known PNe.

The term "Planetary Nebula" is misleading and it comes from the fact that when they were first observed, in the 19^{th} century, the astronomers at the time believed they were planets due to their small spherical size.

6.1. Formation of a Planetary Nebula: Interacting Stellar Winds Model

The Interacting Stellar Wind model proposed by Kwok (2000, chapter 12.2) (Kwok, 1978) is the most widely accepted scenario for the formation of PNe. Their formation begins by the mass loss of AGB stars, due to a slow stellar wind. The AGB core, which lost its outer parts, increases its temperature while the thin H layer is burning by nuclear reactions. When the central star is hot enough, a new mass loss occurs from radiation pressure. Given the fact that the radius of the star is much smaller than the AGB stage, the speed of the new stellar wind is much higher, since it's related to the escape velocity. The shells that were created by the slow stellar wind in a time period of $10^6\, yr$, change shape from the new fast stellar wind, which gives them the final shape that we observe today

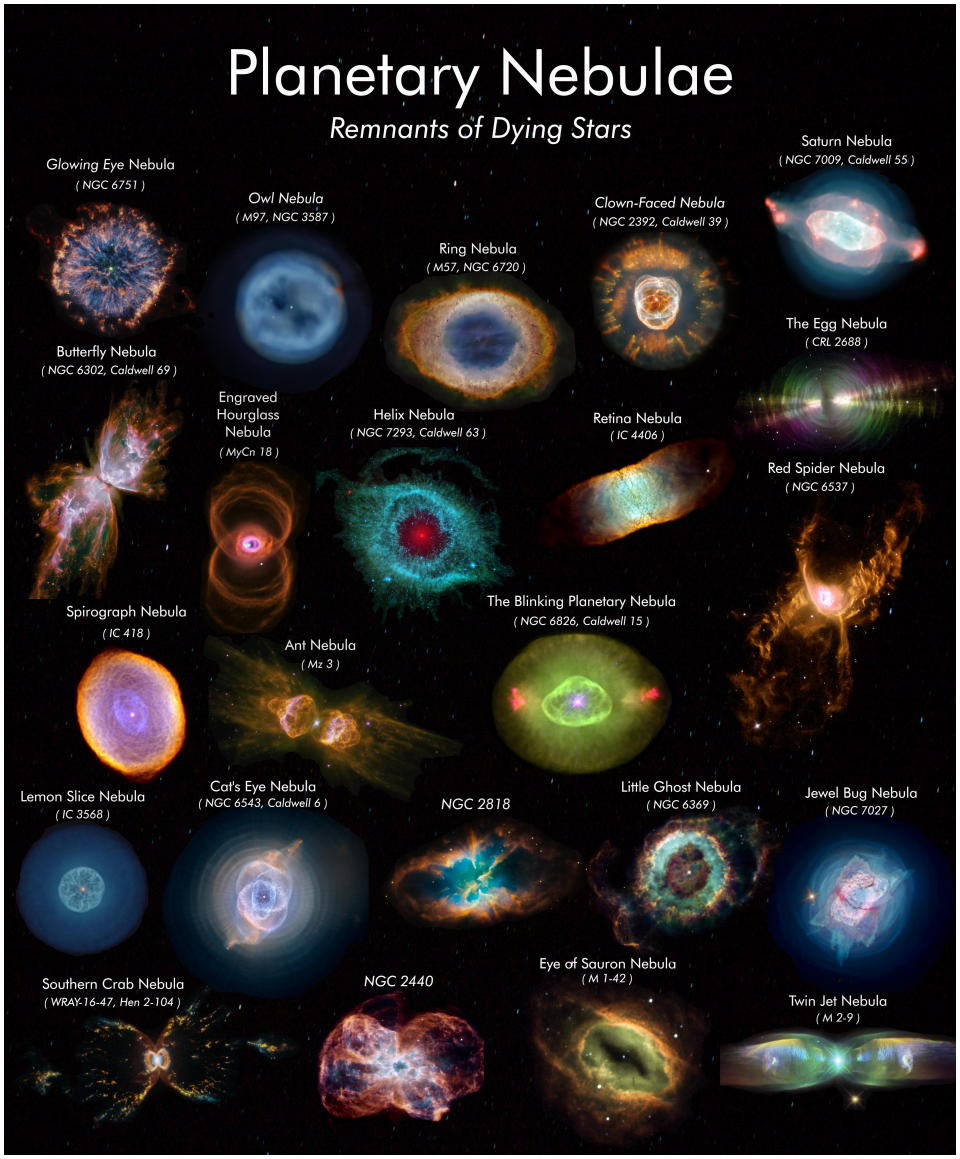

Figure 1.10: Typical Planetary Nebulae.

as a Planetary Nebula. The interaction of the two stellar winds creates high temperature bubbles, which create pressure at the shell, forcing it to expand (Figure 1.11).

The increasing UV radiation flux from the star gradually ionises the shell, which increases its mass due to stellar winds. When the H layer is exhausted due to the nuclear fusion reactions, the core of the star cools down, decreases its luminosity and finally becomes a White Dwarf.

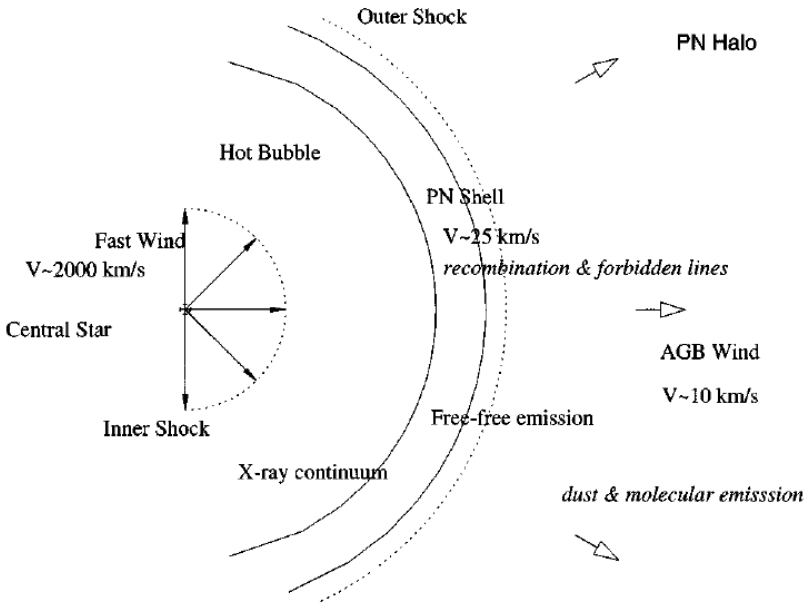

Figure 1.11: Schematic diagram of the ISW model.

Despite the fact that the ISW model explains density, velocity and the structure of a PN shell, simultaneously, it makes some predictions, which have been successfully verified through observations. More specifically, the model predicts the presence of an outer faint halo as a remnant of the AGB shell and an X-ray emission from the hot bubble.

The **ISW** model suggests that both slow and fast stellar winds are isotropic and that the PN has spherical symmetry. In reality, the density of the slow AGB wind differs at the poles in comparison with the equator and when it interacts with the fast spherically symmetrical stellar wind it can create a not spherical PNe (Balick, 1987; Icke, 1988). Possible mechanisms that explain slow wind anisotropy are listed below.

1. The remaining Protostellar disk from the star's creation.
2. Compressed flux at the equator.
3. Stellar rotation.
4. Presence of magnetic fields.
5. Interaction with a companion star (Livio and Soker, 1988).

In the case of a binary system, the morphology of the PNe will probably be bipolar (Frank et al., 2018; García-Segura et al., 2018). Due to mass transfer, binary systems could have a much more complex evolutionary path prior to and after the Planetary Nebula phase.

6.2. 3D morphokinematic studies on PNe with Shape code

SHAPE is a program used to examine the primary morphokinematic characteristics and recreate the three-dimensional shape of astrophysical objects (Steffen et al., 2011). When using only imaging to describe the shape of a PN, it can be misleading due to the uncertainty introduced by the projection effects on the plane of the sky. For example, an axisymmetric nebula like a bipolar one, with a thick waist observed pole-on, would appear as a circular doughnut when projected onto the sky. In such cases, high spectral resolution spectroscopy is an ideal tool for exploring the nebula's three-dimensional structure by examining Doppler shifts in the emission-line profiles (Akras and López, 2012; Akras et al., 2012).

SHAPE modeling involves three main steps. Firstly, the user defines the geometrical forms to use, such as a sphere, torus, or cube, which can be modified further by the user's needs. Secondly, an emissivity distribution is assigned to each object individually. Thirdly, a velocity law is selected based on position from the geometrical center. SHAPE produces a two-dimensional image and synthetic position-velocity (PV) diagrams, which are rendered from the 3D model and compared visually with the observed data. The model's parameters are then iteratively adjusted until a satisfactory solution is obtained (Akras and López, 2012).

Studying PNe with high spatial resolution imagery and high-dispersion spectroscopic data helps us better understand and gain insights into the formation, interaction, and evolution of various nebular components (e.g., shell, rim, bipolar outflows, knots, torus, etc.) (Gómez-Gordillo et al., 2020). The findings of studies like these strongly suggest the significance of evaluating the true structure of PNe for statistical studies that consider the different morphological classes for evolution and population synthesis studies (Akras and López, 2012; Akras et al., 2012, 2015).

6.2.1. The case of PN Abell 14

A 3D morpho-kinematical study of Abell 14 performed by Akras et al. (2016) using the astronomical code SHAPE. The central ring-like structure observed in Hα and [N II] lines appears faint due to the projection effect. Additionally, the eastern and western regions of the nebula exhibit blue and redshifts, respectively.

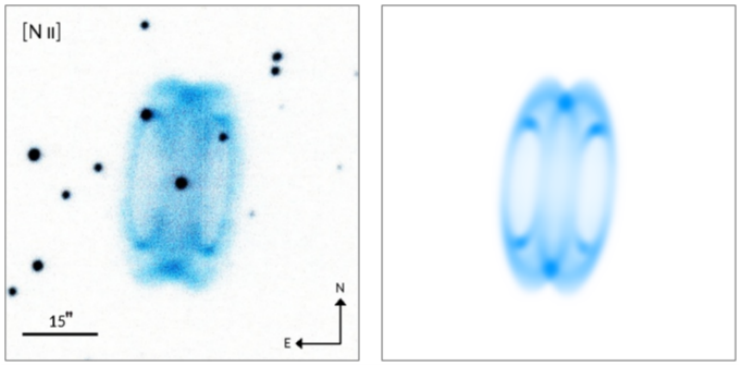

Figure 1.12: [N II] 6584 Å image (left-panel) as observed and the 2D rendered SHAPE image (right-panel).

Akras used an ellipsoidal shell to model the main body of the nebula, which was modified to match the observed image and PV diagrams. The model also includes two symmetrical rings positioned on either side of the nebula's center (Figure 1.12).

Abell 14 has a hollow bipolar shape, with its lobes extending in the east-west directions. The [N II] emission mainly originates from the bipolar lobes' walls, while the [O III] emission originates from the central region. The Hα and [N II] lines reveal two ring-like structures in the eastern and western parts of the nebula, but they are not present in the [O III] line.

6.3. Planetary Nebulae spectrum

The source of energy that makes the nebula radiate is the ultraviolet radiation from the central star of the PN. The spectrum of PNe consists of many emission lines and a weak component of continuum radiation.

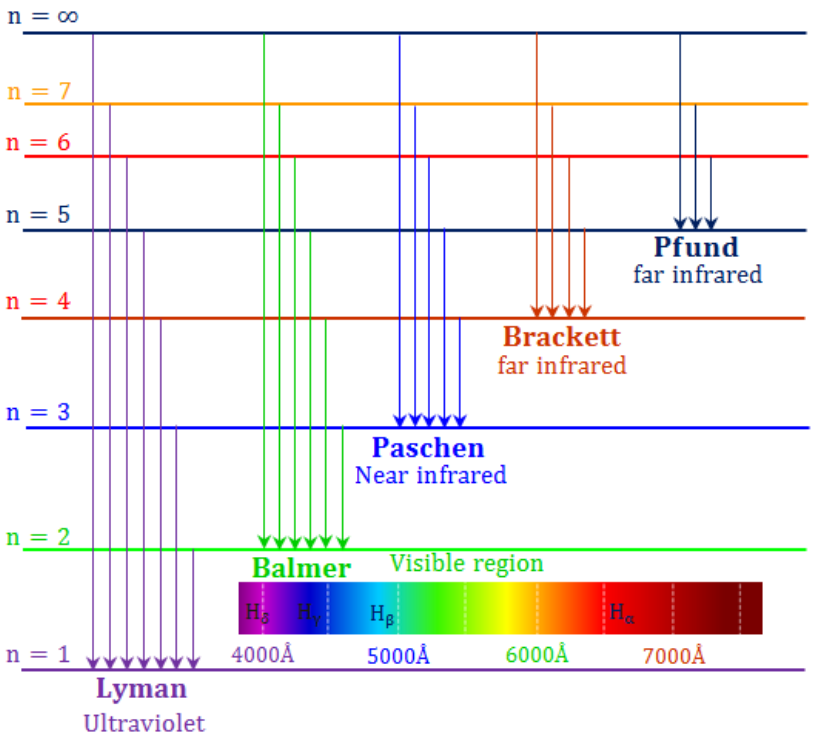

Figure 1.13: Hydrogen line series.

Recombination Lines

These lines (e.g. Hα, Hβ, Hγ etc.) are quite strong and are detected in PNe spectra (Figure 1.13). The central star emits many photons of continuum radiation with energies higher than 13.6 eV and as a result H atoms are ionised, creating a plasma of ions and free electrons. In general, the phenomenon where an atom absorbs a photon and its electron gets excited to a different bound energy state (bound-bound transition) or it becomes free (bound-free transition) is called photoionisation. If the photon has a higher energy from the ionisation energy of an atom, the extra energy is transformed into kinetic energy of the free electron.

The electrons that become free, distribute their energy through collisions with other electrons and ions. The thermal electrons recombine with ions creating excited atoms which later get de-excited to lower energy states, emitting photons until they reach the ground energy state. So, every continuum radiation photon from the central star is transformed to a Lyman-α photon and a line photon (e.g. Balmer).

Forbidden emission lines

Some atoms have metastable states which differ a few eV from the ground energy level. The free electrons from photoionisation are able to excite, through collisions, atoms to these particular states. Metastable states under normal density conditions don't have enough time to de-excite spontaneously, due to collisions. In Earth-like conditions, these transitions don't occur, so they were named forbidden. However, in the environment of a nebula which typically has really low density, these transitions are observed. The forbidden energy transitions are symbolized by two brackets (e.g. [N II]).

Continuum radiation

There is a weak component of continuum radiation in the whole range of electromagnetic spectrum of a PN. Free-bound transitions contribute to the continuum mainly at optical wavelengths and less at infrared (e.g. Balmer continuum, Paschen continuum). These transitions describe the recombination of a free electron with an ion at an excited state.

Free-free emission or Bremsstrahlung contributes to the continuum emission at infrared, radio, and X-rays. More specifically, when an electron passes by an ion, it accelerates and emits radiation. Since each free electron has a different energy and passes by at different distances from the ion, the resulting emission is continuous.

The two photons emission during the de-excitation of the 2^2S H state is another mechanism of emitting continuous radiation.

Last, interstellar dust scatters and absorbs radiation from the central star; it gets heated and re-emits continuous radiation at infrared wavelengths.

Thermal Equilibrium

The recombination process and collisionally excited atoms from free electrons are the cooling mechanism of the nebula, since they absorb energy from it. In contrary, photoionisation is the heating mechanism of the nebula, since it provides energy to the system. Thermodynamic equilibrium is achieved at every point in the nebula, where the heating mechanism is balanced by the cooling one.

6.4. Physical characteristics of the PNe

The extinction coefficient of a nebula c describes the amount of absorption and scattering of the emitted radiation. In particular, dust and gas (e.g. Earth's atmosphere and ISM) between the object and the observer interact with the emitted radiation, turning it redder. In order to correct the emission lines from interstellar extinction, the ratio of specific emission lines is measured and compared with the predicted value from quantum mechanics. In this way, the variation is quantified in the extinction coefficient. The most common lines that are used for this correction are the H Balmer lines Hα and Hβ, that's why the parameter is often known as $c(H\beta)$. Hγ and Hδ lines can also be used to determine the extinction coefficient ($c(H\gamma)$, $c(H\delta)$) but their lower intensities make these estimates less accurate than $c(H\beta)$.
Galactic reddening law of Howarth (1983) :

$$R_V = \frac{A_V}{E(B-V)} = 3.1 \tag{1.5}$$

$$E(B-V) = A_B - A_V = (B-V) - (B-V)_0 \tag{1.6}$$

$$c(H\beta) = \frac{1}{0.348} \log\left(\frac{\frac{F(H\alpha)}{F(H\beta)}}{2.85}\right) \tag{1.7}$$

Where $F(H\alpha)$ and $F(H\beta)$ are normalized fluxes according to $F(H\beta) = 100$ and 2.85 is the theoretical $H\alpha/H\beta$ value for $T_e = 10,000\,K$ and $N_e = 1,000\ cm^{-3}$.

$$E(B-V) = 0.61 \cdot c(H\beta) + 0.024 \cdot c(H\beta)^2 \tag{1.8}$$

$$c(H\beta) = 1.451 \cdot E(B-V) \tag{1.9}$$

The electron temperature of the nebula (T_e) is estimated from specific emission line ratios. More specifically, lines that are emitted from two energy states with different excitation energy and similar de-excitation probabilities of the same ion (Figure 1.14).

$$\frac{[O\ III]j(4959\lambda + 5007\lambda)}{j(4363\lambda)} = \frac{7.90 \cdot e^{\frac{3.29 \cdot 10^4}{T_e}}}{1 + 4.5 \cdot 10^{-4} \frac{N_e}{\sqrt{T_e}}} \tag{1.10}$$

The electron density of the nebula (N_e) is estimated again by specific emission line ratios. This time, lines that emitted from two similar energy

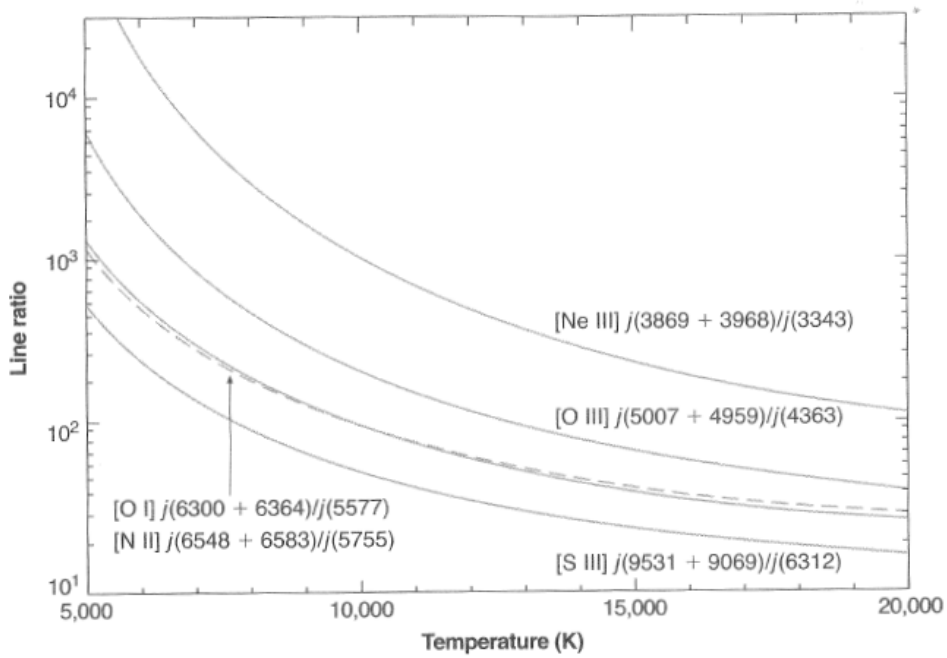

Figure 1.14: Four temperature sensitive forbidden line ratios are shown as a function of the electron temperature. The ratios are shown in the low density limit ($n_e = 1\,cm^{-3}$).

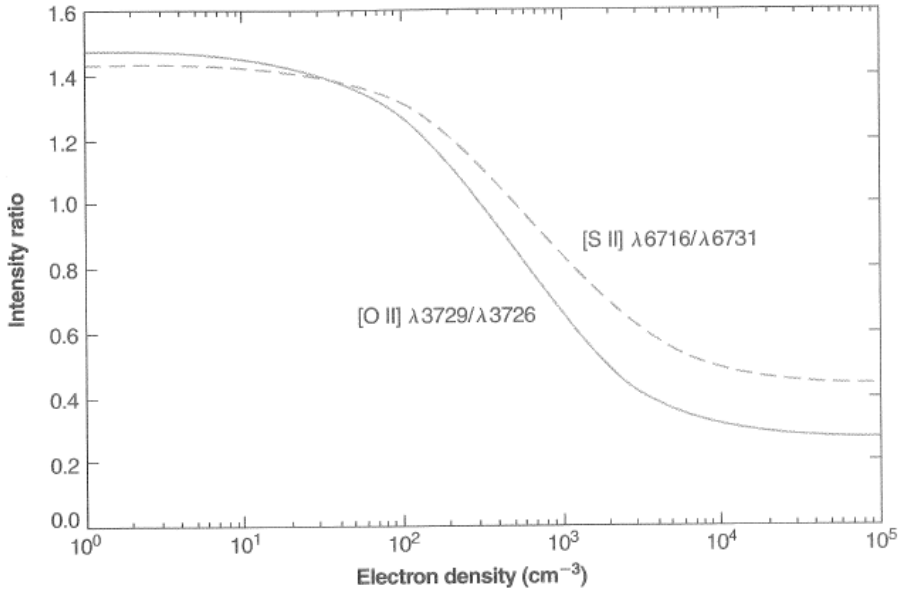

Figure 1.15: Calculated variation [O II] (solid line) and [S II] (dashed line) intensity ratios as functions of n_e at $T = 10,000\,K$.

states and different de-excitation probabilities of the same ion (Figure 1.15).

$$\frac{[S\ II]j(6548\lambda + 6583\lambda)}{j(5755\lambda)} = \frac{8.23 \cdot e^{\frac{2.5 \cdot 10^4}{T_e}}}{1 + 4.4 \cdot 10^{-3} \frac{N_e}{\sqrt{T_e}}} \tag{1.11}$$

Since electron temperature and density are estimated, the abundance of different ions can be computed, as well as the total elemental abundances. The ionic abundances are computed relative to H^+ abundance and the total abundances relative to H abundance. For the estimation of the total abundances, Ionisation Correction Factors are necessary (Kingsburgh and Barlow, 1994; Delgado-Inglada et al., 2014). These factors consist of the contribution of ions that are not detected or not covered by the observations. Finally, it is worth noting that in the above calculations the distance of the nebula isn't needed.

Through extended study of specific abundances (He, C, N) in PNe we are able to check the reliability of stellar evolution models. Furthermore, using the abundance ratios $\frac{He}{H}$ and $\frac{N}{O}$ the estimation of the progenitor star's mass is possible. Finally, through the abundances of O, Ne, Ar and S we can detect the metallicity of the region where the star formed.

Through observations, it is known that the abundances that have been calculated through collisionally excited lines and the ones that were estimated by recombination lines aren't the same. The ones from the recombination lines have systematically higher values, usually by a factor of 10. The exact mechanism behind this difference is an open research subject, but recent studies have pointed out a possible link with binary central systems (García-Rojas et al., 2022a).

6.5. Molecular gas in Planetary Nebula

The presence of molecular gas in PNe is explained by the existence of remnant shells from the progenitor AGB stars. The molecular gas suggests the presence of extra material in PNe than the one provided from the optical observations. Vibrational and rotational energy states of molecules differ only a little from electronic energy states, so when electrons de-excite from these states they emit infrared or millimeter-wave photons. Some examples of the vibrational-rotational transitions of

H_2 are shown in Figure 1.16 (Kwok, 2000, chapter 5).

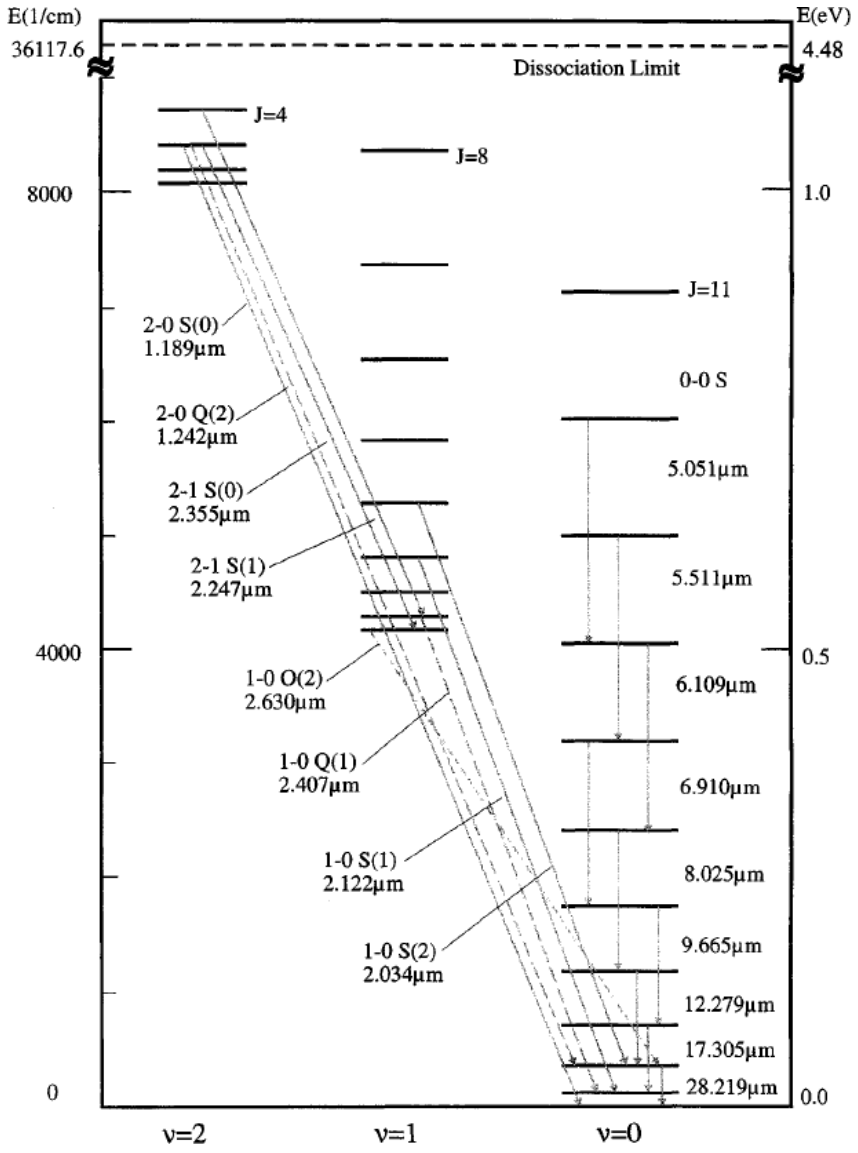

Figure 1.16: The energy diagram of molecular Hydrogen and the observed energy transitions.

6.6. Central Stars of Planetary Nebula - CSPN

Central stars are mainly spectral type O or B or in rarer cases Wolf-Rayet stars which emit most of their radiation at UV wavelengths. They have an effective temperature around $25,000\,K - 300,000\,K$ and on HR

diagram they are located between Red Giants and White Dwarfs (Figure 1.2). Furthermore, their cores have typical masses of $0.55\,M_{\odot} - 0.64\,M_{\odot}$.

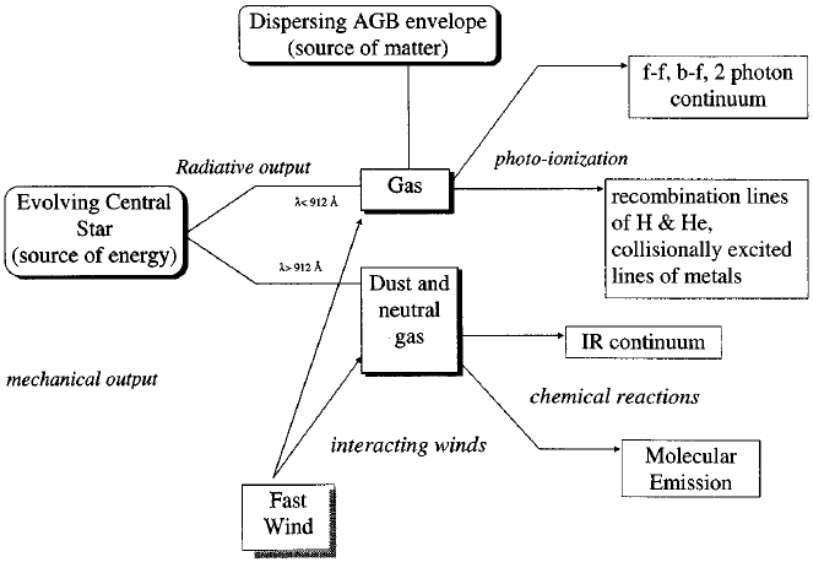

Figure 1.17: Schematic showing the interactions between the central star and the nebula.

CSPN are difficult to be observed because they are faint at optical wavelengths due to their high temperatures. The central stars of Planetary Nebula were created from the degenerate C-O cores of the AGB stars. After the removal of the thin H shell from the nuclear reactions and stellar winds, the star gains energy from gravitational contraction. From now on, the star cools down with a gradual reduction in its luminosity and temperature. The resulting blue, faint stars are known as White Dwarfs.

Despite the fact that all the CSPN will become White Dwarfs, not all the WDs have necessary went (gone)through the PNe phase.

6.7. Classification of PNe and their morphology

It is commonly said that the chemical abundances of a PNe depend on the mass of the central star. The **PNe Type I** have high He, N abundances, they are usually bipolar and originate from high mass stars. **PNe Type II** and **PNe Type III** are nebulae of the Galactic disk with low and high dispersion velocities, respectively. Finally, **PNe Type IV** are halo objects.

This classification is a decreasing sequence of initial mass and increasing age (Kwok, 2000, chapter 19.4).

PNe have been observed in a wide variety of shapes and morphologies. The main reason behind these various shapes haven't been fully understood yet. PNe are morphologically usually classified as elliptical, spherical or bipolar. PNe display large scale components like rims, shells, and halo as some small structures like low ionisation structures (LIS) and jets, knots, filaments. The different morphologies are created from all the different ways in which the gas that initially ejected from the star to interstellar space diffused and interacted with the ISM. There are other factors which affect the final morphology, like the magnetic field, the rotational velocity and the radiation pressure from the star.

Possible theories explaining the different morphologies are:

1. They refer to a different perspective of the shame 3D structure.
2. Each morphology corresponds to a different evolutionary stage of a common evolutionary path that all PNe follow.

Chapter 2

The Planetary Nebula NGC 3132

1. Planetary Nebula NGC 3132

The young planetary nebula NGC 3132 or Southern Ring Nebula is located in the constellation Vela and it consists of a multiple stellar system. The distance of the brighter A-type star has been computed $d = 754^{+15}_{-18}$ parsec (lower and upper 1σ-like confidence intervals) by inverting its parallax (1.3198 ± 0.0344 mas) as it is listed in the GAIA DR3 database (Gaia Collaboration, 2020; Chornay and Walton, 2021; Bailer-Jones et al., 2021). Due to the fact that the distance from the central star have pretty high uncertainties, the distance to the central star's visual companion is adopted as the distance to the PN. The angular dimensions are approximately $58" \times 85"$.

The initials NGC are an abbreviation for New General Catalogue that was completed in 1888 by John Louis Emil Dreyer. NGC is the most famous astronomical deep sky object catalogue in Astronomy.

Observations of NGC 3132 revealed the existence of a binary system at its center (Ciardullo et al., 1999) with rotational period $25,500$ years and 45^o angle between orbital and sky planes (Sahai et al., 2023). The binary system was first observed by Kohoutek and Laustsen (1977). The fainter of the two stars is the young White Dwarf, which ionises the surrounding nebula, while the companion star is a hot Subgiant (Mendez

et al., 1978; Méndez, 1978).

Due to the interaction between the pre-white dwarf and the companion star, the morphology of the Planetary Nebula deviates from the spherical shape and looks more like an elliptical-bipolar one.

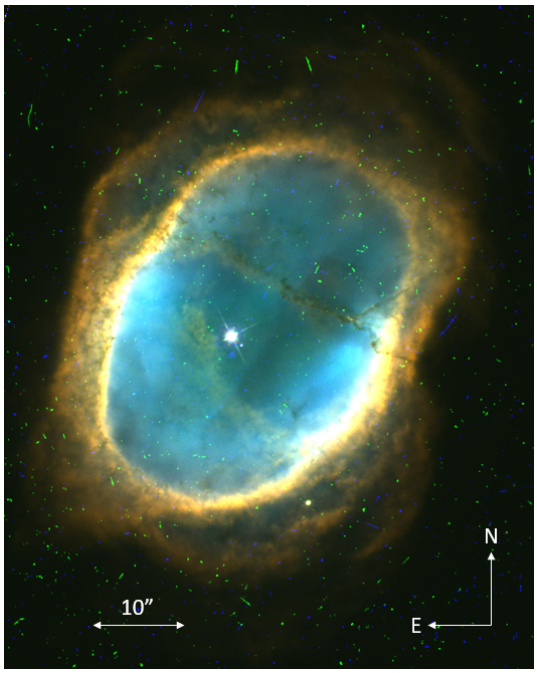

Figure 2.1: Hubble Space Telescope (HST) RGB image of the Planetary Nebula NGC 3132.

Through a python script we created an RGB image of NGC 3132 from HST (2.1), the colors reflect the temperature of the gas. The blue color represents the hot gas, which is constrained at the inner region of the nebula. On contrary, the red color represents the cold gas, which is located at the outer region. The filters that were used for this image are the following: Blue: F502N ([O III]) Green: F656N (Hα) Red: F658N ([N II])

1.1. The companion star

The central bright star, or as it is known HD 87892 was the first one observed in the Planetary Nebula NGC 3132 in 1918 (Henry Draper Catalog). HD 87892 has a mass of $M \sim 2.4\, M_{\odot}$, temperature $T_{eff} \sim 9200\, K$ and luminosity $L \sim 57\, L_{\odot}$ (De Marco et al., 2022). It is an evolved Main

Sequence star with spectral type A2V. It was known for years that this star is not hot and luminous enough to ionize the nebular gas.

1.2. The young White Dwarf

The young White Dwarf, which ionises the surrounding nebula, wasn't observable due to the low resolution of the telescopes at that time. It was first observed in 1977 by Kohoutek and Laustsen (1977). The White Dwarf is located at a distance of ~ 1.7 arcsec South-West from the companion star, it has mass $M \sim 0.7\, M_{\odot}$ (Sahai et al., 2023) and has A0 spectral type. In addition, the CSPN has luminosity $\log(\frac{L}{L_{\odot}}) = 2.19$ and effective temperature around $T_{eff} = 10^5\, K$ (Monreal-Ibero and Walsh, 2020).

1.3. Characteristics of the Southern Ring Nebula

The most accepted morphology of NGC 3132 was the one proposed by Monteiro et al. (2000). More specifically, NGC 3132 has a diabolo-like shape with 40^o inclination with the line of sight while its major axis is rotated by 22^o. The inner ionised cavity has an elliptical shape with major axis ~ 40 arcsec (Figure 2.2).

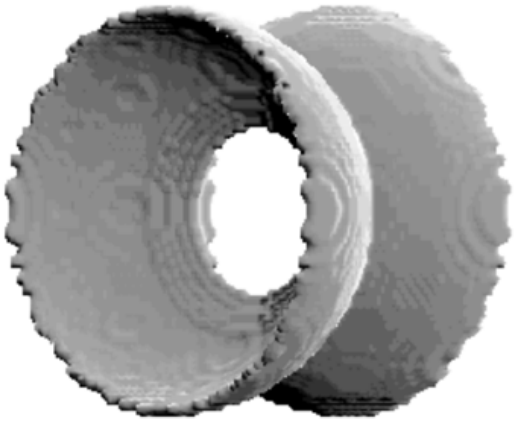

Figure 2.2: Gas distribution of the diabolo model. Only the denser zone is shown. There is a less dense zone which fills the rest of the nebula.

Furthermore, the nebula is classified as spectral type II based on the observed abundances ratios $N/O \sim 0.42$, $He/H \sim 0.124$ (Monreal-Ibero

and Walsh, 2020).

In one of the most recent studies of the Southern Ring nebula by Monreal-Ibero and Walsh (2020), the nebula was observed with MUSE (Multi Unit Spectroscopic Explorer) instrument mounted on VLT (Very Large Telescope), in Chile. Electron density (N_e) was measured $\sim 1,100\ cm^{-3}$ in the inner high ionisation region and $\sim\ 400\ cm^{-3}$ in the outer low ionisation region. Meanwhile, electron temperature only slightly ranges from $9,500\,K$ in high ionisation regions to $9,800\,K$ in low ionisation ones.

It is worth noting that according to a previous study by Sahai et al. (1990), the mass of the neutral matter is $\sim 0.02\,M_{\odot}$, which is comparable if not larger than the ionised mass. In addition, the maximum H_2 emission was detected at the end of the minor axis and not at the poles. In contrary, the maximum outflow occurs at higher speeds at the poles than at the equator. Moreover, additional studies from Zuckerman and Gatley (1988) and Mata et al. (2016) have also found molecular hydrogen in the nebula.

It is known that abundances from recombination lines are higher than the ones from collisionally excited lines. The ratio of these two abundances is called ADF (Abundance Discrepancy Factor) (García-Rojas et al., 2022b). According to Tsamis et al. (2004) NGC 3132 has $ADF(O^{+2}) = 2.4$ and $ADF(N^{+2}) = 3.9$, which is considered relative low compared to other PNe.

1.4. Observations by the James Webb Space Telescope

Among the first images obtained with JWST were those of the Southern Ring Nebula. They were part of Early-Release-Observations (EROs) of the James Webb Space Telescope (De Marco et al., 2022). These observations covered near and mid infrared wavelengths, and more specifically the wavelength ranges from $0.9\,\mu m$ to $18\,\mu m$.

Figure 2.3 (right panel) illustrates the mid-infrared images of NGC 3132 from MIRI on JWST. The hot central star of the nebula is easily observed, given the fact that the mid infrared emission is optically thin. On the other hand, the hot CS can not be seen in the near infrared image from NIRCam. In addition, the hot gas surrounding the central stars and the cold gas ring are visible in both images. In the image captured from

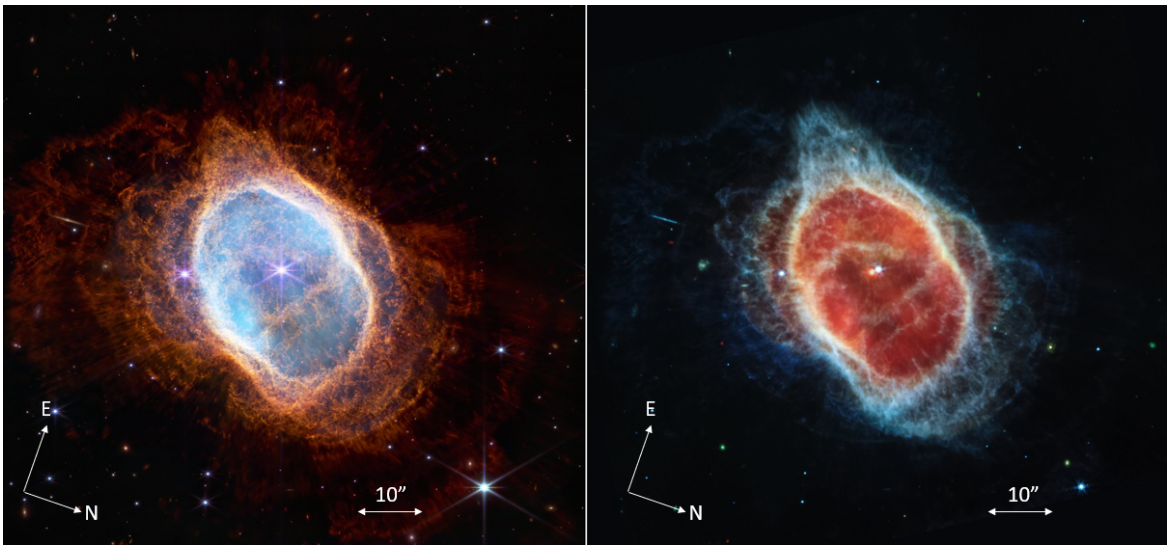

Figure 2.3: James Webb Space Telescope (JWST) image of Planetary Nebula NGC 3132. Left: NIRCam instrument (near-infrared) Right: MIRI instrument (mid-infrared)

NIRCam 2.3 (left panel), scattered outflows spread at interstellar medium as well as dense clumps of molecular gas are present.

Through the extended analysis of JWST data by De Marco et al. (2022), it was suggested the existence of at least a quadruple system in the center of the nebula. Furthermore, it was estimated that the progenitor, when it was in the Main Sequence phase, had mass $2.86 \pm 0.06\, M_{\odot}$.

Chapter 3

Spectroscopic analysis of the NGC 3132

1. Integral Field Spectroscopy

Figure 3.1: The ESO Very Large Telescope (VLT) during observations.

Our analysis started with data obtained by MUSE (Multi Unit Spectroscopic Explorer) instrument which is mounted on VLT (Very Large Telescope), in Chile (Figure 3.1). NGC 3132 was observed on 19 February 2014 and the data was later given to the scientific community from ESO (European Southern Observatory) (Bacon et al., 2014).

Integral Field Spectroscopy is an innovative technology that provides spectroscopic data in two dimensions or, in other words, imaging spectroscopy. It has been used to observe and study various extended objects like galaxies, HII regions (Rousseau-Nepton et al., 2018) or planetary nebulae (Ali et al., 2016; Akras et al., 2022a,b; Monreal-Ibero and Walsh, 2020). Several IFUs have been developed and mounted on different telescopes covering different wavelengths. For instance, VIMOS and MUSE on VLT, GMOS on Gemini in optical and NIFS on Gemini in near infrared wavelengths.

The outcome from IFUs is a cube of data with two spatial dimensions and one spectral dimension (Figure 3.3). The 2D element of the datacube is called "spatial pixel" (spaxel) in order to be distinguishable from the detector's pixel (CCD camera). A spaxel contains the spectrum of a two-dimensional point. The three-dimensional element of a datacube is called voxel (Figure 3.2).

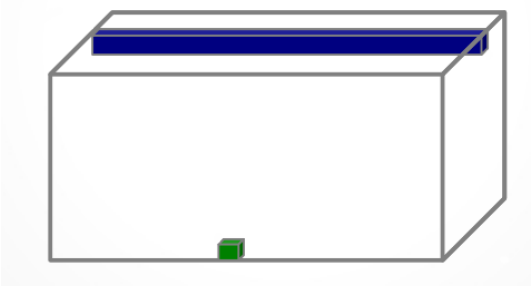

Figure 3.2: A spaxel (Blue) consists of many voxels (Green).

The spectroscopic analysis of extended sources in both spatial dimensions with IFU provide unique information and allow us to study the spatial variation of the physicochemical properties of the ionized gas like electron temperature, electron density and chemical abundances. This chemical analysis was not possible with the traditional long-slit spectroscopy. The advantage of IFU over long slit is discussed in Akras et al. (2022a,b).

2. Extracting 2D emission line maps from IFU datacubes

Emission line maps can be extracted from the datacube fitting a Gaussian profile and subtracting the continuum emission, using a Python

code (Figure 3.3). Fitting the Gaussian distribution, wavelengths before and after the central one are being used. Simultaneously, with emission line maps, emission line error maps are being extracted from the datacube. These error maps mainly depend on the instrument precision, the brightness of the target and the exposure time of the observations.

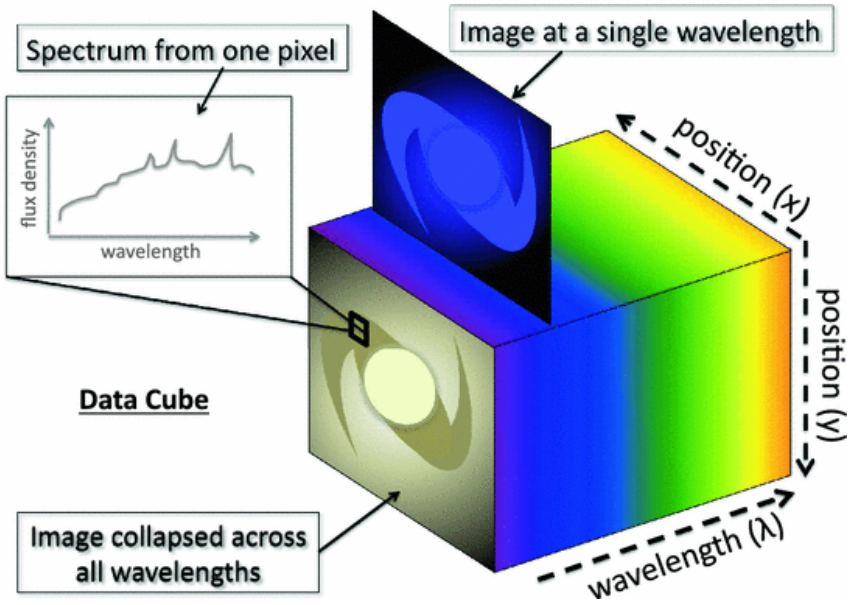

Figure 3.3: The datacube of a galaxy as produced by an Integral Field Unit.

Some main mechanisms for broadening emission lines are mentioned below.

1. Natural Broadening

   Heisenberg's energy-time uncertainty. The uncertainty in energy (wavelength) ΔE is related to the uncertainty in energy state's lifetime Δt.

2. Doppler Broadening-Thermal Broadening

   Relative to the observer movements of atoms and ions. The wavelength of radiation which is emitted from atoms moving away from the observer becomes redder, while if the atoms are moving towards the observer it becomes bluer. The random movements of the atoms is related with the temperature, that's why this mechanism is also called thermal broadening.

3. Collisional Broadening

Collisions between atoms or ions can provide or remove small amounts of energy. This results in photons with a larger range of energies or wavelengths.

3. SATELLITE python code

For the spectroscopic analysis of NGC 3132 the SATELLITE python code was used, which is developed by Akras et al. (2020); Akras et al. (2022b). More specifically, this code calculates the interstellar extinction ($c(H_\beta)$), electron temperature (T_e), electron density (N_e) and chemical composition (ionic and total abundances) in 1D and 2D space. In addition, it calculates ICFs (Ionization Correction Factors) which are necessary for the calculation of total elemental abundances as well as some emission line ratios which are used for the characterization of PNe and investigation of the dominant heating mechanism, UV photons or shocks.

SATELLITE code has four different modules for conducting a more thorough analysis of extended sources:

1. Angular Analysis Module
2. Radial Analysis Module
3. Specific Slit Analysis Module
4. 2D Analysis Module

The program needs as input the emission lines and error maps which have been extracted from an IFU's datacube. Additionally, the code needs:

1. Energy parameter of the IFU i.e., the number which each pixel value from the map is multiplied in order to transform it to energy flux units ($\frac{erg}{cm^2 \cdot sec}$).
2. Pixel scale i.e. the angular distance which corresponds to one pixel on the emission map. ($pixel\ scale = \frac{angular\ distance(arcsec)}{pixel}$).
3. The coordinates x, y (in pixel) of the CSPN on the emission line map.

SATELLITE simulates 1D spectra, creating pseudo-slits with different sizes and orientation. In this way, it's possible to reproduce 1D spectra that resemble those from long-slits and compare the results with previous studies.

All the uncertainties of the physical parameters are calculated through Monte Carlo approach.

3.1. Angular Module

In this module it's possible the study of the variation for physical parameters of the nebular gas, as a function of the position angle (P.A.) of the pseudo-slits, as well as the comparison with previous long slit studies.

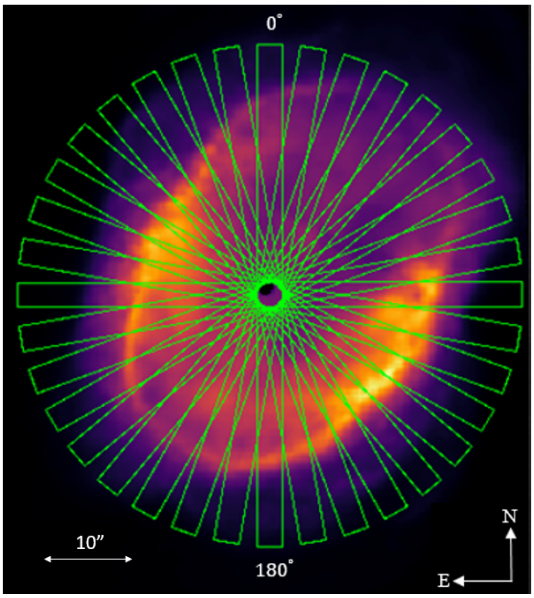

Figure 3.4: An illustrative image of the positioned pseudo-slits with PA from 0 to 360 every 10 degrees overlaid the Hα image of NGC 3132.

The user can choose the dimensions of the pseudo-slit and which parameters will be calculated (Figure 3.4). The minimum and maximum angle of the position angle (P.A.) of the pseudo-slit can also been set by the user, as well as the step. Finally, physicochemical parameters computed by SATELLITE are presented in plots as functions of the P.A. of the pseudo-slit and are saved in ASCII files, so the user can generate his own plots.

3.2. Specific Slit Module

In this module it is possible the study of the physical parameters of specific regions in the nebula, that the user decides (e.g. knots or parts of the nebula).

The user can again set the pseudo-slit's dimension, such as the P.A. and its position (Figure 3.5). The results of all the physical parameters, are saved once again in ASCII files. It has to be mentioned that the results from each pseudo-slit correspond to the integrated emission from the whole structure.

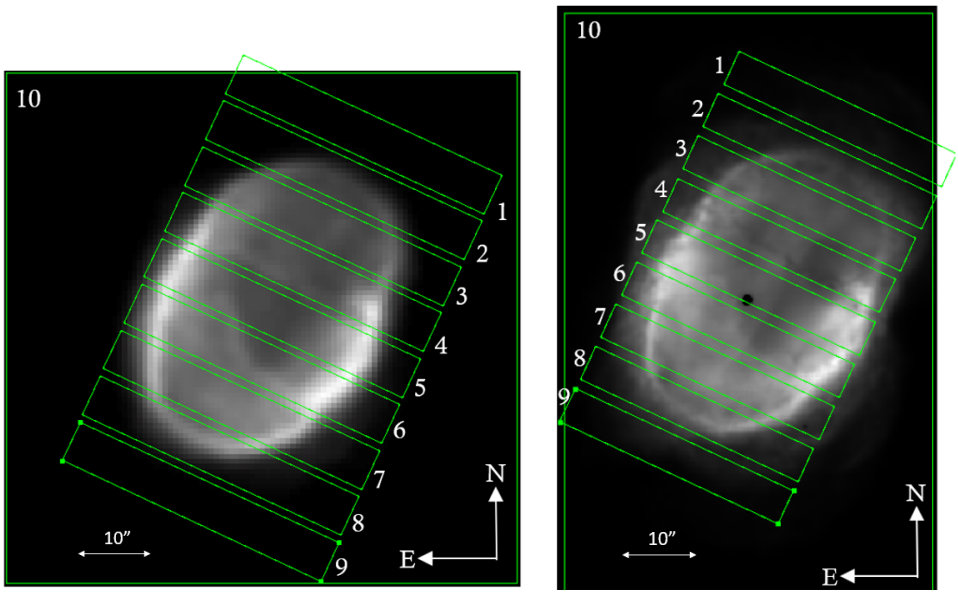

Figure 3.5: Ten selected regions in NGC 3132 overlaid on the Hα map of the photoionization model (left panel) and as captured from MUSE (right panel).

In addition, this module fully simulates the long-slit method, since the user can place pseudo-slits on the exact regions where traditionally long slits were placed in previous studies.

3.3. Radial Module

In this module, the spectroscopic analysis of the nebula carries out a radial analysis of the extended objects. For the case of PNe, SATELLITE perform an analysis from the center to the outer parts. In this way,

a better understanding of inner and outer structure (stratification) of ionized gaseous nebulae is possible.

The user can set dimensions and the angle of the pseudo-slit, which starts from the central star, as well as the physical parameters he/she wants to be calculated. Similar to the previous modules, the results are saved in ASCII files. Plots of the physical parameter as functions of the distance from the CSPN are also generated by the SATELLITE.

3.4. 2D Module

In this module, at each pixel of the emission line maps, every physical parameter is calculated. The results are 2D maps of all the physical parameter's distribution, alongside the nebula. Extended study of these maps, can reveal many secondary structures in the sources under investigation.

This is the most time-consuming module of SATELLITE, but the one which contains the most possible information from an extended astronomical object. In this way, all the information collected from an IFU like MUSE are provided for a thorough analysis of the sources.

4. 3D Photoionisation Model

As we mentioned in previous section, the 3D structure of NGC 3132 has been studied using photoionization models (Monteiro et al., 2000; Baessgen et al., 1990) (Figure 3.6). The goal of this part of my thesis is the comparison of the observed modelled results in 2D terms to improve the model of the nebula. The model emission line maps were used as input to the SATELLITE code. The comparison of the SATELLITE results from the MUSE and modelled line maps will allow us to constrain some of the free parameters of the model.

In this way, the evaluation of the photoionization models and how good the model represents the physical reality is possible.

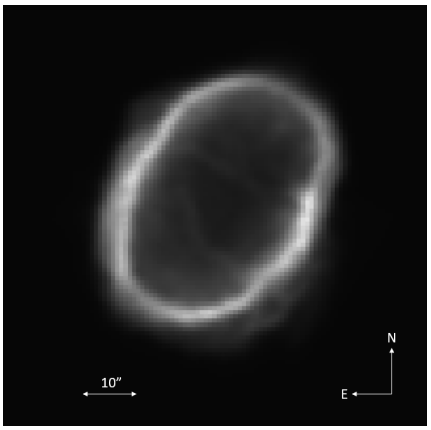

Figure 3.6: [N II] 6583 Å map from the 3D photoionisation model of NGC 3132.

5. JWST DATA

Besides the MUSE data, we decided to use the recent observations of NGC 3132 from the JWST obtained in July 2022 (Pontoppidan et al., 2022).

JWST is equipped with two imagers, MIRI and NIRCam. NIRCam cover wavelengths from $0.6 - 5\,\mu m$ and MIRI from $5 - 28\,\mu m$. In the following subsection, we briefly describe the two main instruments of JWST.

5.1. NIRCam instrument

NIRCam is the main imager of the JWST and it operates at near infrared wavelengths.

Filters F090W, F187N and F212N belong to Short Wavelength Channel, while the F356W, F405N and F470N belong to Long Wavelength Channel. In Table 3.1, we provide information of the filters used to observe NGC 3132. Potential lines covered by these filters are shown in the fourth column. The transmission curves for all the available filters in NIRCam instruments is shown in Figure 3.7.

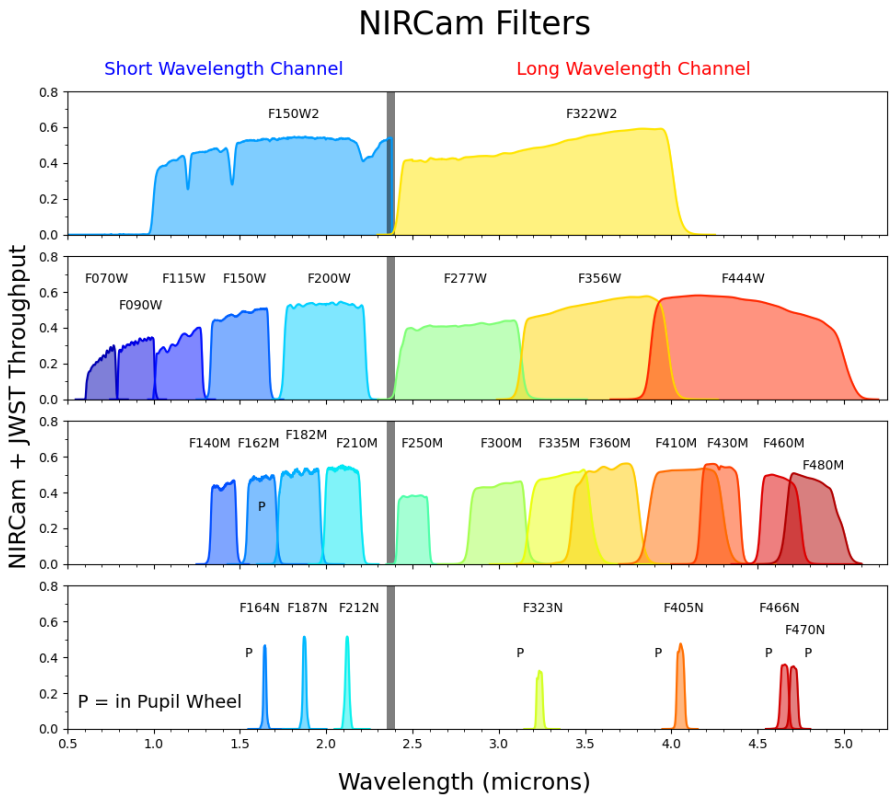

Figure 3.7: Transmission curves for each NIRCam filter.The vertical gray bar marks the cutoff between the short and long wavelength channels.

Filter name	$\lambda_0(\mu m)$	$\Delta\lambda(\mu m)$	Usage
F090W	0.901	0.194	[S III]
F187N	1.874	0.024	Pa-α
F212N	2.12	0.027	H_2
F356W	3.563	0.787	H_2, PAH
F405N	4.055	0.046	Br-α
F470N	4.707	0.051	H_2

Table 3.1: Table of NIRCam filters used for NGC 3132 observations. PAH is an abbreviation for Polycyclic Aromatic Hydrocarbons.

5.2. MIRI instrument

MIRI (Mid-Infrared Instrument), consists of a camera (MIRIM) and a spectrograph (MRS) which operates at mid infrared wavelengths. Several broadband filters are available for the camera (Figure 3.8). In Table 3.2

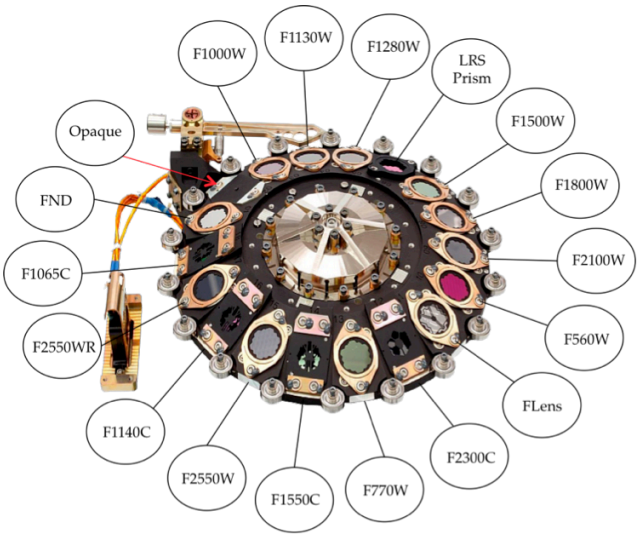

Figure 3.8: The filter wheel on MIRI JWST

the most characteristics emission lines covered by the filter used for the observations of NGC 3132 are listed.

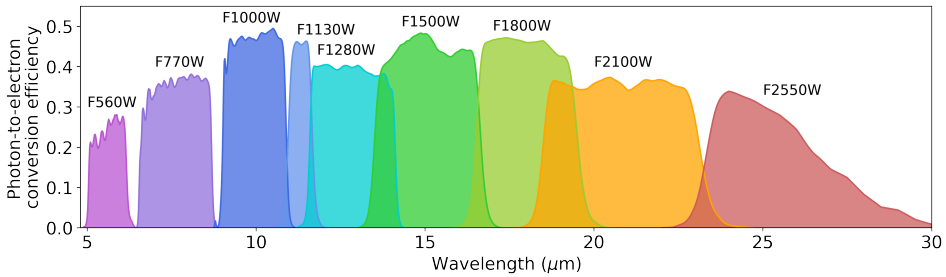

Figure 3.9: Broadband Filters available on MIRI

Filter name	$\lambda_0(\mu m)$	$\Delta\lambda(\mu m)$	Usage
F770W	7.7	2.2	H_2, PAH
F1130W	11.3	0.7	PAH
F1280W	12.8	2.4	[Ne II]
F1800W	18.0	3.0	[S III]

Table 3.2: Table of MIRI filters used for NGC 3132 observations. PAH is an abbreviation for Polycyclic Aromatic Hydrocarbons.

5.3. Radial Analysis of the JWST images

It is known that there is a link between low ionization lines and H_2 lines (Akras et al., 2017; Akras et al., 2020; Akras et al., 2020; Fang et al., 2018). This motivated us to look for this correlation using data from MUSE and JWST. For this exercise, we used the F090W, F187N, F212N, F356W, F405N, F470N, F770W, F1130W, F1280W and F1800W JWST images to compute the radial profiles of the emission along the East, West, North and South directions. An area of 1 arcsec width and 50 arcsec length was considered.

6. Hubble Space Telescope Data

Hubble Space Telescope (HST) launched in 1990 and still remains in operation. From HST archive we were able to retrieve observational data for NGC 3132, which was obtained on 07/12/1995 from WFPC2 instrument (Wide Field and Planetary Camera 2). The available filters for this observation are listed in the Table 3.3, while their transmission curves are shown in Figure 3.10.

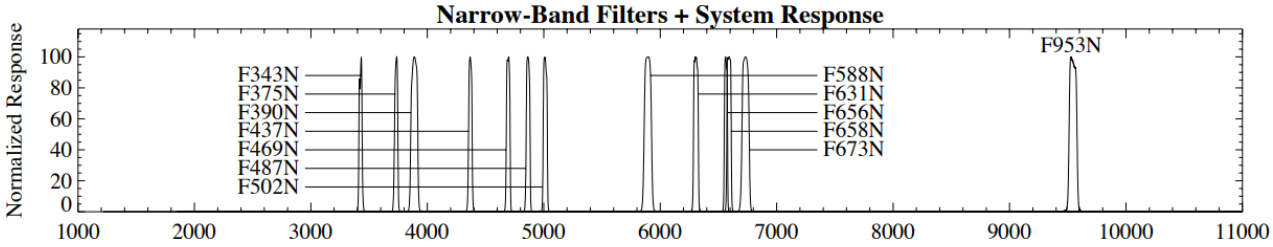

Figure 3.10: HST filters transmission curve.

This filters correspond to some of the brightest emission lines for PNe like [O III] and Hα and cover the optical part of the spectrum. As stated before, from these data we created an RGB image of the NGC 3132 using a python code which we developed.

Name	λ_0(Å)	$\Delta\lambda$ (Å)	Usage
F502N	5012	26.9	[O III] 5007 Å
F631N	6306	30.9	[O I] 6300 Å
F656N	6564	21.5	Hα 6563 Å
F658N	6591	28.5	[N I] 6584 Å
F502N	6732	47.2	[S II] 6731 Å

Table 3.3: HST filters used for NGC 3132 observation.

7. Spitzer data

SPITZER space telescope (SST) was an infrared space telescope launched in 2003. The telescope is named after the astronomer Lyman Spitzer. One of the three instruments that SPITZER was equipped was the Infrared Array Camera (IRAC). This infrared camera was operating simultaneously in four different bands 3.6 μm, 4.5 μm, 5.8 μm and 8.0 μm (Figure 3.11).

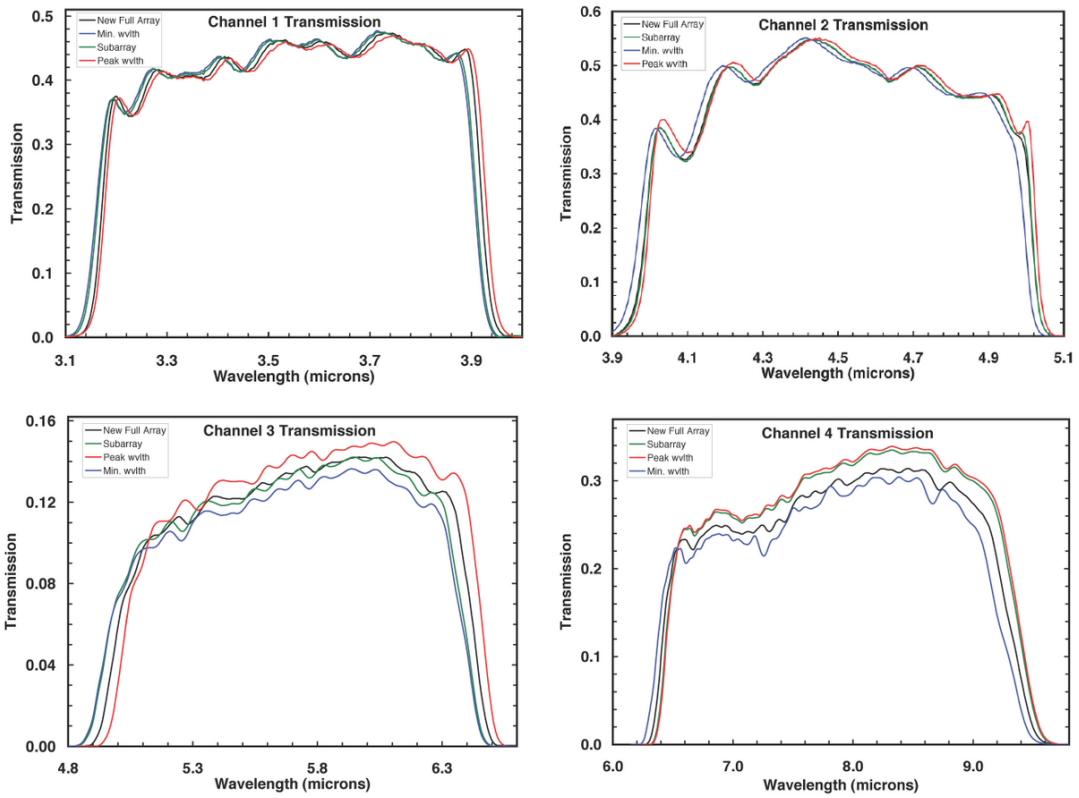

Figure 3.11: Spectral response curves for all four IRAC channels.

Spitzer images by IRAC has been used by authors to study objects in near infrared regime before JWST. Mata et al. (2016) made a spectroscopic analysis with Spitzer data in several PNe, including NGC 3132. In his research, H_2 and several ionic emission lines like [Ar III], [S IV], and [Ne II] were identified in the mid-infrared spectrum of NGC 3132 (Figure 3.12).

The 3^{rd} and 4^{th} bands (Table 3.4) have been considered as an indicator of the presence of molecular gas and stellar objects with that excess in that channels are known as "green fuzzies" (Akras et al., 2020; Phillips et al., 2010). We therefore decided to perform a similar radial analysis on the IRAC images and look for potential links between H_2 and IRAC profiles.

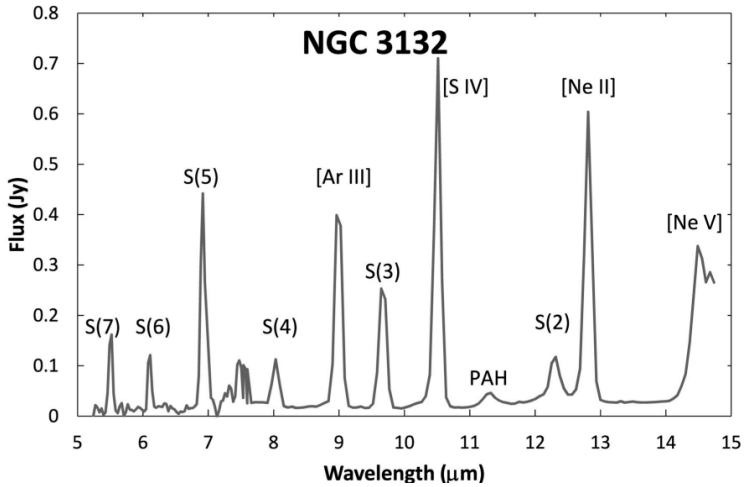

Figure 3.12: NGC 3132 mid infrared spectrum as it was captured by SPITZER space telescope. Several H_2 and ionic lines are identified.

With Spitzer data we performed the same radial analysis in four directions (up, left, down, right) as we did with JWST data. We analysed radially each individual channel in a region with 1 arcsec width and 50 arcsec length. Finally, we compared these results with the previous ones.

Channel	effective λ (μm)	Bandwidth	Peak Transmission
1	3.551	0.750 (21%)	0.465
2	4.493	1.010 (23%)	0.535
3	5.730	1.420 (25%)	0.170
4	7.873	2.930 (37%)	0.318

Table 3.4: Channels characteristics of the SPITZER space telescope.

Chapter 4

Results

1. MUSE results through SATELLITE code

As we explained before, we extracted the emission line maps from MUSE datacube by fitting a Gaussian profile and extracting the continuum. For instance, Figure 4.1 illustrates the resulted 2D map for Hα 6563 Å emission. Moreover, some already extracted emission lines from Monreal-Ibero and Walsh (2020) were used in this study as well.

1.1. Angular Analysis Results

Angular analysis were performed with pseudo-slits as shown in the Figure 3.4. Most of the physicochemical parameters didn't change significant with the P.A. of the slit. However, extinction coefficient c(Hβ) as shown in Figure 4.2 varies significant with the P.A. of the pseudo-slits. More specifically, it gets its higher values for angles around the equator of the nebula ($30^o - 100^o$ and $240^o - 280^o$) and its lower ones around the poles. The fact that the left-hand side has higher values than the right one may be caused by the projection effect.

As far as electron density is concerned, it follows the same behavior as extinction, i.e. higher at the equator and lower at the poles (Figure 4.3). Moreover, electron temperature remains relatively the same with the P.A. of the pseudo-slits (Figure 4.4). From the available wavelength range

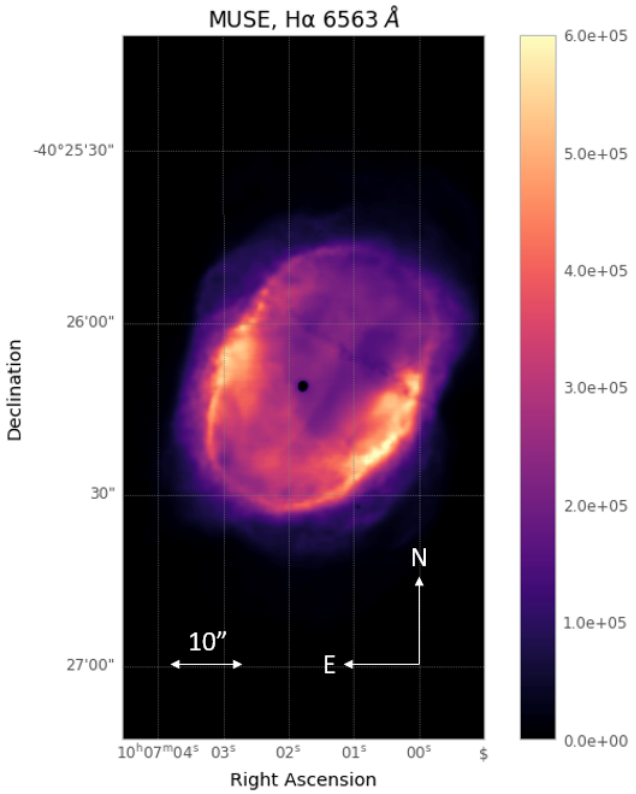

Figure 4.1: Emission map of Hα as extracted from the MUSE datacube.

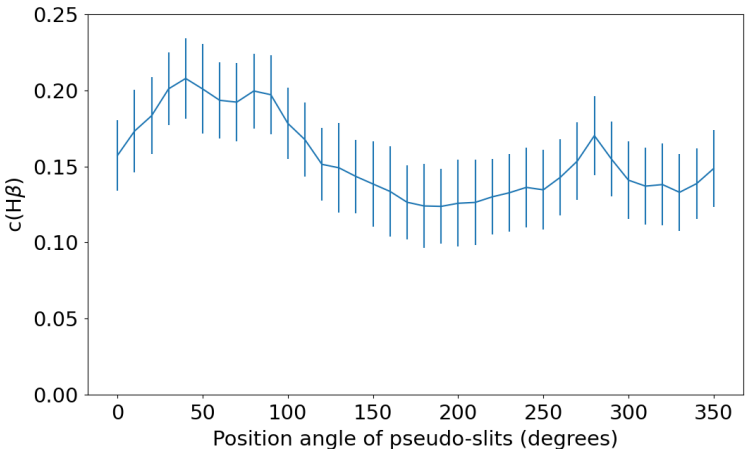

Figure 4.2: Extinction coefficient as function of the P.A. of the slit.

from MUSE Ne[S II] and Te[N II] represent the low ionization region, while Ne[Cl III] and Te[S III] represent the high ionization one.

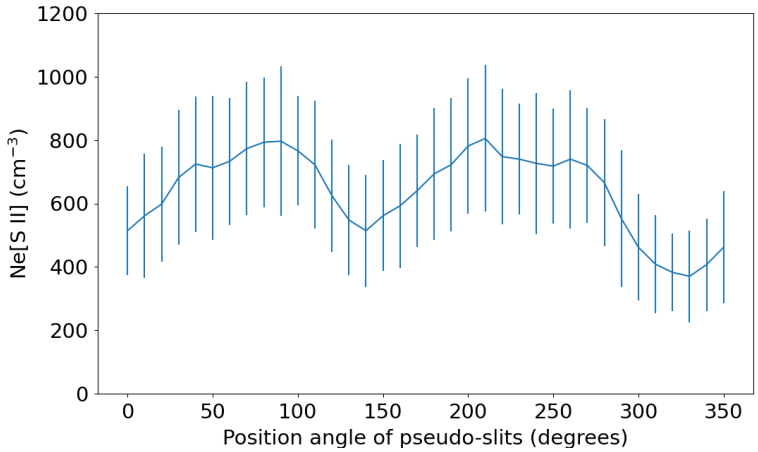

Figure 4.3: Electron density as calculated from [S II] with the P.A. of the pseudo-slits.

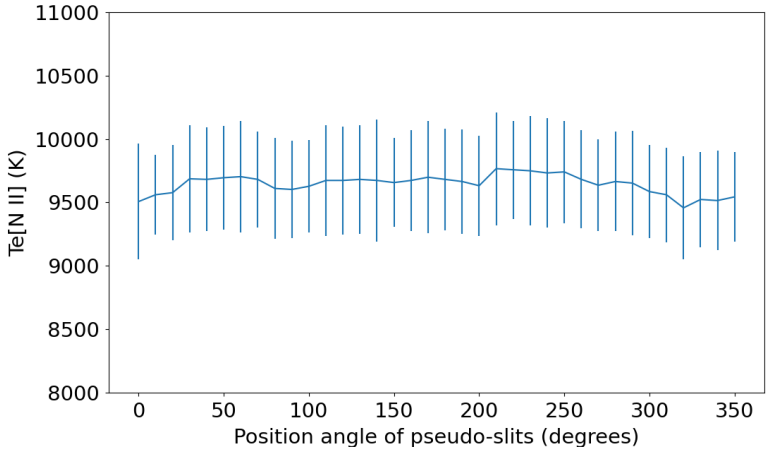

Figure 4.4: Electron temperature as calculated from [N II] with the P.A. of the pseudo-slits.

1.1.1. Model Results

The 3D photoionization model in general recreates well the observational data from MUSE. However, it underestimates a little the electron density (Figure 4.5) and it overestimates the electron temperature (Figure 4.6).

Furthermore, diagram 4.7 shows the total Oxygen abundance between model and data as well as the abundance that was used as input for the 3D photoionization model. The two abundances are pretty similar but considerably higher than the input-abundance. It's clear that using

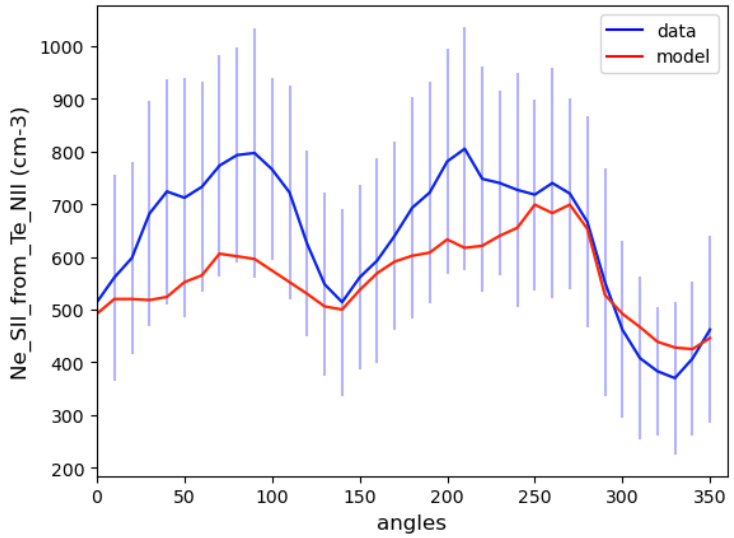

Figure 4.5: Electron density from [S II] with the P.A. of the pseudo-slits as estimated from MUSE data (blue) and the model (red).

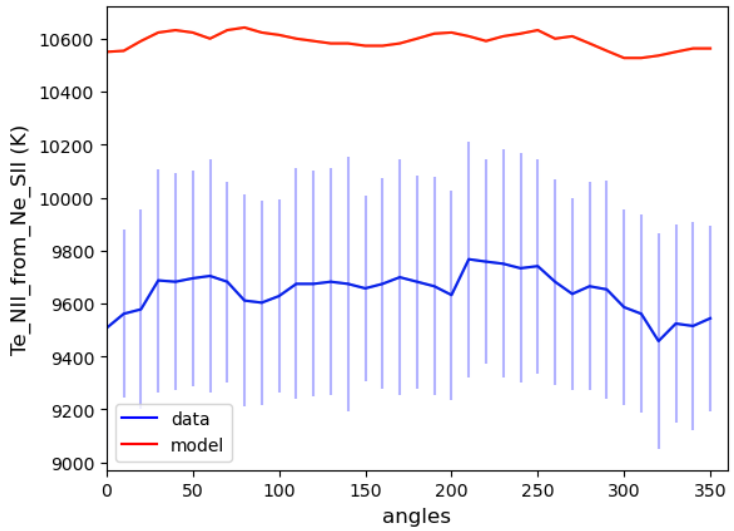

Figure 4.6: Electron temperature from [N II] with the P.A. of the pseudo-slits as estimated from MUSE data (blue) and the model (red).

the ICFs from Delgado-Inglada et al. (2014) the Oxygen abundance is overestimated.

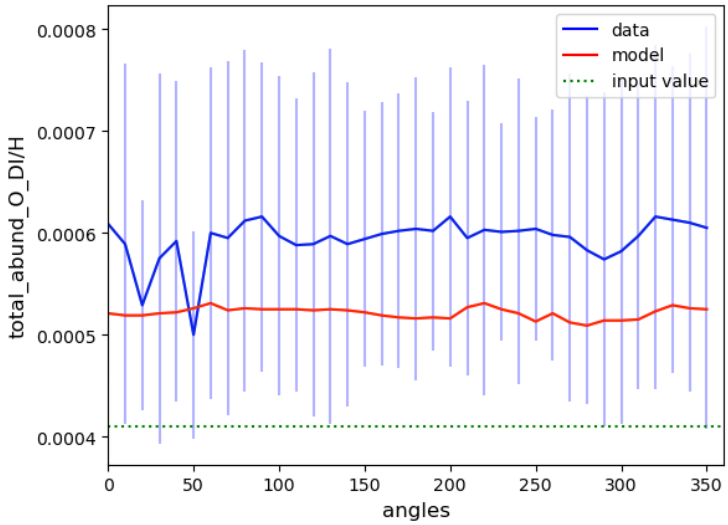

Figure 4.7: Total Oxygen abundance as estimated from MUSE data (blue) and the model (red), the dotted green line corresponds to the abundance that was used as input for the model.

1.2. Specific Slit Analysis Results

For the Specific Slit Analysis module, we chose 10 pseudo-slits for the MUSE data and for the model (Figure 3.5). The main purpose of this task was to investigate in more detail in which regions the model represent the physical reality good enough and where it needs to be improved.

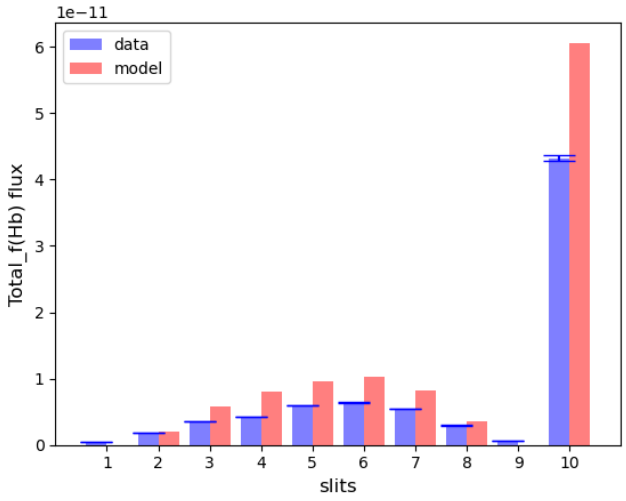

Figure 4.8: Total Hβ flux for each pseudo-slit as estimated from MUSE data (blue) and the model (red).

First, we checked whether the total Hβ flux is comparable between MUSE data and the model. As Figure 4.8 illustrates, the model constantly overestimates the Hβ flux in the small central regions (no. 3-7) as well as in the wider slit (no. 10) which covers the entire nebula.

For the N_e and T_e the model underestimates the electron density (Figure 4.9) and it overestimates the electron temperature (Figure 4.10), exactly as in the Angular Analysis module.

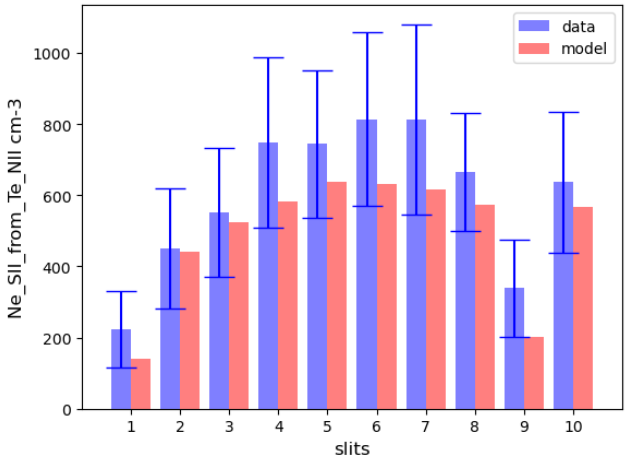

Figure 4.9: Electron density from [S II] for each pseudo-slit as estimated from MUSE data (blue) and the model (red).

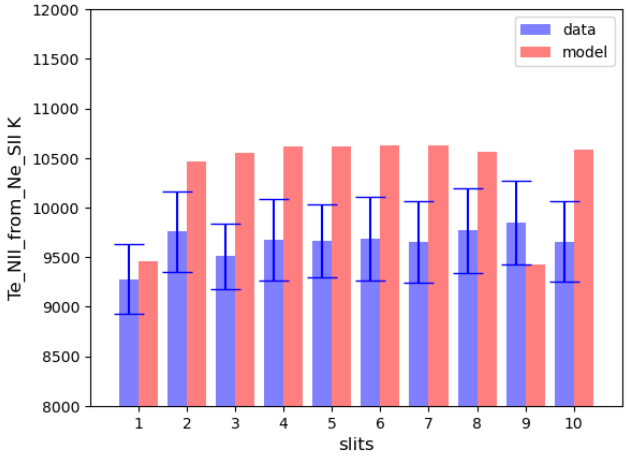

Figure 4.10: Electron temperature from [N II] for each pseudo-slit as estimated from MUSE data (blue) and the model (red).

Moreover, the total Oxygen abundance is illustrated in Figure 4.11 comparing model and data once again. The abundances are pretty close

with each other within error. It is worth mentioning, that in this case the abundances aren't significant above the one used as input for the model.

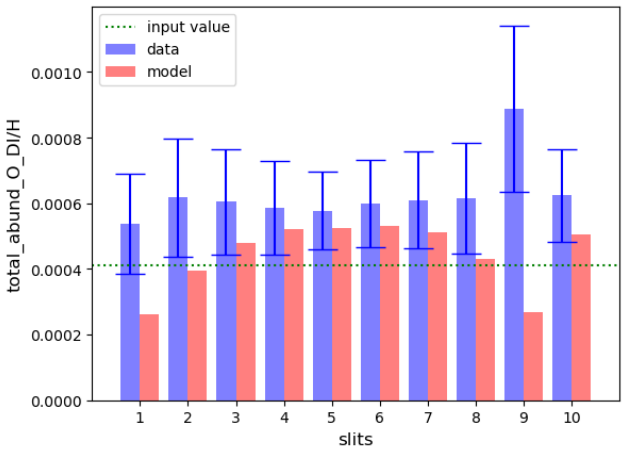

Figure 4.11: Total Oxygen abundance as estimated from MUSE data (blue) and the model (red), the dotted green line corresponds to the abundance that was used as input for the model.

1.3. Radial Analysis Results

A radial analysis was also carried out with a slit $1" \times 30"$ in four orientations 0^o, 90^o, 180^o and 270^o. Below we present only the results for P.A. 270^o, i.e. West from the central star. Starting with the extinction c(Hβ), as shown in Figure 4.12, it clearly peaks at the inner part of the rim ($\sim$17") and at the outer part of the rim ($\sim$22") while it remains constant in the central part of the nebula.

A similar radial profile is shown in Figure 4.13 for electron density, which peaks only at the inner part of the rim. Furthermore, electron temperature remains relatively the same alongside the nebula, with a slight dip around $\sim$14" and a small peak at $\sim$22" (Figure 4.14).

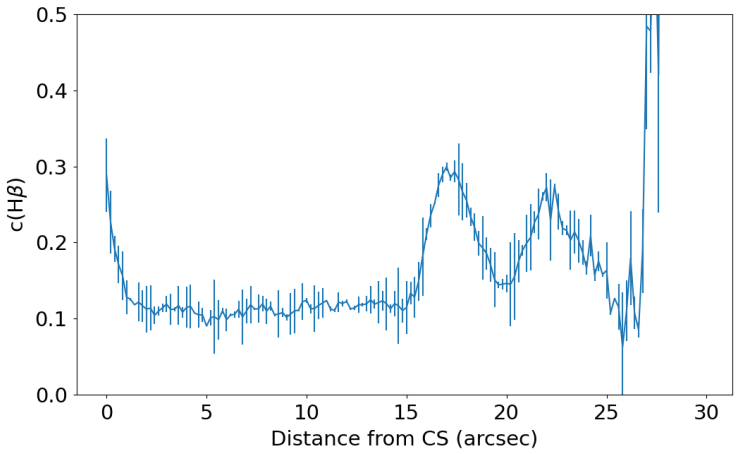

Figure 4.12: Extinction variation with the distance from the central star.

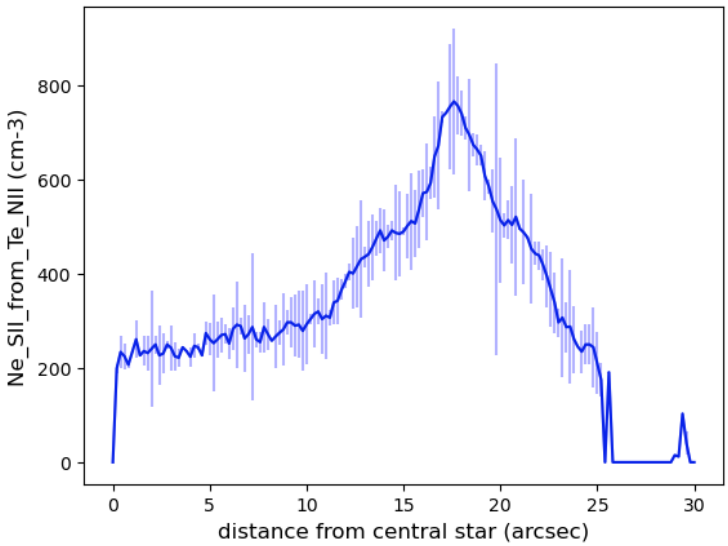

Figure 4.13: Electron density from [S II] with the distance from the central star.

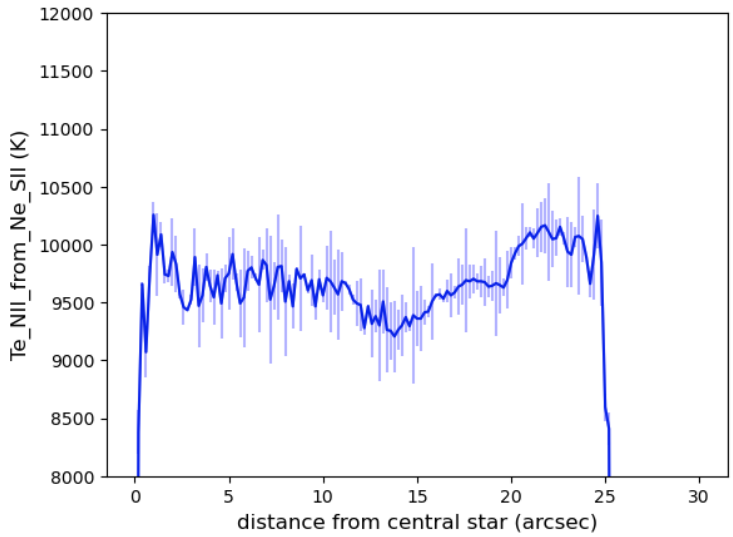

Figure 4.14: Electron temperature from [N II] with the distance from the central star.

1.3.1. Model Results

Again, we performed a radial analysis with the same configuration as above for the photoionization model. We focused our analysis on the West side of the nebula, mostly because of its complicated structure.

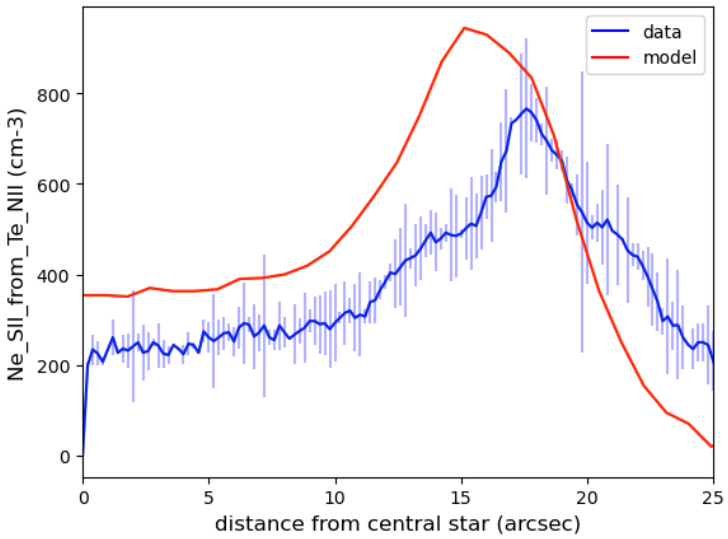

Figure 4.15: Electron density from [S II] with the distance from the central star as estimated from the model (red) and MUSE data (blue).

While the radial profile of electron density matches pretty well with the one from MUSE data as shown in Figure 4.15, the electron temperature's profile is quite different from the MUSE's one (4.16). More specifically, both electron density and temperature of the model are higher than the data. Moreover, model's density peaks before than the MUSE's one (∼2") and model's temperature peaks at the inner rim (∼17") of the nebula while MUSE's temperature seem to peak at the outer rim (∼22").

In addition, the total Nitrogen abundance relative to the distance West of the central star is plotted at Figure 4.17. The model underestimates N abundance by a lot compared to MUSE data, while it is above the abundance value used as input for the model.

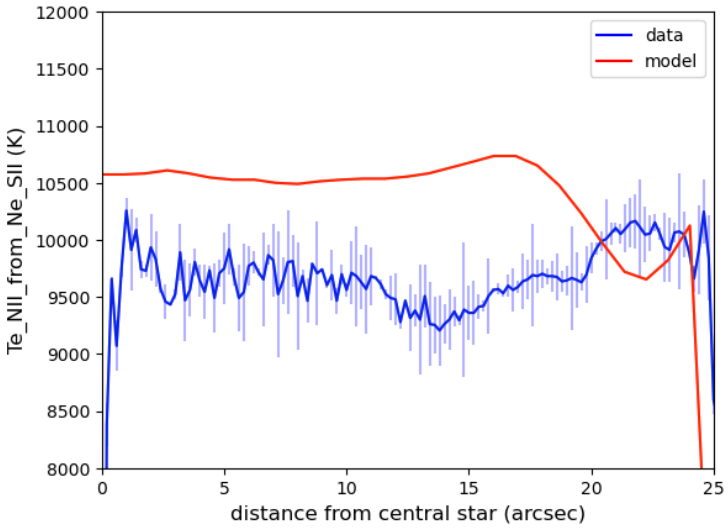

Figure 4.16: Electron temperature from [N II] with the distance from the central star as estimated from the model (red) and MUSE data (blue).

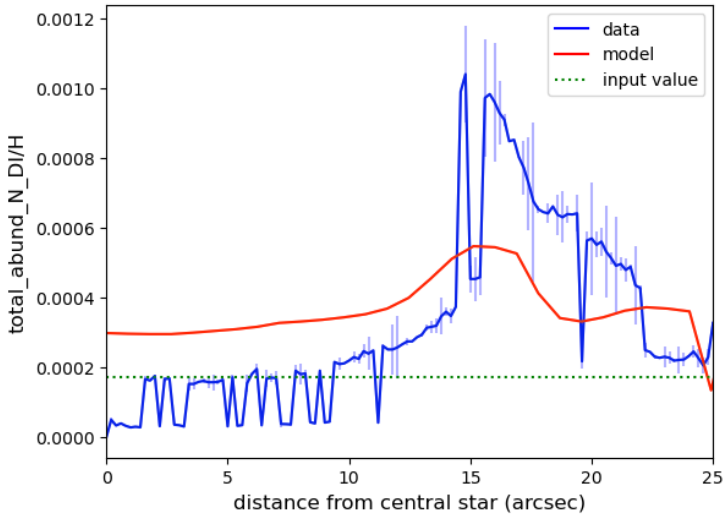

Figure 4.17: Total Nitrogen abundance as estimated from MUSE data (blue) and the model (red), the dotted green line corresponds to the abundance that was used as input for the model.

1.4. 2D Analysis Results

A 2D analysis is carried out using MUSE data through SATELLITE code, as highlighted earlier. Starting with c(Hβ), as it's shown in Figure 4.18 (left panel), it reaches its higher values at the rims of the nebula and especially at the left rim where it takes values as high as 0.5. This difference between left and right rim extinction values may be caused by projection effect. Furthermore, the inner belt-like structure seems to have relatively high values of c(Hβ).

The pixel value distribution from the 2D map is projected on the right panel in Figure 4.18 and at the first column in Table 4.1 there are some useful statistical parameters like median value, mean value and standard deviation (sigma).

Median value is defined as the middle number in an ordered list of values, while mean value refers to the simple average of the given set of quantities. In the case of extinction, mean value is higher than median value, so the distribution is defined as positively skewed.

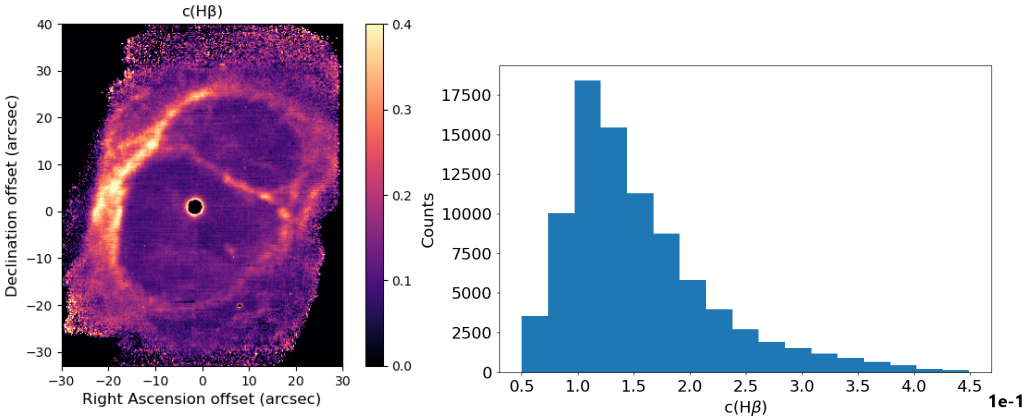

Figure 4.18: Left panel: 2D map for extinction coefficient. Right panel: Histogram for c(Hβ) values.

Electron temperature estimated by [N II] forbidden lines ratio and its pixel value distribution are illustrated in Figure 4.19 left and right panel respectively. Temperature is higher at the rim and outside the nebula, as well as at some visible inner microstructures. In general, the median value is 9,770 K (Table 4.1) which is typical for a planetary nebula.

Electron density calculated by [S II] lines ratio as well as its pixel

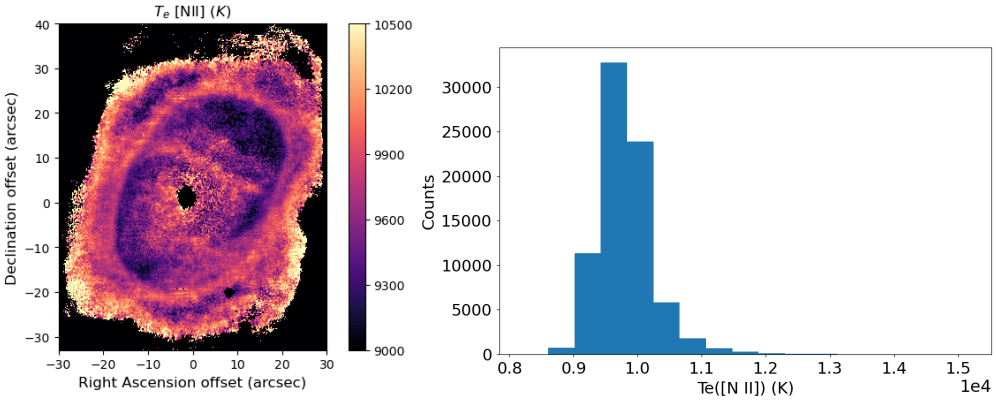

Figure 4.19: Left panel: 2D map for T_e from [N II]. Right panel: Histogram for electron temperature values.

value distribution are shown in Figure 4.20. Like before, density peaks around the rim of the nebula and at some inner structures. Its median value is 400 cm^{-3} and its mean value 391 cm^{-3} (Table 4.1), so its pixel value distribution can be referred as negatively skewed.

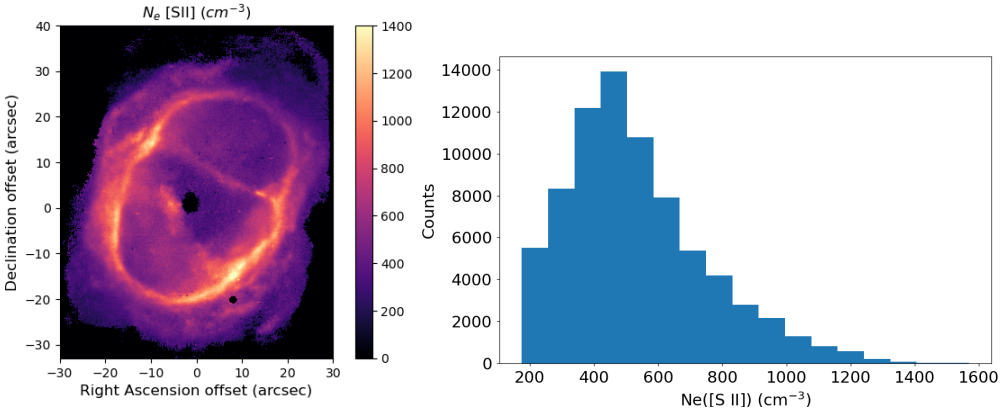

Figure 4.20: Left panel: 2D map for N_e from [S II]. Right panel: Histogram for electron density values.

In Table 4.1 are listed more statistical parameters for T_e[S III] and N_e[Cl III], which represent the high ionization region of the nebula. In comparison with previous results, T_e[S III] is lower than T_e[N II], while N_e[Cl III] is higher compared to N_e[S II]. The Q1 value is the lowest quartile meaning that 25% of the data are below the first quartile. On the contrary, Q3 value is the upper quartile, so 75% of all the data falls below the third quartile.

It is worth mentioning that T_e[S III] and N_e[Cl III] maps have significant smaller set of data than T_e[N II] and N_e[S II]. Given these results, low ionization region results from T_e[N II] and N_e[S II] are more valid.

Name Parameter	No. spaxels	5% Value	Q1 Value	Median Value	Q3 Value	95% Value	Mean Value	Sigma
c(Hβ)	90893	0.0567	0.104	0.134	0.182	0.295	0.150	0.0728
T_e[N II] (K)	77538	9220	9540	9770	10000	10500	9810	423
T_e[S III] (K)	32518	8860	9120	9350	9640	10100	9400	374
N_e[S II] (cm^{-3})	77538	222	370	487	640	954	524	222
N_e[Cl III] (cm^{-3})	32518	172	528	939	1470	2700	1120	828

Table 4.1: Statistics for physical parameters from MUSE data.

In addition, we mapped ionic and total abundances. As expected, ions with higher ionization degree inhabit the main ionized cavity, while ions with lower ionization degree exist around the rims. For example, Figure 4.21 shows how neutral Oxygen is spread through the nebula. Statistical results including all the calculated abundances are shown in Table B′.14.

We have to mention, that all the 2D statistical results for T_e, N_e and ionic abundances are pretty similar with the ones from Monreal-Ibero and Walsh (2020).

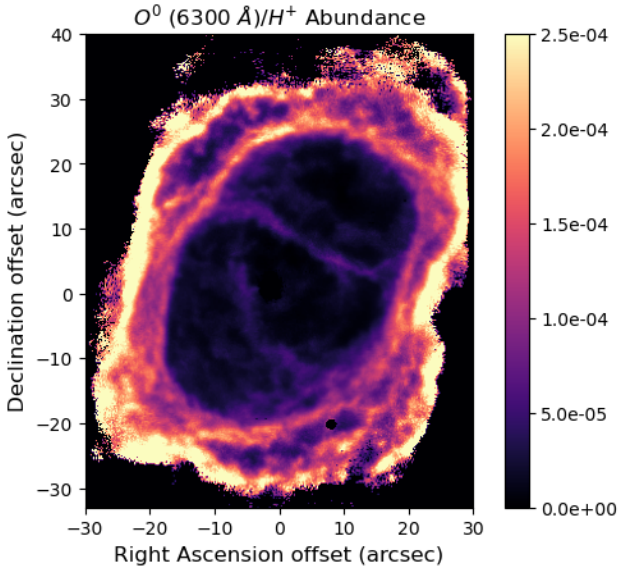

Figure 4.21: Map of neutral Oxygen (6300 Å) abundance for NGC 3132.

Several diagnostic diagrams were also made in order to compare NGC 3132 with typical PNe values. Statistical limits from 613 planetary nebulae were presented by Riesgo and López (2006). These limits were created for integrated values from the traditional long slit method.

Figure 4.22 illustrates log(Hα/[N II]) versus log(Hα/[S II]) in the left panel and log([O III]/Hβ) versus log([S II]/Hα) in the right panel. Cyan dots represent each spaxel value from the 2D map, yellow diamonds represent the pseudo-slit's value created in Specific Slit module and purple circles represent the results from each angle from Angular Analysis module. The diagrams include HII, SNR and PNe regions according to Riesgo and López (2006). Most of NGC 3132 results are inside the PNe region on the left panel, while on the right one there are some dots (mostly cyan) in SNR region. As a reminder, the statistical limits concern only long-slit values, in this case yellow diamonds and purple circles. Individual spaxel results don't necessarily fall into these limits, that's the reason why cyan dots are widely spread. We have to mention, that the two yellow diamonds close or beyond the limits represent the pseudo-slits that are placed far North and far South of the nebula and have a bad Sign to Noise ratio (Monreal-Ibero and Walsh, 2020). As a conclusion, PN NGC 3132 can be defined as a high ionization nebula.

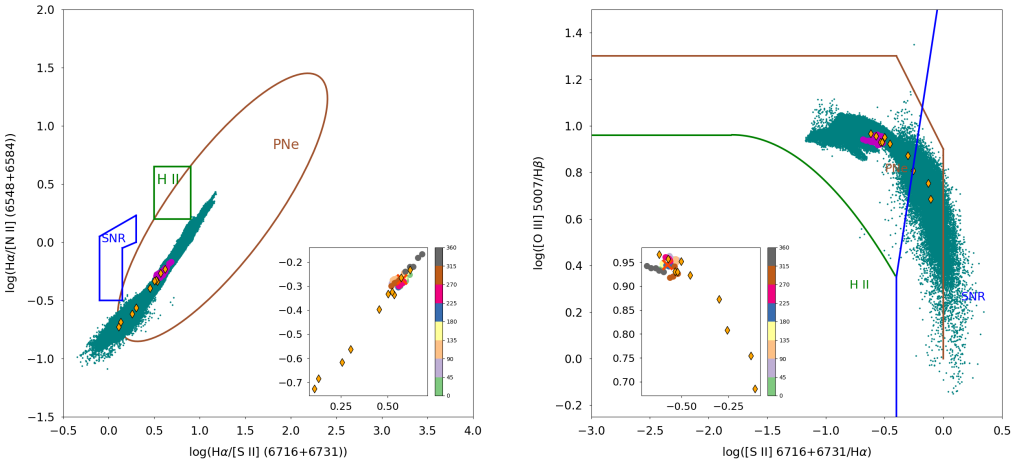

Figure 4.22: Diagnostic diagrams for NGC 3132. Cyan dots represent each spaxel value, yellow diamonds represent the pseudo-slit's value created in Specific Slit module and purple circles represent the results from each angle from Angular Analysis module.

1.4.1. Model Results

We created two-dimensional maps of the physicochemical parameters for NGC 3132 photoionization model. Electron temperature from T_e[N II] ranges from 8,710 K to 10,500 K and has median value 10,300 K (Table 4.2). It peaks at the rim of the nebula and especially around the equator (Figure 4.23). Some inner structures with lower temperature are also visible. T_e[N II] as estimated from the model is similar with the one from MUSE data.

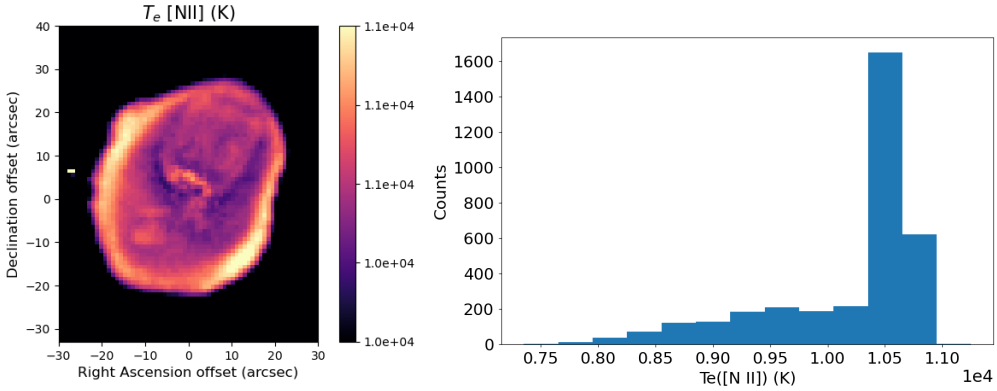

Figure 4.23: Left panel: 2D model map for T_e from [N II]. Right panel: Histogram for electron temperature values.

Electron density N_e[S II] ranges from 73 cm^{-3} to 803 cm^{-3} and has median value 448 cm^{-3} as shown in Table 4.2. Furthermore, the highest values of N_e are found at the rims of the nebula and more specifically around the equator (Figure 4.24). Moreover, it is slightly lower compared to the same density from MUSE data.

Table 4.2 lists the statistics for T_e[S III] and N_e[Cl III]. Temperature values are pretty close with the ones from MUSE data, while density values are considerably lower than MUSE ones. This difference maybe is affected from the small data sample for these calculations (number of spaxels used: 4368 Table 4.2).

Moreover, we mapped the ionic and total abundances of the model and the results are illustrated in Table B′.15. In general, the model's abundances match the MUSE's ones within error.

For further analysis and evaluation of the model, we developed several diagnostic diagrams (Figure 4.25). The left panel in Figure 4.25

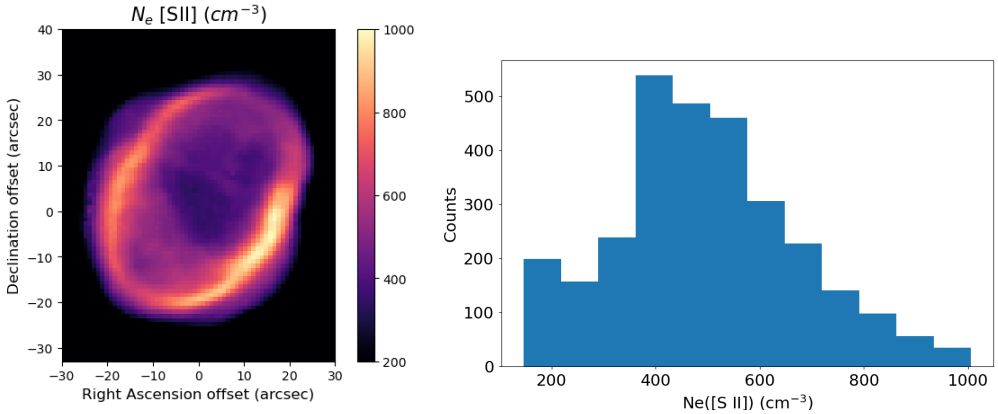

Figure 4.24: Left panel: 2D model map for N_e from [S II]. Right panel: Histogram for electron density values.

Name Parameter	No. spaxels	5% Value	Q1 Value	Median Value	Q3 Value	95% Value	Mean Value	Sigma
T_e[N II] (K)	3438	8680	9910	10600	10600	10700	10200	672
T_e[S III] (K)	4368	6710	8340	9640	9760	9970	9000	1080
N_e[S II] (cm^{-3})	3438	73.2	293	448	578	803	438	216
N_e[Cl III] (cm^{-3})	4368	99.5	161	623	857	1180	570	373

Table 4.2: Statistics for physical parameters from photoionization model.

shows log(Hα/[N II]) versus log(Hα/[S II]), while the right one shows log([O III]/Hβ) versus log([S II]/Hα). The yellow diamonds and the purple circles are in very similar locations compared with MUSE data, however cyan dots, which represent the values of each individual spaxel differ a lot. It is worth noting that HII, SNR and PNe regions on these diagrams were made for integrated values from slits (yellow diamonds, purple circles) and not for individual spaxels (cyan dots).

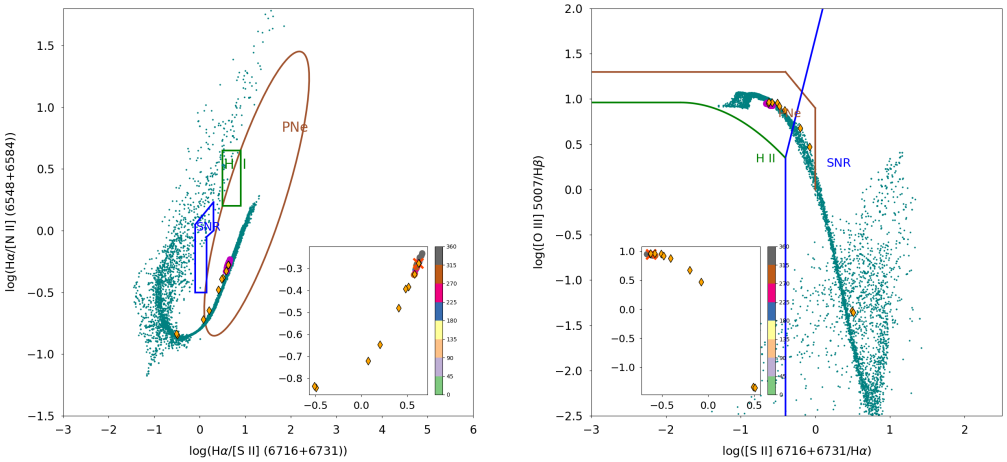

Figure 4.25: Diagnostic diagrams for NGC 3132 from the 3D model. Cyan dots represent each spaxel value, yellow diamonds represent the pseudo-slit's value created in Specific Slit module and purple circles represent the results from each angle from Angular Analysis module.

2. JWST Radial Analysis Results

For the analysis of the JWST data, we built our own python script in order to examine in depth the radial profiles from JWST filters. NIRCam images captured with filters F090W, F187N and F212N (Short Wavelength Channel) have 0.03086" pixel scale while the images captured with the rest of the filters F356W, F405N and F470N (Long Wavelength Channel) have 0.063" pixel scale. So, in order to analyze a region with 1" width, we used 32 pixels for the Short Wavelength Channel and 16 pixels for the Long Wavelength Channel. MIRI images have 0.1109" pixel scale, so we used 9 pixels width for the radial analysis. Furthermore, we rotated NIRCam images by 112^o and MIRI images by 124^o counterclockwise in order to have the same orientation as MUSE's data. Moreover, in this analysis we mention each radial profile peak, but each imager has different accuracy. So, NIRCam's Short Wavelength Channel has ± 0.03" error, NIRCam's Long Wavelength Channel has ± 0.06" error, MIRI has ± 0.11" error and MUSE has ± 0.2" error.

As we mentioned earlier, NGC 3132 expand with typical velocity 25 km/s (Table 1.1). For the best possible comparison between JWST and MUSE results, we have to take into account this expansion. JWST NIRCam observations (Pontoppidan et al., 2022) were performed on 03/06/2022, while MIRI on 12/06/2022 and MUSE on 19/02/2014 (Monreal-Ibero and Walsh, 2020). By using the distance of the nebula $d \sim 754\,pc$ and simple trigonometry (equation 4.1) we calculated the expansion of the nebula. Between MUSE observation and JWST NIRCam the nebula expanded 0.058" (~ 0.0002 pc) and between MUSE and JWST MIRI's observation the nebula expanded 0.058" (~ 0.0002 pc) as well.

$$\tan\left(\frac{\theta}{2}\right) = \frac{l}{2D} \tag{4.1}$$

Where θ is the angular size in arcsec, l is the linear size and D is the distance.

MUSE and NIRCam observations contain the same [S III] 9069Å emission line, which corresponds to F090W NIRCam's filter. This was the first radial profile we compared between the two measurements. Taking into account the nebula's expansion and each measurement random error, the radial profiles peaked at similar distances from the central star as shown in Table 4.4 (Table B′.2,B′.3,B′.4).

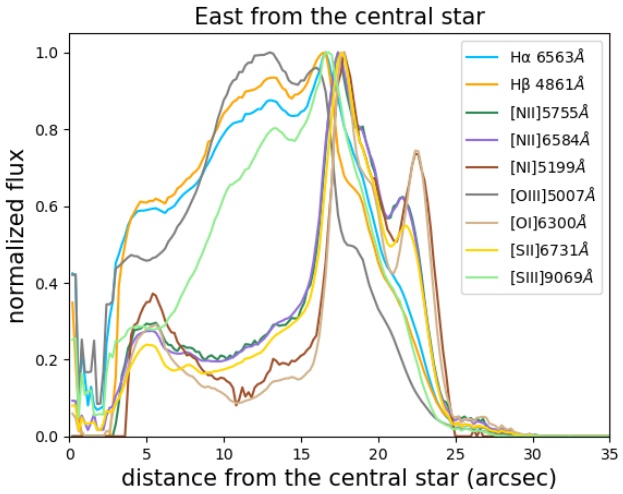

Figure 4.26: SATELLITE's radial analysis module normalized results from MUSE. Each emission line peak is shown in tables 4.3 and 4.4.

In Figure 4.26 the results from SATELLITE's radial analysis module are illustrated and in Figure 4.27, radial profiles of various emission lines from JWST are shown.

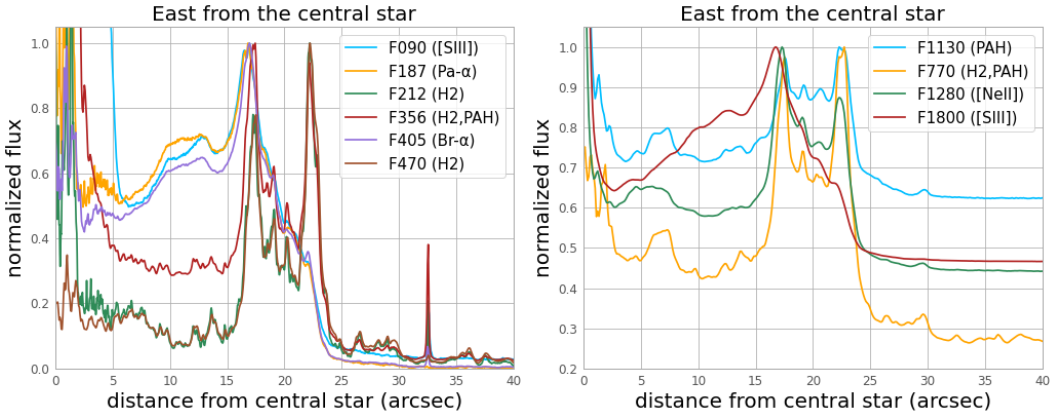

Figure 4.27: Normalized radial profiles from JWST NIRCam (left panel) and MIRI (right panel) East from the central star. Each emission line peak is shown in tables 4.3 and 4.4

The radial profiles reveal the expected nested nebular ionisation structure, wherein the highest ionisation state gas, as traced by [S III], peaks inside the ionised Hydrogen traced by Br-α, and these ionisation zones lie nestled inside the peak H_2 emission.

Radial profiles peak :

High Ionisation lines < Low Ionisation lines < Molecular Lines

The radial intensity profiles of optical emission lines from MUSE show either one peak (high-moderate ionisation lines) or two peaks (low-ionisation lines) in agreement with this data. Low Ionisation lines and Molecular ones from JWST show two peaks (Table 4.3) while High Ionisation lines show only one (Table 4.4).

Emission line	1st peak (arcsec)	2nd peak (arcsec)
Pa-α (F187N)	16.84	22.00
Br-a (F405N)	16.95	22.10
H_2 (F212N)	17.26	22.23
[N II] 5755Å	17.4	21.6
[N II] 6584Å	17.4	21.6
H_2 (F356W)	17.45	22.18
H_2 (F470N)	17.51	22.24
PAH (F1130W)	17.52	22.29
H_2 (F770W)	17.52	22.73
[S II] 6731Å	17.6	21.8
[N I] 5199Å	17.8	22.4
[O I] 6300Å	17.8	22.4

Table 4.3: Radial analysis for low ionisation lines East from the PNe.

It should be noted though that atomic gas, traced by [N I] and [O I], appears to be co-spatial with H_2 gas (Aleman and Gruenwald, 2011; Akras et al., 2017). More specifically, atomic gas lines peak approximately 0.4" further than molecular Hydrogen emission lines (Table 4.3). This difference is attributed to the different spatial resolution of the instruments.

Emission line	1st peak (arcsec)
[O III] 5007Å	16.0
Hα 6563Å	16.6
Hβ 4861Å	16.6
[S III] (F1800W)	16.75
[Ne II] (F1280W)	17.30
[S III] 9069Å	16.8
[S III] (F090W)	16.94

Table 4.4: Radial analysis for high ionisation lines East from the PNe.

2.1. Extinction relation with molecular Hydrogen

It is also worth mentioning that $c(H_\beta)$ obtained from the optical data takes the maximum value at the same positions that H_2 peaks, indicating the presence of dust in these rings. This dust component may prevent the H_2 gas from being dissociated.

Figure 4.28 illustrates the correlation between dust extinction and molecular Hydrogen in four directions East, West, North, and South from the central star. In all of these diagrams, H_2 peaks at the similar distance from the central star with $c(H_\beta)$ except at the inner rim West of the nebula, where an offset of 1.5" is observed. This difference may be caused by projection effect. As we mentioned before, the random errors for NIRCam's Short Wavelength Channel are ± 0.03", for NIRCam's Long Wavelength Channel are ± 0.06" error, for MIRI are ± 0.11" error and for MUSE are ± 0.2".

The exact peaks for molecular Hydrogen emission lines as well as for dust emission peaks East from the central star are shown in Table 4.5 (West, North and South results are shown in tables B′.12 B′.13 and B′.11 respectively).

Emission line	1st peak (arcsec)	2nd peak (arcsec)
c(Hβ)	17.2	22.4
H_2 (F212N)	17.26	22.23
H_2 (F356W)	17.45	22.18
H_2 (F470N)	17.51	22.24
H_2 (F770W)	17.52	22.73

Table 4.5: Radial analysis comparison between c(Hβ) and molecular Hydrogen East from the PNe.

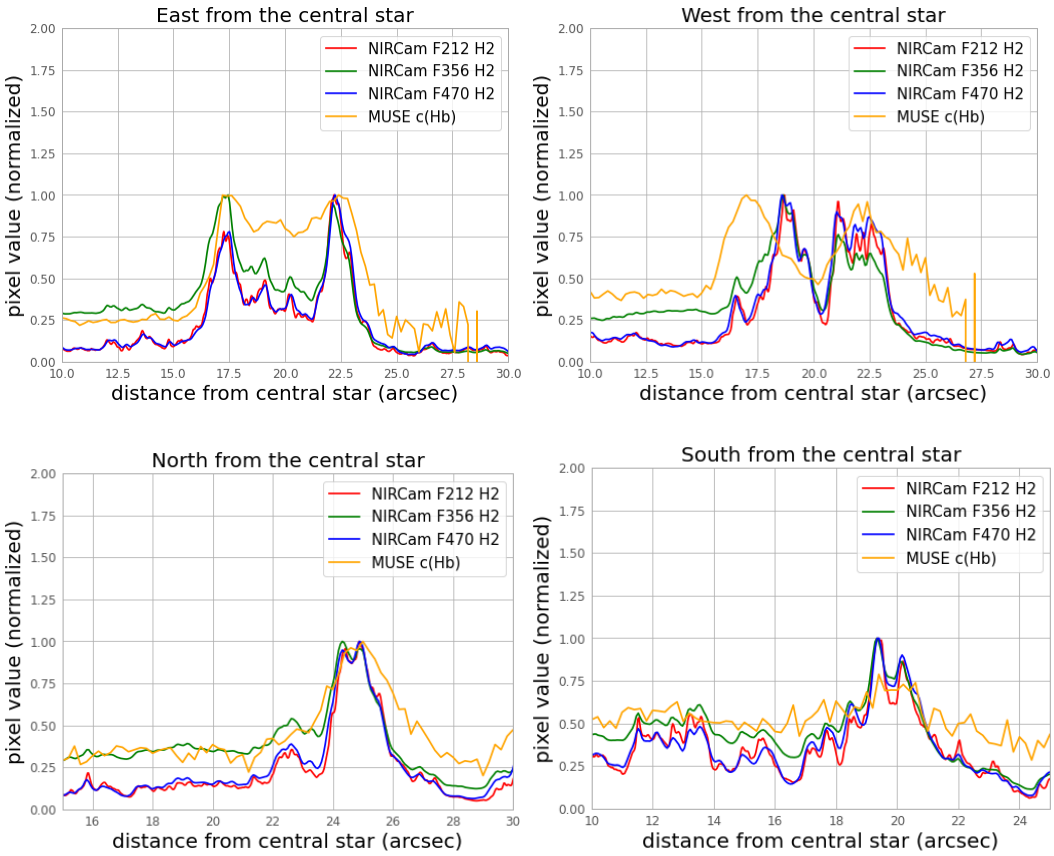

Figure 4.28: Radial analysis for H_2 lines and extinction coefficient East, West, North, and South from the central star.

3. HST Radial Analysis Results

The pixel scale of HST WFPC2 instrument is 0.1", so each measurement has a random error ± 0.1". With such accuracy, both the White Dwarf and the companion star are visible. We performed the same radial analysis in four directions North, South, East, and West from the central star. The region that were used has 1" width which correspond to 10 pixels from WFPC2 instrument.

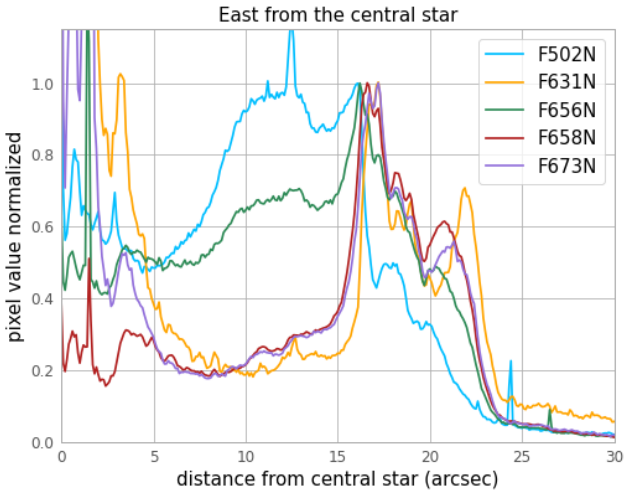

Figure 4.29: HST radial analysis normalized results East from the central star.

Figure 4.29 shows the HST normalized radial profiles East from the central star. All the emission lines peak at the inner part of the rim $\sim$ 17". Moreover, the [O I], [N II] and [S II] emission lines show a second peak at the outer rim of the nebula $\sim$ 21". The exact peaks of the emission lines East from the central star are listed in the Table 4.6, while the results for West, North, and South from the central star are shown in tables B′.5 B′.6 B′.7 respectively.

In order to compare these results with the ones from MUSE we need to take into account the expansion of the nebula between the two observations. Using distance $d = 754\,pc$ and $U_{exp} = 25\,km/s$ and the equation 4.1 we calculated $\sim$0.13 pc expansion between HST and MUSE observations.

Radial profiles from MUSE and HST data are similar North, West, and South from the CSPN. However, MUSE data peak at slightly larger distances than HST ones, but always within error. The biggest offset

Emission line	1st peak (arcsec)	2nd peak (arcsec)
[O III] (F502N)	16.1	-
Hα (F656N)	16.2	-
[N II] (F658N)	16.6	20.8
[S II] (F673N)	17.2	21.3
[O I] (F631N)	17.2	21.9

Table 4.6: Radial analysis for emission lines East from the PNe as captured by HST.

is observed at the East side of the nebula, where [N II] emission from MUSE (Table 4.3) peaks ($\sim$ 0.8") further than HST's one (Table 4.6). This difference may be caused by the coordinates of the starting point (CSPN) for each radial analysis. In comparison, on HST data the CSPN is clearly visible, while on MUSE data it is pretty faint.

4. SPITZER Radial Analysis results

Spitzer space telescope's imager IRAC has accuracy of 0.6" so the random errors for each measurement are ± 0.6". Initially, we rotated the images from the four channels 303.5^o counterclockwise in order to have the same orientation as JWST images. In order to perform the same radial analysis at the same region (1" $\times$ 50") we used 2 pixels as width from Spitzer data.

Furthermore, the expansion of the nebula between Spitzer and JWST observations was estimated using distance d=754 pc, expansion velocity 25 km/s and the trigonometric equation 4.1. The expansion between Spitzer and MIRI observation was found 0.094" as well as the Spitzer-NIRCam one.

In Figure 4.30 the normalized radial profiles of the four channels from IRAC camera are illustrated.

From tables 3.2, 3.1 and 3.4 it is shown that Spitzer's channel 4 transmission curve contains MIRI's F770W, Spitzer's channel 1 contains NIRCam's F356W and Spitzer's channel 2 contains NIRCam's F405N and F470N.

In Table 4.7 we present the exact distance where each channel's

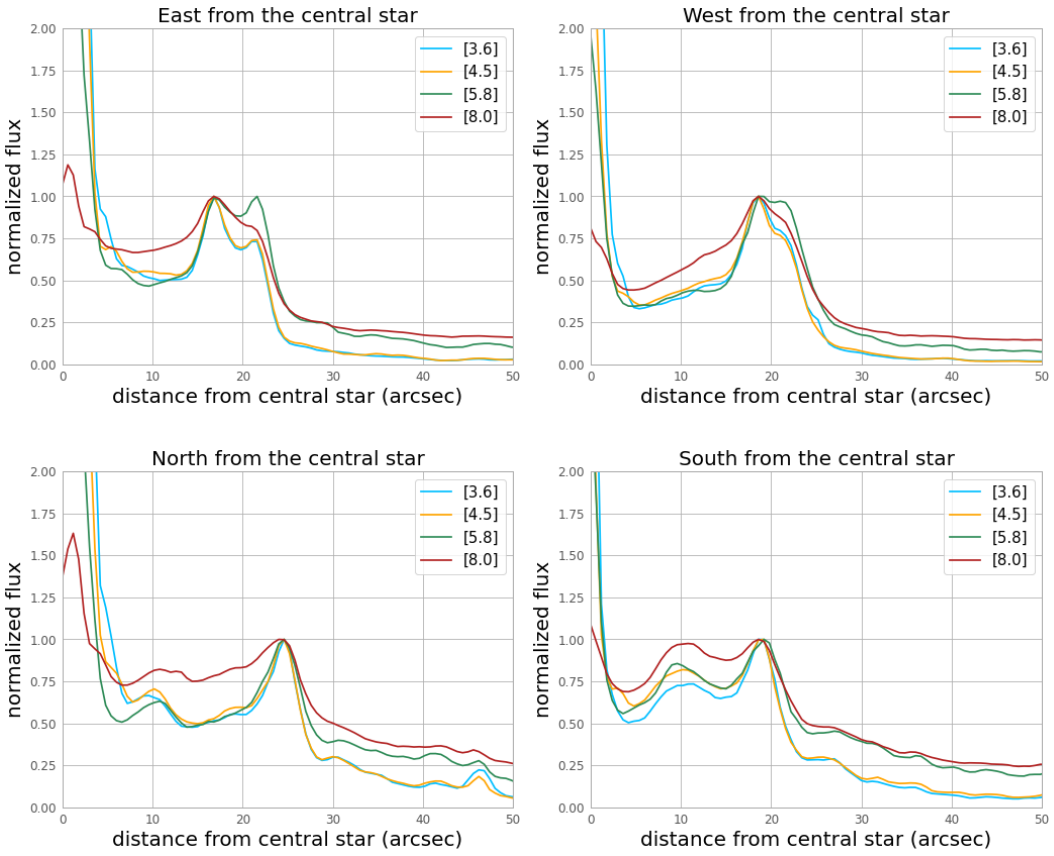

Figure 4.30: Radial analysis for Spitzer channels East, West, North, and South from the central star.

radial profile peaks East from the central star of the planetary nebula (West, North and South results are in tables B′.8, B′.9, B′.10 respectively). Comparing these results with the corresponding results from JWST, we found that all Spitzer channels peak at smaller distances than JWST but within the random errors.

Channel	Band's Center (μm)	1st peak (arcsec)	2nd peak (arcsec)
1	3.6	16.8	21.0
2	4.5	16.8	21.6
3	5.8	16.8	21.6
4	8.0	16.8	-

Table 4.7: Radial analysis from each SPITZER channel Left from the PNe.

Furthermore, IRAC's channels contain molecular Hydrogen lines from ground rotational state 0-0 and some forbidden emission lines

(Figure 3.12). More specifically, channel 2 contains Br-α and various 0–0 H_2 emissions in the range 4.649-4.694 μm (Phillips et al., 2010), channel 3 contains S(7) (5.5μm) and S(6) (6.1μm) while channel 4 contains S(4) (8.0μm), S(5) (6.9μm) and [Ar III] 8.991 μm lines (Akras et al., 2020). All "S" transitions are from the upper to lower J state with ΔJ=2.

Especially, Phillips et al. (2010) focused on some channels ratios like [3.6]/[4.5], [5.8]/[4.5] and [8.0]/[4.5]. He proposed that [8.0]/[4.5] and [5.8]/[4.5] ratios increase at large distances and that [8.0]/[4.5] show dips at low ionization regions outside the nebular core. So, we created our own radial profiles for IRAC's channels ratios, which are illustrated in Figure 4.31.

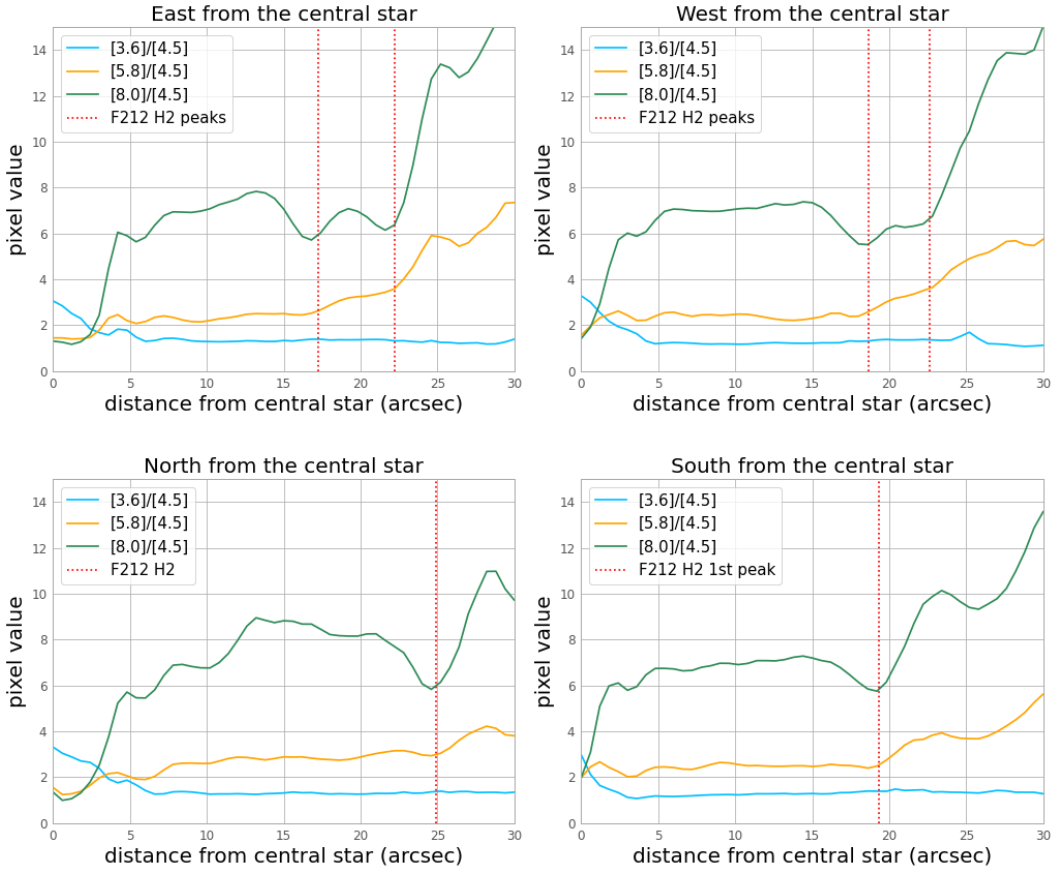

Figure 4.31: Radial profile for Spitzer channels ratios East, West, North, and South from the central star.

From Figure 4.31 it's clear that in all four directions, [8.0]/[4.5] and [5.8]/[4.5] increase with the distance from the central star. In addition, dips in the [8.0]/[4.5] profile are present at distances which correspond to

the rim of the nebular shell and strong molecular Hydrogen emission.

These are great results which verify the suggestions of several authors that [8.0]/[4.5] ratio provides indirect evidence for the presence of H_2 gas. Here, we provide for the first time direct confirmation between the link of H_2 emission lines from JWST and infrared colors from Spitzer's IRAC.

Chapter 5

Conclusions

1. Summary

In this thesis we presented a detailed analysis of the physicochemical parameters of the NGC 3132 planetary nebula as calculated from MUSE, JWST, HST and SST. In addition, we tested the goodness of fit of a 3D photoionization model. A brief summary of this study includes:

1. Emission line maps were extracted from MUSE datacube by fitting a Gaussian profile and subtracting the continuum.
2. Morphological structure of PN NGC 3132 was identified (central star, companion star, central ionized cavity, rim, belt-like structure, dust shells).
3. Through SATELLITE code, it was verified that neither the angle nor the location of the slit affects significant the values of the physicochemical parameters.
4. The ionization structure was studied from radial profiles of emission lines.
5. 2D maps for T_e and N_e were created from several line ratios in order to examine in more detail the characteristics of the nebula. The rims have high electron temperature $\sim 10,000\,K$ and electron density $\sim$ 1000 cm^{-3}, while inside the elliptical ionized cavity $T_e \sim 9,700\,K$ and $N_e \sim 400\ cm^{-3}$.

6. Several maps of ionic and total abundances were created and as expected ions with higher ionization degree inhabit the main ionized cavity while ions with lower ionization degree exist around the rims.

7. ICFs were calculated by two different methods (KB Kingsburgh and Barlow (1994) and DIMS Delgado-Inglada et al. (2014)) and mapped.

8. Various diagnostic diagrams were developed from MUSE data in order to examine how PN NGC 3132 compares with the typical PNe population, and indeed it falls into the predicted statistical limits for a photoionisation dominated PN.

9. Radial profiles of strong optical emission lines were compared between MUSE and HST and it was found that MUSE data peak at slightly larger distances than HST's ones.

10. Through SST and mostly JWST data the rich molecular halo was detected in infrared wavelengths and the exact distances from the central star that H_2 emissions are present were measured.

11. IRAC's bands ratio [8.0]/[4.5] dip at the rim of the nebula, exactly where H_2 emission from JWST peaks.

12. A close relation was observed between dust extinction as derived by Hα and Hβ recombination lines and molecular Hydrogen. This kind of dust may prevent the H_2 gas from being dissociated.

13. A 3D photoionization model was put to the test and compared with MUSE data. The model in general represent good enough the nebula, however it underestimates the electron density by a little and overestimates the electron temperature. Moreover, the model is really close to real data as far as ionic and total abundances are concerned.

2. Future Work

In the future, we plan to take into consideration the differences between the model and real data and adjust its parameters in order to make it even better. In this way, we will be able to understand in depth the morphology and ionization structure of NGC 3132 and PNe in general. Furthermore, we would like to apply the same codes and analysis to different kind of Planetary Nebula, so we can examine them

extensively and check if indeed there is a close relation between dust extinction and molecular Hydrogen. Another future goal of ours is to improve the SATELLITE code (e.g. T_e and N_e from more line ratios) and even extend it to be able to analyze IR IFU data. Finally, we would like to use SATELLITE and the other python codes used in this thesis for different astronomical objects like HII regions, SNRs, Galaxies and even at Active Galactic Nucleus (AGN) observed by IFU instruments.

Bibliography

Akras, S., Boumis, P., Meaburn, J., Alikakos, J., López, J. A., and Gonçalves, D. R. (2015). Evidence for a [WR] or WEL-type binary nucleus in the bipolar planetary nebula Vy 1-2. , 452(3):2911–2929.

Akras, S., Clyne, N., Boumis, P., Monteiro, H., Gonçalves, D. R., Redman, M. P., and Williams, S. (2016). Deciphering the bipolar planetary nebula Abell 14 with 3D ionization and morphological studies. *Monthly Notices of the Royal Astronomical Society*, 457(4):3409–3419.

Akras, S., Gonç alves, D. R., Ramos-Larios, G., and Aleman, I. (2020). H2 emission in the low-ionization structures of the planetary nebulae NGC 7009 and NGC 6543. *Monthly Notices of the Royal Astronomical Society*, 493(3):3800–3810.

Akras, S., Gonçalves, D. R., and Ramos-Larios, G. (2017). H_2 in low-ionization structures of planetary nebulae. , 465(2):1289–1296.

Akras, S., Gonçalves, D. R., Ramos-Larios, G., and Aleman, I. (2020). Molecular Hydrogen Microstructures in Planetary Nebulae. *Galaxies*, 8(2):30.

Akras, S., López, J.-A., and Steffen, W. (2012). 3-D modeling of the collimated outflows of M1-32 and M2-42. *IAU Symposium*, 283:302–303.

Akras, S. and López, J. A. (2012). Three-dimensional modelling of the collimated bipolar outflows of compact planetary nebulae with Wolf–Rayet-type central stars. *Monthly Notices of the Royal Astronomical Society*, 425(3):2197–2202.

Akras, S., Monteiro, H., Aleman, I., Farias, M. A. F., May, D., and Pereira, C. B. (2020). Exploring the differences of integrated and spatially resolved analysis using integral field unit data: the case of Abell 14. *Monthly Notices of the Royal Astronomical Society*, 493(2):2238–2252.

Akras, S., Monteiro, H., Walsh, J., Isabel, A., Gonçalves, D. R., and Boumis, P. (2022a). SATELLITE: Application to Planetary Nebulae IFU Data. *Galaxies*, 10(1):27.

Akras, S., Monteiro, H., Walsh, J. R., García-Rojas, J., Aleman, I., Boffin, H., Boumis, P., Chiotellis, A., Corradi, R. M. L., Gonçalves, D. R., Gutiérrez-Soto, L. A., Jones, D., Morisset, C., and Papanikolaou, X. (2022b). Spectroscopic analysis tool for intEgraL fieLd unIt daTacubEs (SATELLITE): case studies of NGC 7009 and NGC 6778 with MUSE. , 512(2):2202–2221.

Aleman, I. and Gruenwald, R. (2011). H_2 infrared line emission from the ionized region of planetary nebulae. , 528:A74.

Ali, A., Dopita, M. A., Basurah, H. M., Amer, M. A., Alsulami, R., and Alruhaili, A. (2016). IFU spectroscopy of southern planetary nebulae - III. , 462(2):1393–1404.

Bacon, R., Vernet, J., Borisova, E., Bouché, N., Brinchmann, J., Carollo, M., Carton, D., Caruana, J., Cerda, S., Contini, T., Franx, M., Girard, M., Guerou, A., Haddad, N., Hau, G., Herenz, C., Herrera, J. C., Husemann, B., Husser, T. O., Jarno, A., Kamann, S., Krajnovic, D., Lilly, S., Mainieri, V., Martinsson, T., Palsa, R., Patricio, V., Pécontal, A., Pello, R., Piqueras, L., Richard, J., Sandin, C., Schroetter, I., Selman, F., Shirazi, M., Smette, A., Soto, K., Streicher, O., Urrutia, T., Weilbacher, P., Wisotzki, L., and Zins, G. (2014). MUSE Commissioning. *The Messenger*, 157:13–16.

Baessgen, M., Diesch, C., and Grewing, M. (1990). A three-dimensional ionisation model of the planetary nebula NGC 3132. , 237:201.

Bailer-Jones, C. A. L., Rybizki, J., Fouesneau, M., Demleitner, M., and Andrae, R. (2021). Estimating distances from parallaxes. v. geometric and photogeometric distances to 1.47 billion stars in gaia early data release 3. *The Astronomical Journal*, 161(3):147.

Balick, B. (1987). The Evolution of Planetary Nebulae. I. Structures, Ionizations, and Morphological Sequences. , 94:671.

Chornay, N. and Walton, N. A. (2021). One star, two star, red star, blue star: an updated planetary nebula central star distance catalogue from igaia/i EDR3. *Astronomy &amp Astrophysics*, 656:A110.

Ciardullo, R., Bond, H. E., Sipior, M. S., Fullton, L. K., Zhang, C. Y., and Schaefer, K. G. (1999). A HUBBLE SPACE TELESCOPE Survey for Resolved Companions of Planetary Nebula Nuclei. , 118(1):488–508.

De Marco, O., Akashi, M., Akras, S., Alcolea, J., Aleman, I., Amram, P., Balick, B., De Beck, E., Blackman, E. G., Boffin, H. M. J., Boumis, P., Bublitz, J., Bucciarelli, B., Bujarrabal, V., Cami, J., Chornay, N., Chu, Y.-H., Corradi, R. L. M., Frank, A., García-Hernández, D. A., García-Rojas, J., García-Segura, G., Gómez-Llanos, V., Gonçalves, D. R., Guerrero, M. A., Jones, D., Karakas, A. I., Kastner, J. H., Kwok, S., Lykou, F., Manchado, A., Matsuura, M., McDonald, I., Miszalski, B., Mohamed, S. S., Monreal-Ibero, A., Monteiro, H., Montez, R., Baez, P. M., Morisset, C., Nordhaus, J., Mendes de Oliveira, C., Osborn, Z., Otsuka, M., Parker, Q. A., Peeters, E., Quint, B. C., Quintana-Lacaci, G., Redman, M., Ruiter, A. J., Sabin, L., Sahai, R., Contreras, C. S., Santander-García, M., Seitenzahl, I., Soker, N., Speck, A. K., Stanghellini, L., Steffen, W., Toalá, J. A., Ueta, T., Van de Steene, G., Van Winckel, H., Ventura, P., Villaver, E., Vlemmings, W., Walsh, J. R., Wesson, R., and Zijlstra, A. A. (2022). The messy death of a multiple star system and the resulting planetary nebula as observed by JWST. *Nature Astronomy*, 6:1421–1432.

Delgado-Inglada, G., Morisset, C., and Stasińska, G. (2014). Ionization correction factors for planetary nebulae - I. Using optical spectra. , 440(1):536–554.

Donald E. Osterbrock, G. J. (2006). *Astrophysics of Gaseous Nebula and Active Galactic Nuclei*. University Science Books.

Fang, X., Zhang, Y., Kwok, S., Hsia, C.-H., Chau, W., Ramos-Larios, G., and Guerrero, M. A. (2018). Extended structures of planetary nebulae detected in hsub2/sub emission. *The Astrophysical Journal*, 859(2):92.

Frank, A., Chen, Z., Reichardt, T., Marco, O. D., Blackman, E., and Nordhaus, J. (2018). Planetary nebulae shaped by common envelope evolution.

Gaia Collaboration (2020). VizieR Online Data Catalog: Gaia EDR3 (Gaia Collaboration, 2020). *VizieR Online Data Catalog*, page I/350.

García-Rojas, J., Morisset, C., Jones, D., Wesson, R., Boffin, H. M. J., Monteiro, H., Corradi, R. L. M., and Rodríguez-Gil, P. (2022a). MUSE spectroscopy of planetary nebulae with high abundance discrepancies. , 510(4):5444–5463.

García-Rojas, J., Morisset, C., Jones, D., Wesson, R., Boffin, H. M. J., Monteiro, H., Corradi, R. L. M., and Rodríguez-Gil, P. (2022b). MUSE spectroscopy of planetary nebulae with high abundance discrepancies. , 510(4):5444–5463.

García-Segura, G., Ricker, P. M., and Taam, R. E. (2018). Common Envelope Shaping of Planetary Nebulae. , 860(1):19.

Gómez-Gordillo, S., Akras, S., Gonçalves, D. R., and Steffen, W. (2020). Distance mapping applied to four well-known planetary nebulae and a nova shell. *Monthly Notices of the Royal Astronomical Society*, 492(3):4097–4111.

Hannu Karttunen, Pekka Kröger, H. O. M. P. K. J. D. (2017). *Fundamental Astronomy*. Springer Heidelberg New York Dordrecht London.

Howarth, I. D. (1983). LMC and galactic extinction. , 203:301–304.

Icke, V. (1988). Blowing bubbles. , 202:177–188.

Keeton, C. (2014). *Principles of Astrophysics: Using Gravity and Stellar Physics to Explore the Cosmos*. Springer Science+Business Media New York 2014.

Kingsburgh, R. L. and Barlow, M. J. (1994). Elemental abundances for a sample of southern galactic planetary nebulae. , 271:257–299.

Kohoutek, L. and Laustsen, S. (1977). Central star of NGC 3132: a visual binary. , 61:761–763.

Kwok, S. Purton, C. R. F. P. M. (1978). On the origin of planetary nebulae. , 219:L125–L127.

Kwok, S. (2000). *The Origin and Evolution of Planetary Nebulae*. Cambridge University Press.

Livio, M. and Soker, N. (1988). The Common Envelope Phase in the Evolution of Binary Stars. , 329:764.

Mata, H., Ramos-Larios, G., Guerrero, M. A., Nigoche-Netro, A., Toalá, J. A., Fang, X., Rubio, G., Kemp, S. N., Navarro, S. G., and Corral, L. J. (2016). Spitzer mid-infrared spectroscopic observations of planetary nebulae. , 459(1):841–853.

Méndez, R. H. (1978). A-type central stars of planetary nebulae - II. The central stars of NGC 2346, He 2-36 and NGC 3132. , 185:647–660.

Mendez, R. H., Niemela, V. S., and Lee, P. (1978). A-type central stars of planetary nebulae - I. A radial-velocity study of the central stars of NGC 2346 and NGC 3132. , 184:351–354.

Monreal-Ibero, A. and Walsh, J. R. (2020). The MUSE view of the planetary nebula NGC 3132. *Astronomy &amp Astrophysics*, 634:A47.

Monteiro, H., Morisset, C., Gruenwald, R., and Viegas, S. M. (2000). Morphology and Kinematics of Planetary Nebulae. II. A Diabolo Model for NGC 3132. , 537(2):853–860.

Phillips, J. P., Cuesta, L. C., and Ramos-Larios, G. (2010). Mapping and spectroscopy of the planetary nebula NGC 7009 in the visual and infrared. , 409(3):881–902.

Pontoppidan, K. M., Barrientes, J., Blome, C., Braun, H., Brown, M., Carruthers, M., Coe, D., DePasquale, J., Espinoza, N., Marin, M. G., Gordon, K. D., Henry, A., Hustak, L., James, A., Jenkins, A., Koekemoer, A. M., LaMassa, S., Law, D., Lockwood, A., Moro-Martin, A., Mullally, S. E., Pagan, A., Player, D., Proffitt, C., Pulliam, C., Ramsay, L., Ravindranath, S., Reid, N., Robberto, M., Sabbi, E., Ubeda, L., Balogh, M., Flanagan, K., Gardner, J., Hasan, H., Meinke, B., and Nota, A. (2022). The JWST early release observations. *The Astrophysical Journal Letters*, 936(1):L14.

Riesgo, H. and López, J. A. (2006). Revised Diagnostic Diagrams for Planetary Nebulae. , 42:47–51.

Rousseau-Nepton, L., Robert, C., Martin, R. P., Drissen, L., and Martin, T. (2018). NGC628 with SITELLE: I. Imaging spectroscopy of 4285 H II region candidates. , 477(3):4152–4186.

Sahai, R., Bujarrabal, V., Quintana-Lacaci, G., Reindl, N., de Steene, G. V., Contreras, C. S., and Ressler, M. E. (2023). The binary and the disk: The beauty is found within NGC3132 with JWST. *The Astrophysical Journal*, 943(2):110.

Sahai, R., Wootten, A., and Clegg, R. E. S. (1990). CO in the bipolar planetary nebula NGC 3132. , 234:L1.

Steffen, W., Koning, N., Wenger, S., Morisset, C., and Magnor, M. (2011). Shape: A 3D Modeling Tool for Astrophysics. *IEEE Transactions on Visualization and Computer Graphics*, 17(4):454–465.

Tsamis, Y. G., Barlow, M. J., Liu, X.-W., Storey, P. J., and Danziger, I. J. (2004). A deep survey of heavy element lines in planetary nebulae - II. recombination-line abundances and evidence for cold plasma. *Monthly Notices of the Royal Astronomical Society*, 353(3):953–979.

Zuckerman, B. and Gatley, I. (1988). Molecular Hydrogen Maps of Extended Planetary Nebulae: The Dumbell, the Ring, and NGC 2346. , 324:501.

Appendix A′

Complementary Theory

1. Evolutionary Time scales

There are three main time scales regarding the evolution of a star.

1. Nuclear time scale t_n

   This is the time it takes for a star to radiate all of its energy that has been produced by nuclear reactions.

$$t_n \approx \frac{0.007 \times 0.1\, M\, c^2}{L} \tag{A′.1}$$

$$t_n \approx \frac{M/M_\odot}{L/L_\odot} \times 10^{10}\, years \tag{A′.2}$$

2. Thermal time scale t_t

   This is the time it takes a star to radiate away all of its thermal energy if nuclear energy isn't taken into account. It's equal to the time it takes for the radiation to reach the surface, starting from the core.

$$t_t \approx \frac{0.5\ G\ M^2}{R\ L} \tag{A′.3}$$

$$t_t \approx \frac{(M/M_\odot)^2}{(R/R_\odot)\ (L/L_\odot)} \times 2 \times 10^7\ years \tag{A′.4}$$

3. Dynamical time scale t_d

   This is the time it takes a star to collapse by gravitational force if the pressure that resists gravity disappears. It is estimated by the time it takes a particle to fall freely to the core, starting from the surface of the star.

$$t_d = \frac{2\pi}{2}\sqrt{\frac{(R/2)^3}{G\ M}} \approx \sqrt{\frac{R^3}{G\ M}} \tag{A'.5}$$

   If we compare all the time scales for a star like our Sun, we get:

$$t_d \ll t_d \ll t_n$$

2. CNO Cycle

At high mass stars the force of gravity is so strong that it compresses the H in the core, reaching really high temperatures compared to the low mass stars. So, during Main Sequence the H is burning into He through CNO (Carbon Nitrogen Oxygen) cycle and the released energy is proportional to T^{17} while the proton-proton reaction is proportional to T^4. Through CNO cycle, H is transforming to He at a higher rate than it does in proton-proton reaction. This is the reason why high mass stars spend less time in Main Sequence than low mass stars.

$$\begin{aligned}
{}^{12}_{6}\mathrm{C} + {}^{1}_{1}\mathrm{H} &\longrightarrow {}^{13}_{7}\mathrm{N} + \gamma \\
{}^{13}_{7}\mathrm{N} &\longrightarrow {}^{13}_{6}\mathrm{C} + e^{+} + \nu_e \\
{}^{13}_{6}\mathrm{C} + {}^{1}_{1}\mathrm{H} &\longrightarrow {}^{14}_{7}\mathrm{N} + \gamma \\
{}^{14}_{7}\mathrm{N} + {}^{1}_{1}\mathrm{H} &\longrightarrow {}^{15}_{8}\mathrm{O} + \gamma \\
{}^{15}_{8}\mathrm{O} &\longrightarrow {}^{15}_{7}\mathrm{N} + e^{+} + \nu_e \\
{}^{15}_{7}\mathrm{N} + {}^{1}_{1}\mathrm{H} &\longrightarrow {}^{12}_{6}\mathrm{C} + {}^{4}_{2}\mathrm{He}
\end{aligned}$$

High mass stars also go through H burning, H shell burning, He burning and He shell burning. The fact that differentiates them from low mass stars is that they don't stop at He shell burning. Due to their

higher mass, they also have higher temperatures and densities in their cores, which enables them to burn even heavier elements. After C and O burning, the temperature is high enough to create Ne and at even higher temperatures Na, Mg, Si, P, S, Ar is produced until Fe is formed. These nuclear reactions are known as Silicon Burning and occur when the star is located in the AGB phase (Red Supergiant).

3. Fe Burning

When Fe is formed in a star's core, an exothermic reaction has to take place (fusion or fission) so the released energy can resist inwards gravity. Elements lighter than Fe through nuclear fusion create heavier elements, while the reactants are lighter than Fe. However, for heavier elements than Fe through fission, they create lighter elements, while the reactants are heavier than Fe.

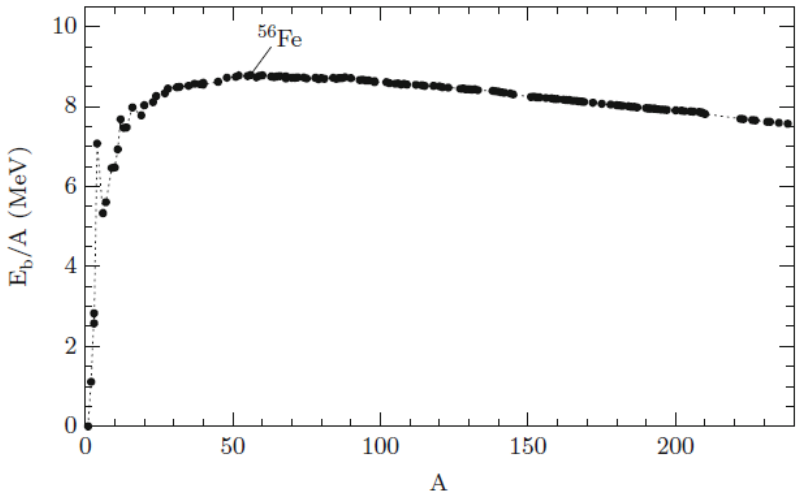

Figure A′.1: Binding energy per nucleon, as a function of the atomic mass number.

Fe as the most stable element, has to consume energy (endothermic reaction) to change its molecular structure. This isn't possible inside a star's core, that's why all the nuclear fusion reactions stop at when Fe is forming.

In this way, the star is starting to lose energy due to various mechanisms.

1. Fission of Fe to He.
2. Reverse β-reaction, creating neutrinos and neutrons from protons and free electrons.
3. Neutrinos escaping, transferring huge amounts of energy.

In the end, gravity overcomes the pressure until the star collapses into a Supernova explosion.

The huge energy released from the Supernova explosion is able to transform Fe into heavier elements like Uranium. So, the Supernova explosion is the main mechanism which creates heavier elements than Fe in the Universe.

4. Intercombination and forbidden energy transitions

The selection rules for Spin-Orbit interactions for energy transitions are the following. $\Delta L = \pm 1, 0$, $\Delta S = 0$, $\Delta J = 0, \pm 1$ except $J = 0 \rightarrow 0$.

A system with two $s = 1/2$ particles are in a triplet (parallel spin $m_s = -1, 0, 1$) or a singlet (antiparallel spin $m_s = 0$) state.

In the case of He, which Spin-Orbit fully applies, the transitions that occur are the singlet-singlet or triplet-triplet. The singlet or triplet states can be considered as different atoms, e.g. para-helium or ortho-helium respectively for He.

The transitions from singlet to triplet states of light ions like CIII, OIII, NIV are called intercombination transitions because the Spin-Orbit selection rules don't apply fully in ions. These transitions are symbolized with one right bracket, e.g. C III].

Transitions which violate Spin-Orbit selection rules can occur as electric quadrupole transitions or magnetic dipole transitions, but their spontaneous emission coefficients (A_{ij} Einstein coefficient) are really smaller than the permitted electric dipole ones. In Earth-like conditions, this means that the high frequency of the collisions don't allow the higher energy state to get de-excited spontaneously. However, in nebular conditions the time between collisions is higher than the energy state's lifetime, so

they get de-excited spontaneously emitting a forbidden photon. Most of the emission lines in a Planetary Nebula spectrum are forbidden and they are symbolized with two brackets (e.g. [N II]).

At last, energy transitions between two energy states with the same multiplets are known as fine structure lines.

5. Two Photon Decay

The $^2S_{1/2}$ Hydrogen energy state is metastable and the transition to the ground state 1^2S is forbidden since $\Delta l = 0$ and $\Delta m = 0$. The energy transitions to the $2^2P_{1/2}$ has very small transition probability and occurs once in 30 million years.

The only way for the electron to escape from the $2s$ state is with photoionisation or with a collision to $2^2P_{1/2}$ state where it gets quickly de-excited emitting a Lyman-α photon.

In a low density environment, like in a Planetary Nebula, an electron at $^2S_{1/2}$ Hydrogen state "jumps" to another "virtual" p state where it's located between $n = 1$ and $n = 2$ energy states. Later, this electron gets de-excited to the ground level, emitting two photons with frequencies $\nu_1 + \nu_2 = \nu_{Ly-\alpha}$. This procedure contributes to continuum emission at near UV wavelengths.

6. Critical Density

Critical density is the density at which the rate of collisional de-excitation equals the rate of radiation de-excitation. If the density is higher than the critical one, the collisional de-excitation becomes important and the forbidden lines more wick.

Appendix B′

Radial Analysis results for different orientations and Abundance tables

Radial profiles for JWST, MUSE, HST and SST available data as well as c(Hβ)-H_2 comparison East, West, North, and South from the central star. In addition, there are tables that include statistical parameters for ionic abundances.

Emission line	1st peak (arcsec)	2nd peak (arcsec)
[O III] 5007Å	16.0	-
Hα 6563Å	16.6	-
Hβ 4861Å	16.6	-
[S III] (F1800W)	16.75	-
[S III] 9069Å	16.8	-
Pa-α (F187N)	16.84	22.00
[S III] (F090W)	16.94	22.00
Br-a (F405N)	16.95	22.10
H_2 (F212N)	17.26	22.23
[Ne II] (F1280W)	17.30	22.40
[N II] 5755Å	17.4	21.6
[N II] 6584Å	17.4	21.6
H_2 (F356W)	17.45	22.18
H_2 (F470N)	17.51	22.24
PAH (F1130W)	17.52	22.29
H_2 (F770W)	17.52	22.73
[S II] 6731Å	17.6	21.8
[N I] 5199Å	17.8	22.4
[O I] 6300Å	17.8	22.4

Table B′.1: Radial analysis for all emission from MUSE and JWST lines East from the PNe.

Emission line	1st peak (arcsec)	2nd peak (arcsec)
[O III] 5007Å	18.8	-
Pa-α (F187N)	19.21	-
Br-a (F405N)	19.28	-
[S III] (F1800W)	19.30	-
[S III] (F090W)	19.32	-
H_2 (F356W)	19.34	20.16
H_2 (F212N)	19.35	20.19
[S III] 9069Å	19.4	-
Hα 6563Å	19.4	-
Hβ 4861Å	19.4	-
H_2 (F470N)	19.40	20.16
[Ne II] (F1280W)	19.52	20.29
H_2 (F770W)	19.52	20.63
[N II] 6584Å	19.8	-
[N II] 5755Å	20.0	-
[S II] 6731Å	20.2	-
[O I] 6300Å	20.4	-
[N I] 5199Å	20.6	-
PAH (F1130W)	20.74	-

Table B′.2: Radial analysis for all emission lines from MUSE and JWST South from the PNe.

Emission line	1st peak (arcsec)	2nd peak (arcsec)
[O III] 5007Å	17.6	-
[S III] 9069Å	17.6	-
[S III] (F090W)	17.84	21.0
Pa-α (F187N)	17.92	21.0
[S III] (F1800W)	17.97	-
Hα 6563Å	18.0	-
Br-a (F405N)	18.08	21.04
Hβ 4861Å	18.2	-
[N II] 5755Å	18.4	20.6
[N II] 6584Å	18.4	20.6
[S II] 6731Å	18.4	20.8
H_2 (F470N)	18.58	21.04
[O I] 6300Å	18.6	21.0
H_2 (F356W)	18.65	21.10
H_2 (F212N)	18.68	21.08
[N I] 5199Å	18.8	21.0
H_2 (F770W)	18.96	-
[Ne II] (F1280W)	18.96	-
PAH (F1130W)	19.0	-

Table B′.3: Radial analysis for all emission lines from MUSE and JWST West from the PNe.

Emission line	1st peak (arcsec)	2nd peak (arcsec)
[O III] 5007Å	18.4	-
Hβ 4861Å	18.4	23.8
[S III] 9069Å	18.6	23.8
Hα 6563Å	18.4	24.0
[N II] 6584Å	-	24.0
[N II] 5755Å	-	24.0
[S III] (F1800W)	-	24.07
Br-a (F405N)	18.58	24.13
Pa-α (F187N)	18.60	24.19
[S III] (F090W)	18.52	24.22
H_2 (F470N)	-	24.32
H_2 (F356W)	-	24.32
PAH (F1130W)	-	24.4
H_2 (F770W)	-	24.4
[Ne II] (F1280W)	-	24.4
[S II] 6731Å	-	24.4
H_2 (F212N)	-	24.42
[O I] 6300Å	-	24.6
[N I] 5199Å	-	24.6

Table B′.4: Radial analysis for all emission lines from MUSE and JWST North from the PNe.

Emission line	1st peak (arcsec)	2nd peak (arcsec)
[O III] (F502N)	17.4	20.9
Hα (F656N)	18.1	20.9
[N II] (F658N)	18.5	20.8
[O I] (F631N)	18.6	20.8
[S II] (F673N)	18.7	20.8

Table B′.5: Radial analysis for emission lines West from the PNe as captured by HST.

Emission line	1st peak (arcsec)	2nd peak (arcsec)
[O III] (F502N)	18.0	-
Hα (F656N)	24.0	-
[N II] (F658N)	24.1	-
[O I] (F631N)	24.1	-
[S II] (F673N)	24.2	-

Table B′.6: Radial analysis for emission lines North from the PNe as captured by HST.

Emission line	1st peak (arcsec)	2nd peak (arcsec)
[O III] (F502N)	18.6	-
Hα (F656N)	18.9	-
[S II] (F673N)	19.7	-
[N II] (F658N)	19.8	-
[O I] (F631N)	19.9	-

Table B′.7: Radial analysis for emission lines South from the PNe as captured by HST.

Channel	Band's Center (μm)	1st peak (arcsec)	2nd peak (arcsec)
1	3.6	18.6	-
4	8.0	18.6	-
2	4.5	19.2	-
3	5.8	19.2	-

Table B′.8: Radial analysis from each SPITZER channel South from the PNe.

Channel	Band's Center (μm)	1st peak (arcsec)	2nd peak (arcsec)
1	3.6	18.6	-
2	4.5	18.6	-
3	5.8	18.6	21.0
4	8.0	18.6	-

Table B′.9: Radial analysis from each SPITZER channel West from the PNe.

Channel	Band's Center (μm)	1st peak (arcsec)	2nd peak (arcsec)
4	8.0	-	24.0
1	3.6	-	24.6
2	4.5	-	24.6
3	5.8	-	24.6

Table B′.10: Radial analysis from each SPITZER channel North from the PNe.

Emission line	1st peak (arcsec)	2nd peak (arcsec)
H_2 (F356W)	19.34	20.10
H_2 (F212N)	19.35	20.19
c(Hβ)	19.4	20.2
H_2 (F470N)	19.40	20.16
H_2 (F770W)	19.52	20.63

Table B′.11: Radial analysis comparison between c(Hβ) and molecular Hydrogen South from the PNe.

Emission line	1st peak (arcsec)	2nd peak (arcsec)
c(Hβ)	17.0	22.4
H_2 (F470N)	18.58	22.49
H_2 (F356W)	18.65	22.55
H_2 (F212N)	18.68	22.60
H_2 (F770W)	18.96	21.85

Table B′.12: Radial analysis comparison between c(Hβ) and molecular Hydrogen West from the PNe.

Emission line	1st peak (arcsec)	2nd peak (arcsec)
H_2 (F770W)	-	24.40
H_2 (F356W)	-	24.88
H_2 (F212N)	-	24.88
H_2 (F470N)	-	24.88
c(Hβ)	-	25.0

Table B′.13: Radial analysis comparison between c(Hβ) and molecular Hydrogen North from the PNe.

Name Parameter	No. spaxels	5% Value	Q1 Value	Median Value	Q3 Value	95% Value	Mean Value	Sigma
He I 5876Å	76596	9.18e-02	1.14e-01	1.24e-01	1.36e-01	1.65e-01	1.26e-01	2.16e-02
He I 6678Å	71111	8.85e-02	1.09e-01	1.19e-01	1.31e-01	1.60e-01	1.21e-01	2.16e-02
He II 5412Å	10962	5.69e-03	1.14e-02	1.91e-02	2.93e-02	3.85e-02	2.05e-02	1.06e-02
[O I] 6300Å	77419	9.11e-06	2.72e-05	9.67e-05	1.64e-04	2.81e-04	1.09e-04	8.96e-05
[O I] 6363Å	77419	9.49e-06	2.83e-05	1.01e-04	1.70e-04	2.92e-04	1.13e-04	9.31e-05
[O II] 7320Å	77012	8.59e-05	1.43e-04	2.88e-04	3.73e-04	4.90e-04	2.76e-04	1.37e-04
[O II] 7330Å	77012	8.59e-05	1.42e-04	2.82e-04	3.64e-04	4.76e-04	2.70e-04	1.33e-04
[O III] 4959Å	32518	2.09e-04	2.95e-04	3.95e-04	4.65e-04	5.33e-04	3.82e-04	1.04e-04
[O III] 5007Å	32518	2.09e-04	2.95e-04	3.96e-04	4.66e-04	5.33e-04	3.82e-04	1.04e-04
[N I] 5199Å	64979	4.34e-06	9.58e-06	2.66e-05	4.08e-05	6.59e-05	2.83e-05	2.03e-05
[N II] 5755Å	77538	3.79e-05	7.33e-05	1.74e-04	2.19e-04	2.70e-04	1.56e-04	7.87e-05
[N II] 6548Å	77538	3.74e-05	7.23e-05	1.72e-04	2.16e-04	2.66e-04	1.54e-04	7.76e-05
[N II] 6583Å	77538	3.81e-05	7.36e-05	1.75e-04	2.20e-04	2.71e-04	1.57e-04	7.90e-05
[S II] 6716Å	77538	1.04e-06	1.88e-06	4.13e-06	5.38e-06	7.04e-06	3.88e-06	2.00e-06
[S II] 6731Å	77538	1.04e-06	1.88e-06	4.13e-06	5.38e-06	7.04e-06	3.88e-06	2.00e-06
[S III] 6312Å	32518	4.76e-06	5.80e-06	6.75e-06	7.64e-06	8.98e-06	6.77e-06	1.28e-06
[S III] 9069Å	32518	4.76e-06	5.80e-06	6.75e-06	7.64e-06	8.98e-06	6.77e-06	1.28e-06
[Cl III] 5517Å	32518	1.05e-07	1.30e-07	1.49e-07	1.66e-07	1.90e-07	1.48e-07	2.62e-08
[Cl III] 5538Å	32518	1.05e-07	1.30e-07	1.49e-07	1.66e-07	1.90e-07	1.48e-07	2.62e-08
[Ar III] 7136Å	32518	1.88e-06	2.42e-06	2.68e-06	2.87e-06	3.08e-06	2.61e-06	3.61e-07

Table B′.14: Statistics for abundances relative to H^+ from MUSE data.

Name Parameter	No. spaxels	5% Value	Q1 Value	Median Value	Q3 Value	95% Value	Mean Value	Sigma
He I 5876Å	3438	7.59e-02	1.19e-01	1.27e-01	1.79e-01	2.88e-01	1.51e-01	6.28e-02
He I 6678Å	3438	7.55e-02	1.18e-01	1.26e-01	1.79e-01	2.86e-01	1.51e-01	6.24e-02
He II 5412Å	1431	1.07e-05	1.82e-04	7.14e-03	3.54e-02	4.60e-02	1.66e-02	1.81e-02
[O I] 6300Å	3438	9.07e-06	1.79e-05	7.07e-05	4.75e-04	2.35e-03	4.54e-04	8.37e-04
[O II] 7320Å	3438	2.05e-05	3.49e-05	8.81e-05	1.08e-04	1.18e-04	7.49e-05	3.63e-05
[O II] 7330Å	3438	7.92e-05	1.35e-04	3.37e-04	4.17e-04	4.57e-04	2.88e-04	1.40e-04
[O III] 4363Å	4131	2.94e-07	2.37e-06	8.43e-05	4.59e-04	5.58e-04	2.14e-04	2.37e-04
[O III] 4959Å	4354	2.66e-07	2.13e-06	4.84e-05	3.46e-04	4.38e-04	1.59e-04	1.82e-04
[O III] 5007Å	4360	2.58e-07	2.10e-06	4.78e-05	3.44e-04	4.36e-04	1.58e-04	1.81e-04
[N I] 5199Å	3438	1.60e-07	3.58e-07	1.49e-06	1.09e-05	7.30e-05	1.27e-05	2.50e-05
[N II] 5755Å	3438	3.18e-05	5.44e-05	1.67e-04	3.26e-04	3.94e-04	1.90e-04	1.34e-04
[N II] 6548Å	3438	3.09e-05	5.29e-05	1.63e-04	3.17e-04	3.83e-04	1.84e-04	1.31e-04
[N II] 6583Å	3438	3.21e-05	5.49e-05	1.69e-04	3.29e-04	3.97e-04	1.91e-04	1.36e-04
[S II] 6716Å	3438	6.19e-07	1.11e-06	3.59e-06	1.52e-05	5.94e-05	1.28e-05	2.05e-05
[S II] 6731Å	3438	6.19e-07	1.11e-06	3.59e-06	1.52e-05	5.94e-05	1.28e-05	2.05e-05
[S III] 6312Å	4368	4.03e-06	6.20e-06	7.74e-06	1.03e-05	1.14e-05	8.04e-06	2.54e-06
[S III] 9069Å	4368	4.03e-06	6.20e-06	7.74e-06	1.03e-05	1.14e-05	8.04e-06	2.54e-06
[Cl III] 5517Å	4368	3.13e-08	4.97e-08	8.33e-08	1.10e-07	1.21e-07	7.91e-08	3.18e-08
[Cl III] 5538Å	4368	3.13e-08	4.97e-08	8.32e-08	1.10e-07	1.21e-07	7.91e-08	3.18e-08
[Ar III] 7136Å	4365	5.32e-07	1.45e-06	2.40e-06	3.16e-06	3.51e-06	2.28e-06	9.81e-07

Table B′.15: Statistics for abundances relative to H^+ from the 3D photoionization model.